The Structure and Flow of Disordered Wet Foams

Cathal B. O'Donovan
School of Physics
Trinity College Dublin

A thesis submitted for the degree of
Doctor of Philosophy
April 14, 2014

Declaration

I declare thesis has not been submitted as an exercise for a degree at any other University.

Except where otherwise stated, the work described herein has been carried out by the author alone.

I agree to deposit this thesis in the University's open access institutional repository or allow the library to do so on my behalf, subject to Irish Copyright Legislation and Trinity College Library conditions of use and acknowledgement.

Cathal O'Donovan Cathal O'Donovan

Acknowledgements

First of all I would like to thank my supervisor Prof. Matthias Möbius, whose insight, guidance and support has been crucial to the compilation of this work. I must also acknowledge Prof. Stefan Hutzler, who has provided great help and direction during my time with the fantastic Foams and Complex Systems group.

I thank my supervisor Prof. Möbius and the School of Physics for providing funding through my time in Trinity. I would also like to acknowledge Trinity College High Performance Computing for all the valuable assistance they have provided and Graduate Studies Office and Trinity Trust for providing funds so that I could attend conferences.

One of the privileges of studying for a PhD is the many diverse and talented people you get to meet in the course of your study. To that end I must acknowledge all my work mates through the years (years!): Joe, Stephen, Aaron, Ho-Kei, Ruggero, Vincent, Tuomo, Rob, David and Gavin. As well as all the summer and project students that I have come to know during my time with the foams group. I am particularly grateful to those that proofread this document. A special mention must go to Mike and Steven who have shared this journey through these past four years (years!). I consider myself lucky to have worked with such readily helpful colleagues during this time.

I would like to give a thank you to all those in DUHAC past and present, who have converted me to the life of a distance runner and in the process given me an outlet from the constant stress of research. There are so many great conversations had on six mile loops around Sandymount, on freezing rambles through the Wicklow mountains and collapsed at the end of the Munich loop in the Phoenix Park that I cannot acknowledge them all, but I would like to particularly thank Vinny for keeping me fit during the write up. At the start of my PhD I read in another thesis acknowledgements the value of getting out of the office and exercising. Personally, I could not recommend

anything better for dealing with the slings and arrows of doing a PhD.

To the many, many great people I have met and worked with in No Drama Theatre, I cannot thank you all enough. In even the darkest weeks of this PhD, thanks to you at least one evening would be filled with joy. I would like to particularly thank all the people I worked with in A Pile of Rocks, you provided me a wonderful distraction at particularly stressful time.

I would very much like to thank my flatmate Brian, who has suffered the most of my raving during these last few months. To my long time friends: Cian, Jack and Cethan - thank you for your support and providing great company when I needed a break.

Most importantly, I would like to thank my family for their unwavering support and unstinting encouragement. To my brilliant sisters Fiona and Aideen, who have never been short of sharing a kind and encouraging word when I needed it. But especially, more than anybody else, I would like to thank my parents, my gratitude to them is ineffable. Thank you mom and dad.

Finally, I would like to dedicate this thesis to the memory of my grandmother, Mary O'Donovan, whose attitude, belief and diligence has been an inspiration to me.

Summary

This thesis concerns the structure and flow properties of wet foams. We primarily use computer simulations of soft particles to model the behaviour of disordered wet foams. We investigate the properties of 2D and 3D polydisperse packings of soft particles and the flow of 2D soft discs as model systems for wet foams.

We study how the polydispersity of packings affect the structure of disordered packings. We examine the correlations between size and contact number of particles in jammed packings at the random closed packing density ϕ_c in two and three dimensions for a wide range of size distributions. Our key finding is the existence of universal correlations between size and contact number that is *independent* of the polydispersity. This empirical result allows us to formulate a mean field approach based on the granocentric model that yields excellent agreement with our data.

We pose the question: how locally random are disordered packings of particles? Many models proposed to describe the properties of packings implicitly that the packings are spatially uncorrelated. Our measurements show correlations in both size and contact number of nearest neighbours. In general, the average contact number and the average size of neighbouring particles do not correspond to the global mean of contact number and size. In 3D packings larger particles are surrounded by smaller particles and vice versa. Moreover, in both 2D & 3D, particles with few contacts neighbour particles with many contacts. Nevertheless, these correlations are sufficiently weak that the predictions obtained from the granocentric model agree well with our data.

The effect of increasing packing fraction above ϕ_c in our simulations is investigated. We find that for a given size distribution, the contact number can be rescaled onto a master curve for any packing fraction in 2D and 3D. At higher densities the correlation between size and contact number remains independent of polydispersity. Our model to predict the contact

number distribution from the size distribution is shown to be valid for denser packings. The spatial correlations found at ϕ_c persist at higher packing fraction.

The empirical Herschel-Bulkley equation is commonly used to described foam rheology. This empirical description demands a unique rheological relation independent of geometry. Recent experimental results have shown the inadequacy of this description in confined geometries where the typical size of confinement is 10-100 particle diameters.

We reproduce these experimental results in 2D simulations and similarly find a non-unique position-dependent rheology, referred to as a non-local rheology. Furthermore, we apply a fluidity model proposed for 3D emulsion flows that captures the rheology of our simulations. We investigate how this model is affected by packing fraction.

Frictionless particles have been show to have an emergent macroscopic friction in both simulation and experiment. Granular materials form piles with a characteristic angle of repose, which is attributed to the static friction that exists between grains. We show that a static angle of repose is also found in frictionless matter, such as wet foam. This result is found in 2D simulations and compared with 2D experiments for a variety of parameters. This angle in the limit of infinite system size tends to $\approx 5°$. We also observe dilatancy when shear stress is applied to the system.

List of Publications

1. **C.B. O'Donovan**, E. I. Corwin, M. E. Möbius. Mean-field granocentric approach in 2D & 3D polydisperse, frictionless packings, *Phil. Mag.*, **93**(4030) (2013).

2. **C.B. O'Donovan**, M. E. Möbius. Spatial correlations in polydisperse, frictionless, two-dimensional packings, *Phys. Rev. E*, **84**(020302) (2011).

Contents

List of Figures

Chapter 1

Introduction

Foams are found in every facet of our daily life, from the soap we wash with and the coffee we drink in the morning, to the bike helmet that protects the author as he travels to work, perhaps the chair you are sitting on right now. You may find foam in the cushioning of your shoes as you play sport, and hopefully find it in the delicious pint of beer with which the foam physicist typically relaxes. Foams are undoubtedly ubiquitous.

In addition to their omnipresence in everyday life, foams have a wide range of industrial applications. They are used in applications as diverse as ore separation by flotation in mines, oil recovery, fire fighting, and dozens others, including the preparation of solid foams for the construction for stable but lightweight technologies.

If nothing else foams are beautiful, see Figure 1.1.1. This appreciation of the aesthetic structures foams form has been the inspiration for the architecture of iconic buildings like Beijing National Aquatics Center and the Olympiastadion in Munich.

Most relevant to this work, foams have been described as an ideal model for the study of disordered complex systems [1].

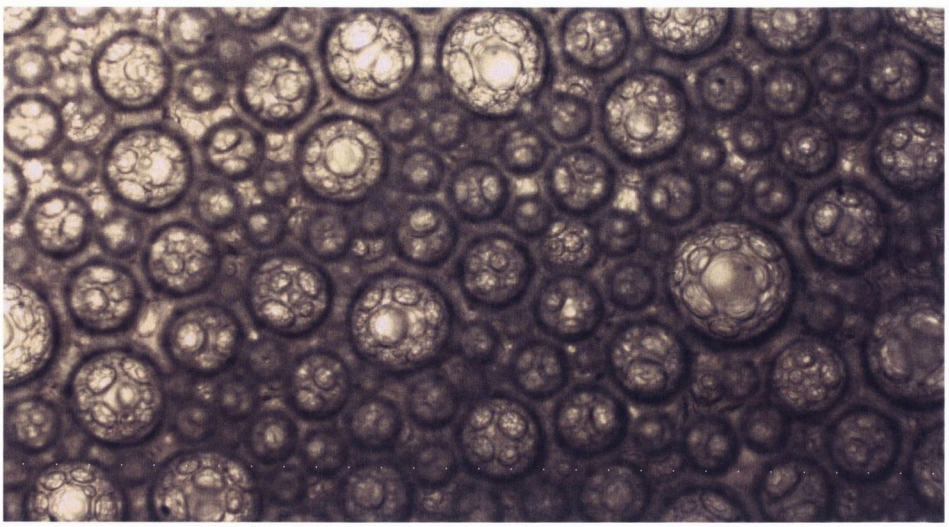

Figure 1.1.1: Experimental image of bubbles in a Guinness foam. Average bubble diameter is $53\mu m$. Image courtesy of G. Ryan.

1.1 Foams

The typical foam is a two phase material that consists of gas bubbles dispersed in a continuous liquid phase with a surfactant that stabilises the foam [2]. Foams are characterised by the fraction of gas enclosed in the total volume of the foam, this is called the packing fraction ϕ. There are two limits to the packing fraction of foams. If the packing fraction is high, ($\phi \approx 1$), the foam is dry. If the packing fraction is low, but not less than a critical packing fraction ϕ_c, the foam is wet. This ϕ_c is the random close packing density, the point at which all the bubbles are just in contact and is related to the jamming phase transition point J, which will be discussed in detail later on. The value of ϕ_c depends on dimension, in 3D, $\phi_c \approx 0.64$ and in 2D, $\phi_c \approx 0.84$. A range of packing fractions in 2D are shown in Figure 1.1.2.

The two limits of wet and dry foam have qualitatively different structures. Bubbles in a dry foam are forced by their surface tension to minimise their surface areas, resulting in polyhedral structures that follow the well defined

rules known as Plateau's laws [4], which specify the angle at which film meet and the number of films that can meet at a vertex. The ideal structure is one that possesses the lowest surface energy while obeying Plateau's laws. In this configuration, the bubbles in the foam are separated by a thin film of liquid, the edges of which are called Plateau borders. As the foam becomes wetter, and ϕ decreases, the Plateau borders swell until the bubbles become spherical. In the wet limit bubbles can be well approximated as spheres with harmonic repulsion.

Foam may be studied on several length scales. The smallest length scale is of the size of surfactant molecules, at this scale the chemistry of the particles are most important. An intermediate, or mesoscopic length scale is on the order of the individual bubble size. This scale is the basis of our investigations in this thesis. At the mesoscopic scale where each bubble is discernible from one another, individual bubbles interact and deform on contact. Finally at the macro-scale, where bubbles form as an ensemble that is considered a foam and forms a continuum. On this length scale the complex interactions at the particle level produce the emergent behaviour of foams. In such a picture we can consider macroscopic quantities like the rheology and the bulk modulus. The focus of this thesis is the employment of simulations on the bubble scale to study macroscopic properties.

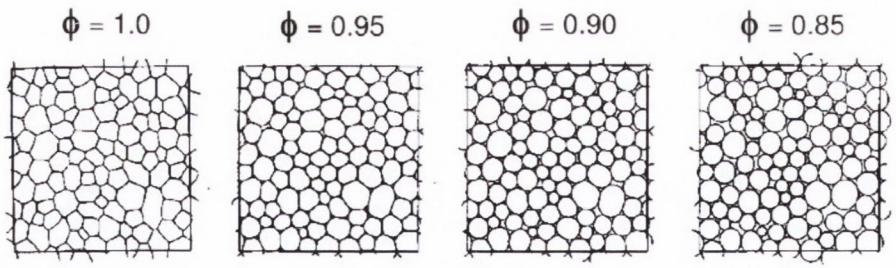

Figure 1.1.2: Structure of 2D foam simulations for different packing fractions ϕ, taken from Bolton and Weaire [3]. The figures range from dry foam on the left to wet foam near ϕ_c on the right.

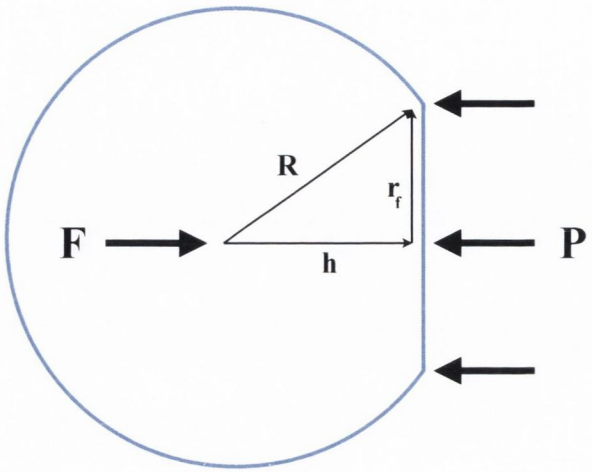

Figure 1.1.3: Force balance on a deformed bubble. The dimensionless compression of the bubble is $\xi_c = {}^{(R-h)}/_{R}$.

The dominant interaction of a static wet foam is the repulsive interaction between bubbles. This interaction is governed by the Young–Laplace law, which describes the balance of pressure difference P across a gas-liquid interface [2] as

$$P = \frac{2\gamma_s}{R}, \tag{1.1.1}$$

where R is the radius of the bubble and γ_s is the surface tension. When a small force is applied to a bubble, it is balanced by the pressure across the thin film, giving

$$F = \pi r_f^2 P, \tag{1.1.2}$$

where πr_f^2 is the area of the facet flattened by the force. To get an expression for the force on a bubble being deformed we define the deformation $\delta\xi_c$, where $\xi_c = {}^{(R-h)}/_{R}$ is a dimensionless measure of the compression [5]. The radius of the flattened facet, by Pythagorus's theorem, can be expressed as

$$r_f^2 = R^2 - h^2, \tag{1.1.3}$$

then rewriting Equation (1.1.3) in terms of ξ_c gives

$$r_f^2 = R^2 - \left(R^2 + R^2\xi_c^2 - 2R^2\xi_c\right). \tag{1.1.4}$$

In the limit of small compression when $\xi_c \approx \delta\xi_c$ gives an approximation of the flattened facet as

$$r_f^2 \approx 2R^2\delta\xi_c, \tag{1.1.5}$$

ignoring terms of $O\left(\delta\xi_c^2\right)$. Substituting the previous expression and the Young–Laplace law into Equation (1.1.2) gives

$$F = 4\pi\gamma_s R\delta\xi_c. \tag{1.1.6}$$

Thus for small deformations, the interaction between bubbles is harmonic with a spring constant $\kappa = 4\pi\gamma_s$.

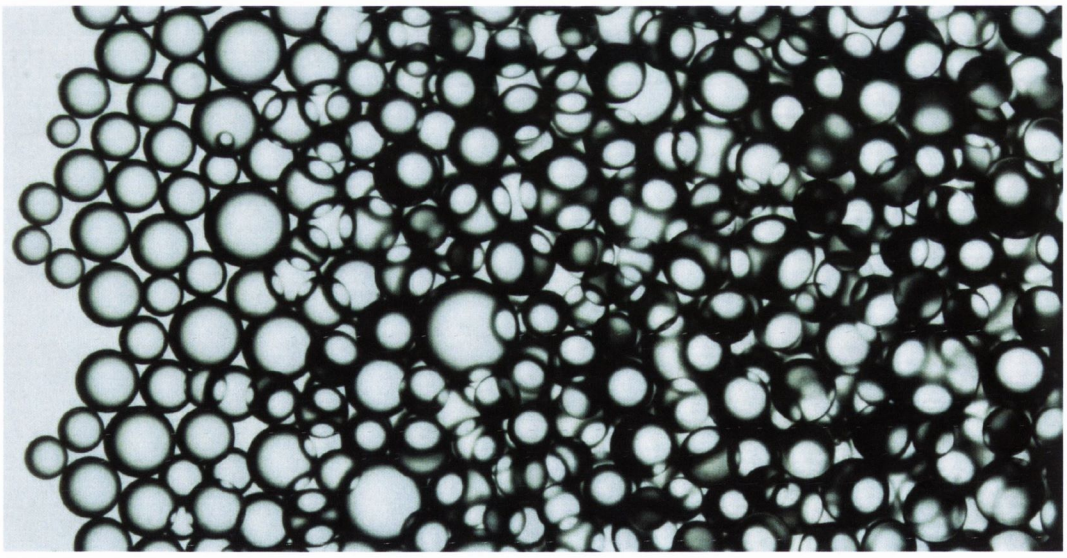

Figure 1.1.4: Experimental image of an emulsion packing. The average particle diameter is $55\mu m$. Image courtesy of G. Ryan.

Foams have a tendency to be disordered with no long range structure. In this regard foams resemble other amorphous materials like emulsions (Figure 1.1.4), soft pastes and particulate gels [6]. Like foams these materials have a finite interaction range, the interaction energy is much greater than kT and therefore athermal. The behaviour of these materials along with that of thermal materials like glasses have been encapsulated in a famous phase diagram by Liu and Nagel [7].

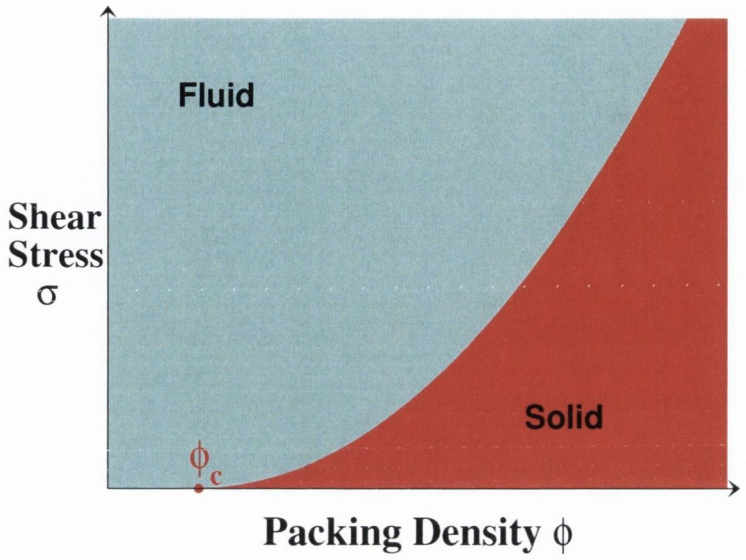

Figure 1.2.1: Schematic of the phase diagram for foams.

1.2 Structure of Thesis

In Figure 1.2.1, we show an equivalent phase diagram for athermal materials like foams, removing the temperature axis from the diagram of Liu and Nagel [7]. This elucidates the phase space of foams. Above the critical packing fraction of the jamming point ϕ_c, with no applied stress, a foam has a rigidity that is characteristic of a solid. Should the density decrease below this critical point the foam behaviour would transition to that of a fluid. Similarly, if sufficient external shear stress σ was applied to a foam above ϕ_c, the foam would start to flow. In this thesis we investigate this phase space, with particular emphasis on the transition between the two states, through simulation of soft particles.

1.2.1 Packings

In Part I of this thesis we explore the first case of static foam at the critical density, by treating foams as packings of disordered soft frictionless particles. Inspection of measures like the radial distribution function in foam experiments [8] and soft particle simulations [9] have shown that this is an appropriate model for foams at the critical density. We investigate the contact properties of polydisperse packings, polydisperse meaning particles with a range of sizes. This is with the view of providing a path to the understanding of the structure of amorphous materials like foams. In Chapter 2, we introduce the field of packings and present some results on bulk polydisperse packings. In Chapter 3, we look at disordered packings from the point of view of a particle in the packing. We investigate the relationship between contact number and particle size, which we use to form a mean-field model to predict the distribution of contacts. In Chapter 4, we look for spatial correlations in the contact number and in particle size in disordered packings. In Chapter 5, we look how the correlations between size and contact number change as the packing fraction is increased.

1.2.2 Rheology

In Part 2 of this thesis we focus on how foams are affected when a shear stress is applied to a foam above ϕ_c in Figure 1.2.1, and the foam starts to flow. This study of the deformation and flow of matter is called rheology [10]. We introduce aspects of rheology in Chapter 6, before moving on to look at the models of foam flow in 2D simulations in Chapter 7. In Chapter 8, we investigate the macroscopic friction as an emergent property of foams and simulations of frictionless particles.

1.2.3 Style

I have chosen to use "we" to refer to work presented in the thesis with consideration of the fact that research is often a collaborative effort, with contributions made to the research from supervisors, project students and collaborators. My personal preference that a writing style using the personal voice makes for a more engaging description of research than the passive voice. I have acknowledged when work that forms a significant part of the thesis undertaken in collaboration with my own research but has been primarily conducted by others. Finally, the layout of this thesis is broken into two parts, focussing on packings and rheology. The intention is that either part can be read independently of the other.

Part I

Structure

Chapter 2

Introduction to Jammed Packings

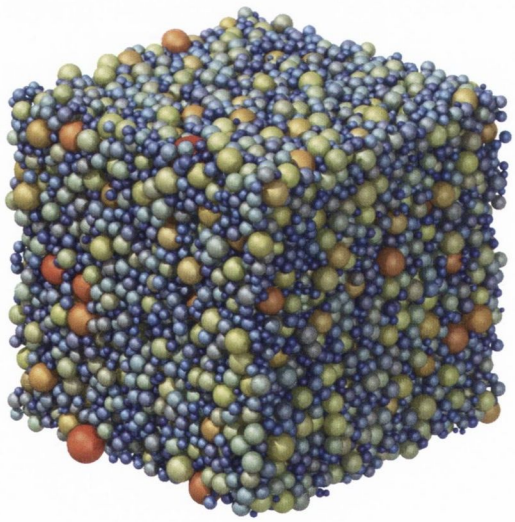

Figure 2.0.1: Visualisation of a soft sphere packing simulation at ϕ_c with a lognormal distribution of radii. The spheres are coloured by size with blue for the smallest through a spectrum to red for the largest.

The question of how spheres pack together has been of interest to scientists for centuries [11], with references to the packing of ordered structures going back to a Sanskrit text written around 499 CE [12]. One of the oldest posited problems is the Kepler conjecture. Johannes Kepler asked in *De Nive Sexangula* (1611): what is the densest packing of hard spheres in three dimensions? Kepler conjectured that this structure would form a face-centered cubic crystal with a packing fraction of $\phi = \pi/\sqrt{18} = 0.74048\ldots$. The proof of this conjecture was Hilbert's eighteenth problem and the focus of much attention for the last century until a rigorous proof was provided by Hales [13] in 1998. The equivalent problem in two dimensions for monodisperse (all particles have equal radius) hard (no overlap) circular discs is a triangular packing with a packing fraction $\phi = \pi/\sqrt{12} = 0.9068\ldots$, which is known as the ordered closed packing density.

Crystalline systems with well defined structures such as the one mentioned above are well understood, less well comprehended is the case when packings are disordered. The packing of spheres that lack the long range order of crystals were first studied by Bernal [14] as a model system for liquids in the late 1950s. Bernal studied a related question to that posed by Kepler: what is the densest random packing of spheres? He found that $\phi = 0.64$ for 3D monodisperse spheres [15]. Despite the randomness of these disordered hard sphere systems, the value for the densest packing has proven to be robust with only small variations found in experimental values [16].

Factors such as static friction and the sphericity of particles can affect how particles pack together. Ellipsoids and other spheroids have been shown to pack more densely than spheres [17, 18]. Conversely frictional spheres can be randomly packed to a density less than 0.64 when poured loosely. This density (called random loose packed) is around 0.55 but is not strictly defined [19, 20]. We will restrict our attention to the contact properties of jammed disordered packings of frictionless spheres and discs in this work.

2.1 Jamming

In the context of soft frictionless amorphous materials, such as wet foams and emulsions, the jamming transition of random close packed spheres is of particular interest and has been a substantial area of study in recent years [21, 22]. At the jamming transition the properties of amorphous packings change abruptly. This is the point where a jammed packing makes the transition from being mechanical stable and behaving like a solid, to becoming unjammed and mechanically unstable, where the yield stress and shear modulus drop to zero and the fluid description is most appropriate. In a static packing of athermal particles, the packing will jam at a density ϕ_c which is the same density as the random close packing density of frictionless particles.

In recent years the packing of athermal static frictionless particles that can overlap and have short range repulsive potentials have been an area of active study. These packings have been described as an 'Ising model' for the jamming transition [18]. Jamming has been proposed as an analogy to the glass transition [7] and possesses interesting physics that is fundamentally different from that of ordinary solids.

The properties of jammed matter are difficult to ascertain experimentally, particularly at ϕ_c, therefore much of the research has been done on computationally generated packings [23]. In a landmark study by O'Hern et al. [24], many properties of jammed amorphous soft spheres such as the shear and elastic modulus were found to scale with distance from ϕ_c. O'Hern et al. [24] found for a finite number of particles that the jamming transition occurs at a range of packing fractions and so calculates the transition to be at the peak of this distribution. This packing fraction is $\phi^* = 0.639 \pm 0.001$ for monodisperse soft spheres independent of the interaction potential used. This is in agreement with the experimentally found packing density of random closed packed hard spheres.

However ϕ^* is only unique in the asymptotic limit of infinite number

of particles. In the case of finite particle number N, it was found that jamming occurs at distribution of packing fractions with a width that scales like $1/\sqrt{N}$. For finite particle number the peak of the distribution of ϕ_c is found at lower densities. To further confuse the issue it has been shown that the density ϕ_c is dependent upon the packing protocol [19, 25] and the preparation history of the packing [26]. Torquato et al. [19] have even queried if the random closed packing density is well-defined and propose the concept of a 'maximally random jammed' state which can be precisely mathematically defined. Though it is important to note that others have argued that this precise definition may not be practical [24]. The definition of jamming used in O'Hern et al. [24], requires that packings do not possess non-trivial floppy modes when at a non-zero pressure and will be discussed in detail in Section 2.1.1.

2.1.1 Isostatic Criteria

What is required for a soft particle packing to be in a jammed state? A jammed state is defined at the point where a packing becomes rigid and the elastic moduli take a finite non-zero value, which requires that the pressure is non-zero. In order for a packing to be considered jammed there also cannot be collective particle motions that have a zero elastic energy cost (floppy modes) other than those attributed to rattlers. Rattlers are particles that do not have a sufficient number of contacts to be mechanically stable. By setting a constraint on the average contact number of a packing $\langle z \rangle$, one can demand the system generically disallow floppy deformations [27, 28]. This sets the isostatic contact criteria for a rigid packing described below.

The isostatic condition can be shown by the following arguments. If there are D dimensions with N soft particles excluding rattlers, there are ND degrees of freedom of which D are trivial due to translational invariance. So, $ND - D$ degrees of freedom must be constrained. This requires that the critical number of contacts N_c fulfil,

$$N_c \geq ND - D. \tag{2.1.1}$$

If we call the critical average contact number z_c, and note that every contact is shared by two particles, then we can write the number of contacts as

$$N_c = \frac{Nz_c}{2} = ND - D. \tag{2.1.2}$$

In order to have a positive bulk modulus an additional contact must be added [29] giving,

$$\frac{Nz_c}{2} = ND - D + 1. \tag{2.1.3}$$

The isostatic contact criteria then becomes,

$$z_c = 2D - \frac{2D - 2}{N}. \tag{2.1.4}$$

In the limit of large N this brings the standard criteria of

$$z_c := \begin{cases} 6, & \text{in 3 dimensions,} \\ 4, & \text{in 2 dimensions,} \end{cases} \tag{2.1.5}$$

which is commonly used [18, 24]. For more details on this isostatic condition see Alexander [27].

In a recent work Dagois-Bohy et al. [30] show that for a packing to be stable to shear, it requires that the shape of the periodic cell has to be allowed to deform during minimization of the packing. There are an additional $D(D+1)-1$ degrees of freedom that have to be added to Equation (2.1.4) to account for such a deformation. The isostatic criteria is then given as

$$z_c = 2D + \frac{D^2 - D}{N}, \tag{2.1.6}$$

which leads to a number z_c quoted in Equation (2.1.5), only in the asymptotic limit of large N. This will be discussed further in Section 2.2.

While globally these mechanically jammed states are constrained to have $\langle z \rangle = z_c$, there is a distribution of contact numbers for particles and there are some particles that have fewer than necessary contacts to achieve local mechanical stability. In general, particles that have less than $D+1$ contacts cannot be locally mechanical stable. For 3D, that means all particles with less than 4 contacts and 2D, all particles with less than 3 contacts are locally unstable. These locally unstable particles are called rattlers and the contribution of rattlers to the contact number analysis is omitted but are included when calculating the packing fraction.

2.1.2 Polydispersity

The discussion of jammed packings is often focussed on monodisperse packings in 3D. Studying jamming of monodisperse discs in 2D is inappropriate because such packings have been shown to spontaneously order into crystalline structures [31], thus prevent the investigation into disordered systems. Indeed for two dimensional packings, in order to be disordered it is required that the standard deviation of the size distribution σ_R must be greater than 0.1, otherwise crystallisation can occur [32]. Frequently the choice of a 50-50 bidisperse mixture of particles with a radius ratio of 1:1.4 between small and larger particles are used to avoid crystallisation [31].

There has also been a long history of study of the density at which random close packing occurs for binary mixtures of particles in both experiment [33] and simulation [34, 35, 36]. All studies have found that as the ratio between the size of small and large particles moves further from one, the density at which ϕ_c occurs increases. These bidisperse packings exhibit similar properties to monodisperse packings when jammed. The scaling of the shear and bulk moduli (denoted as G and B respectively) with distance from jamming is similar to the monodisperse case [24, 36], namely

$$G \propto (\phi - \phi_c)^{\frac{1}{2}}, \quad B \propto H(\phi - \phi_c),$$

where H is the Heaviside step function. These scalings of the elastic moduli of packings at ϕ_c are true in both 2D and 3D. More prevalent in nature, though not as a widely studied, are packings with a continuous distribution of sizes. Experiments and simulations of continuous size distributions [37, 38, 39, 40, 41] have investigated the value of ϕ_c and like that of binary mixtures found that ϕ_c increases with polydispersity. Another result of increased polydispersity in packings is an increase in the fraction of particles that are rattlers [41].

2.2 Simulation Procedure

In light of some of the properties of packings being sensitive to the packing protocol, we use two different protocols to investigate disordered polydisperse packings of soft particles. The first code is a molecular dynamics code based on the bubble model [42]. This code was originally developed to simulate the flow of foams in 2D by Langlois et al. [43]. The code has been amended to investigate the properties of packings.

The second is a conjugate gradient minimisation procedure for packing soft particles. This particular implementation of this procedure was initially developed by Corwin et al. [44]. In this thesis it is implemented in two and three dimensions and is used in all the packing results produced in Part I of this thesis unless stated otherwise.

2.2.1 Bubble Model Code

This molecular dynamics code is responsible mainly for the rheological results in this thesis but contributes some of the 2D disordered packing simulation results. Durian [42] developed the bubble model to simulate the flow of wet foams. In the bubble model, bubbles are represented by overlapping (soft) discs (Figure 2.2.1(b)). This model was later refined by Langlois et al. [43] by removing a mean field approximation of viscous dissipation in Durian's model. The bubble model simulates a foam by allowing each soft disc to move independently in a periodic cell and considers interactions only when overlap occurs. As a simplification in this model, the gas displaced upon overlap between discs is ignored. In real foams when bubbles interact, a deformation in the shape of the bubble occurs due to the gas displaced by the interaction (Figure 2.2.1(a)). For small deformations in wet foams this approximation is good [3, 5]. In order to describe the elastic repulsion due to surface tension experienced by bubbles in a foam, a simple spring force model for the elastic interaction of soft discs is used. This elastic repulsive

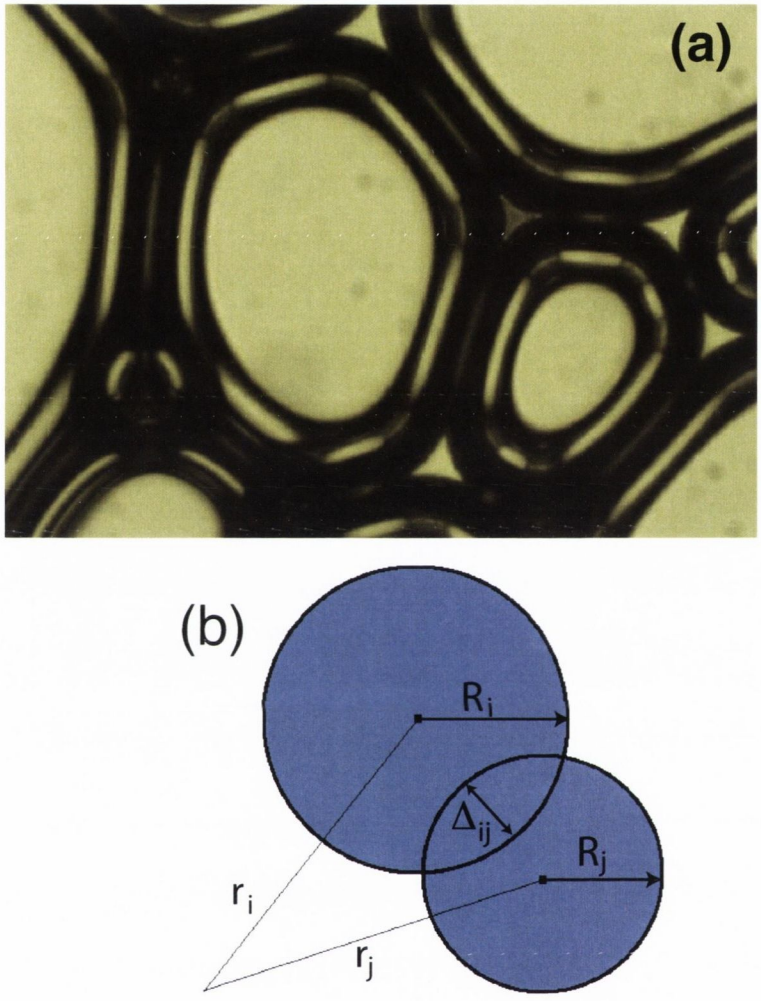

Figure 2.2.1: (a) Experimental image of a 2D foam. Note the deformation of the bubbles due to contact. (b) Image of soft discs with overlap Δ_{ij} between the two soft discs in contact with radii R_i and R_j, located at $\boldsymbol{r}_i$ and $\boldsymbol{r}_j$, respectively.

force F_n acting on disc i due to disc j is given by:

$$\boldsymbol{F}_n = \kappa \frac{2\langle R \rangle}{R_i + R_j} \Delta_{ij} \boldsymbol{n}_{ij}. \tag{2.2.1}$$

Here κ is the coefficient of elasticity, $\boldsymbol{n}_{ij} = \frac{\boldsymbol{r}_i - \boldsymbol{r}_j}{|\boldsymbol{r}_i - \boldsymbol{r}_j|}$ the normal vector between bubbles i and j and the overlap Δ_{ij} is given by

$$\Delta_{ij} = \begin{cases} (R_i + R_j) - |\boldsymbol{r}_i - \boldsymbol{r}_j|, & \text{if}(R_i + R_j) > |\boldsymbol{r}_i - \boldsymbol{r}_j| \\ 0, & \text{otherwise.} \end{cases} \tag{2.2.2}$$

R_i and R_j are the radii of discs i and j, centred at $\boldsymbol{r}_i$ and $\boldsymbol{r}_j$ respectively and $\langle R \rangle$ is the average disc radius of the packing. Equation (2.2.1) is related to the harmonic approximation made in Equation (1.1.6), where the spring constant $\kappa = 4\pi\gamma_s$ and the deformation ξR now equates to Δ_{ij}. In addition the term $2\langle R \rangle / R_i + R_j$ is introduced to account for smaller bubbles having a stronger repulsion than larger bubbles.

A second interaction force accounts for viscous dissipation in the films between two bubbles in contact. This viscous drag force F_d is found in experiment to be $F_d \propto \Delta v^{2/3}$ [45, 46], where the exponent of $2/3$ is due to the bubbles deforming on contact and the film thickness of the liquid in the bubbles also changing when the foam flows [47, 48]. For simplicity in this model F_d is linear and only occurs with an overlap between discs,

$$\boldsymbol{F}_d = -c_b(\boldsymbol{v}_i - \boldsymbol{v}_j) H(R_i + R_j - |\boldsymbol{r}_i - \boldsymbol{r}_j|), \tag{2.2.3}$$

where c_b is the dissipation constant and $\boldsymbol{v}_i$ and $\boldsymbol{v}_j$ are the respective disc velocities. We use a Verlet algorithm to calculate the trajectories of the discs. A Verlet algorithm relies on the position calculated at the previous and present time-step and the forces calculated at the present time-step to

calculate the next position and velocity of a particle,

$$\boldsymbol{r}(t+\Delta t) = 2\boldsymbol{r}(t) - \boldsymbol{r}(t-\Delta t) + \frac{\boldsymbol{F}_n(t) + \boldsymbol{F}_d(t)}{m_b}\Delta t^2 \tag{2.2.4}$$

$$\boldsymbol{v}(t+\Delta t) = \frac{\boldsymbol{r}(t+\Delta t) - \boldsymbol{r}(t-\Delta t)}{2\Delta t} \tag{2.2.5}$$

where m_b is the mass of the disc.

Inertial effects are negligible for bubbles, therefore we set the ratio of the inertial timescale $t_i = m_b/c_b$ to the viscous timescale $t_v = c_b/\kappa$ to be $t_i/t_v = \kappa m_b/c_b^2 \ll 1$ [43, 49]. These timescales are set by the prefactors of Equations (2.2.1) and (2.2.3), which are chosen to be close to the values found in experiment.

In each packing we use 1500 polydisperse particles whose radii R are normally distributed with a polydispersity $\sigma_R = 0.28$. Computation time limits the number of particles in each packing, though in simulations with 1000 particles, finite size effects are considered small. The discs are randomly placed in a periodic box at low packing fraction and then allowed to relax while their radii are slowly increased until the prescribed packing fraction ϕ is reached. The simulation was terminated when the energies reached a steady state, indicating a local minimum of the energy landscape, provided the isostatic criteria has been fulfilled. Upon reaching force equilibrium, discs with fewer than three contacts are removed for the analysis of the contact network but are included in the determination of the packing fraction. Contacts are defined as overlaps between discs. Typically between 8 and 14 packings have been created for each packing fraction to increase statistics.

When the total energy of a packing has reached a steady state, the configuration is in a local energy minimum. The condition for a steady state is when the change in the energy of the system (calculated every 10^5 time-steps) is 2.5×10^3 less than the total energy of the system for 10^6 successive time-steps. Energy is lost from the packings only through the dissipative interactions between discs due to the viscous drag force F_d.

2.2.2 Conjugate Gradient Minimisation

We now introduce another method to study packings in 2D and 3D. We simulate frictionless particles that interact through purely repulsive body centred forces, which can be written as a function of the overlap between two particles in contact. The overlap is

$$\delta_{ij} = 1 - \frac{d_{ij}}{R_i + R_j}, \tag{2.2.6}$$

where R_i and R_j are the radii of spheres i and j and d_{ij} is the distance between the respective centres of the spheres. The interaction potential of the spheres is

$$V(d_{ij}) = \begin{cases} \frac{k}{2}\delta_{ij}^2, & \text{if } \delta_{ij} > 0, \\ 0, & \text{otherwise.} \end{cases} \tag{2.2.7}$$

These interactions are harmonic with a spring constant k.

We followed a simplified version of the infinite temperature quench technique presented in O'Hern et al. [24] to create jammed packings, this protocol has been previously used in simulations at ϕ_c [44, 50]. Each simulation starts with a fixed number of particles ($N = 16384$) whose positions are distributed randomly within a cubic box with periodic boundary conditions. This is an approximation to an infinite temperature condition. The particles have their radius drawn from a set size distribution $P(r)$ and then rescaled such that the desired global packing fraction ϕ matches that of a density which has been set. The temperature is then quenched close to zero and nearly all of the energy in the system is removed by allowing particles to move away from one another by a conjugate gradient method. This method minimises the overlap between spheres and hence the the total energy of the packing [51]. We decrease the packing fraction in small increments ($\Delta\phi = 0.0005$). Packings are said to have reached the jamming threshold ϕ_c when they fulfil the criteria that the average contact number of packings of that size distribu-

tion is $z_c + 0.05 > \langle z \rangle \geq z_c$ and the pressure is non-zero. This indicates a mechanically stable packing and the procedure is then stopped. At a given packing fraction a small number of packings fall below the isostatic criteria and are discarded. We choose the $\langle z \rangle$ threshold to be 0.05 from the isostatic point which is sufficiently close to the jamming point for our analysis, getting closer to z_c does not alter our results.

For each size distribution up to 500 realisations of a packing at ϕ_c in three dimensions and 50 realisations in two dimensions are created. An example of a sphere packing is shown in Figure 2.0.1. A variety of size distributions are created including discrete size distributions of monodisperse, where all particles have a single characteristic radius R, and bidisperse, where there is a 50-50 mixture with a size ratio 1:1.4, to continuous distributions in which the spheres can have a range of radii given by lognormal, Gaussian or uniform distributions, which are plotted in Figure 2.3.1.

The main focus of this algorithm and an application of the bubble model algorithm is to produce jammed amorphous packings close to the jamming transition to investigate the contact properties of these packings. Recently Dagois-Bohy et al. [30] have shown that some realisations can be unstable to shear near the jamming point. With neither algorithm do we check that the packing is stable to shear. However, particularly using the CG minimisation method, since the average contact number is greater than z_c and the number of particles is large then the likelihood of a packing being unstable to a small shear stress is slight.

2.3 Bulk Properties of Polydisperse Packings

The size distribution affects the packing density at which the isostatic point is reached [37]. We define σ_R as the normalised standard deviation of the particle radius distribution $P(R)$ where rattlers have been removed,

$$\sigma_R = \sqrt{\frac{\langle R^2 \rangle}{\langle R \rangle^2} - 1}. \tag{2.3.1}$$

The shape of $P(R)$ changes when rattlers are removed, as shown in Figure 2.3.1. On average rattlers only tend to be smaller particles but there is a limit on their size below which all particles are rattlers. As the width of the size distribution σ_R is increased, ϕ_c becomes larger because smaller particles are able to fit between the interstices of larger particles in contact [39], as seen in Figure 2.3.2 for three and two dimensions (inset). This results in an increase

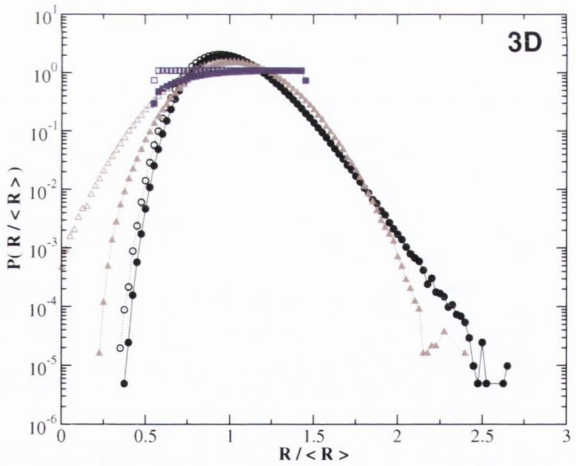

Figure 2.3.1: Continuous size distributions used to create the soft sphere packings. The distributions are: (○) lognormal $\sigma_R = 0.20$; (△) Gaussian $\sigma_R = 0.22$; (□) uniform $\sigma_A = 0.24$. The open symbols represent the original size distribution and the closed symbols represent the size distribution once rattlers are removed.

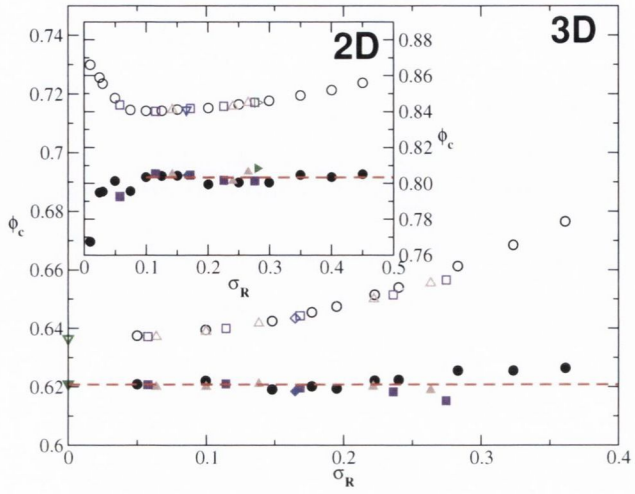

Figure 2.3.2: Relationship between the standard deviation of the radius distribution and ϕ_c for a variety of size distributions in three dimensions: ($\triangledown$) monodisperse; ($\Diamond$) bidisperse; ($\square$) uniform; ($\triangle$) Gaussian; ($\circ$) lognormal. The packing fractions including all particles are plotted as open symbols. The closed symbols denote ϕ_c'. The dashed line is the average packing fraction with rattlers omitted for all size distributions. Inset: Relationship between σ_R and ϕ_c in two dimensions. The data is labelled the same as in the main plot with the addition of ($\triangleright$) Gaussian distribution using the bubble model code with $\langle z \rangle = 4.06$. The dashed line is the average packing fraction with rattlers omitted for all size distributions with $\sigma_R \geq 0.1$.

of rattlers, which is shown in Figure 2.3.3 and its inset. Rattlers, which are always present in real and simulated packings, are usually not discussed in detail in the literature. Our values are largely consistent with the results from literature [41, 44, 52]. For narrow size distributions, the packing fraction at which the isostatic point is reached and the relative amount of rattlers in a packing is unaffected by the type of size distribution of the packing. As the size distribution becomes wider more particles are found in the interstices between particles and do not contribute to the mechanical stability of the packing. Polydispersities with a large population of small particles, such as

the uniform distribution, have an increased amount of rattlers, though ϕ_c is only slightly affected. The increase of ϕ_c and number of rattlers in 2D packings for $\sigma_R < 0.1$ is attributed to the effects of crystallisation seen in Figure 2.3.4, where crystalline patches form, leading to an increase in ϕ_c. A large number of rattlers are particles located in between crystalline patches.

Also plotted in Figure 2.3.2 is ϕ_c', which is ϕ_c with the volume of rattlers excluded. This ϕ_c' is found to be a constant that is independent of the size distribution in three dimensions, where the average $\phi_c' = 0.621 \pm 0.003$. In two dimensions for $\sigma_R \geq 0.1$ the ϕ_c' is also constant and independent of polydispersity when crystallisation does not occur with the average ϕ_c' equal to 0.803 ± 0.002.

To our knowledge nobody has looked at ϕ_c'; while this is below ϕ_c including rattlers, there is no literature value to compare it against. The constancy

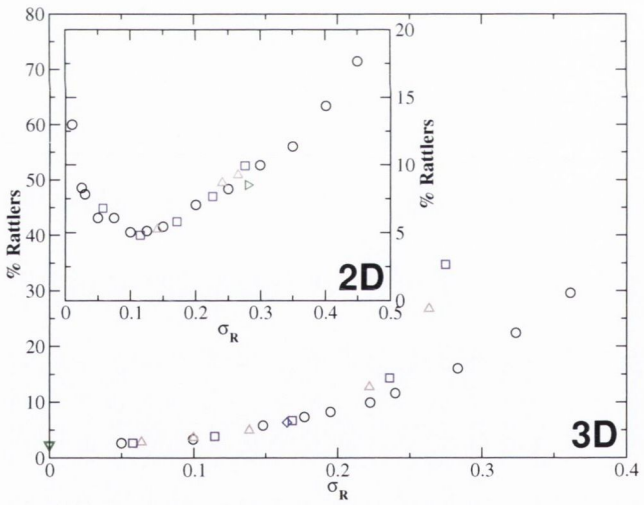

Figure 2.3.3: Relationship between the standard deviation of the radius distribution and the percentage of rattlers at ϕ_c in three dimensions. Inset: Relationship between the percentage rattlers found at ϕ_c in two dimensions and the standard deviation of the radius distribution. The data is labelled the same as in Figure 2.3.2.

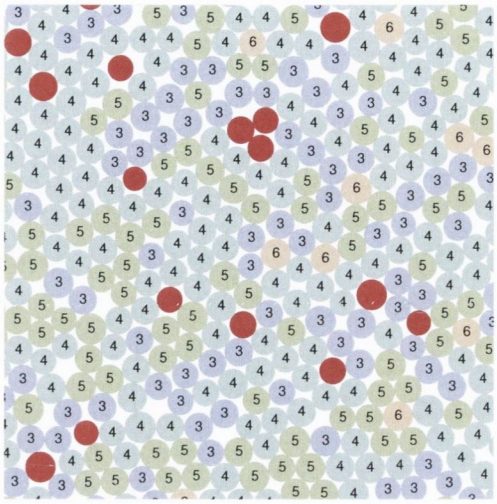

Figure 2.3.4: Visualisation of a packing with $\sigma_R = 0.05$. The numbers in the centres of the discs represent the number of contacts of that disc. The red coloured discs are rattlers which are locally unstable.

of the rattler free ϕ_c' is an interesting phenomenon for which we do not have a satisfactory explanation. It appears that two trends cancel out at higher polydispersities: (a) the increase of rattler percentage with polydispersity which would lower ϕ_c'; (b) the ability to fill space more efficiently with increasing polydispersity as evidenced by the increase of ϕ_c, this would increase ϕ_c'.

2.3.1 Contact Variance

The contact properties of disordered packings is the main focus of Part I this thesis. There have been some simulation and experimental studies on the contact properties of polydisperse, disordered packings [38, 41, 53, 54] and recently the granocentric model has been proposed to predict the local packing structure at ϕ_c [44, 50, 55] in three dimensions.

Changing the polydispersity also affects the contact properties. As seen in Figure 2.3.5, changing the width of the size distribution affects the standard

deviation of the contact number distribution σ_Z, which is defined as

$$\sigma_Z = \sqrt{\langle z^2 \rangle - \langle z \rangle^2}. \tag{2.3.2}$$

For all types of size distribution it is shown that broader size distributions results in broader contact number distributions. This trend is independent of the type of size distribution in both two and three dimensions, though there do appear to be deviations for the uniform distribution at large σ_R in 3D.

For two-dimensional cellular structures a corresponding relationship between the standard deviation of the size distribution and the standard deviation of the number of cell faces has been observed [56, 57, 58]. While the width of the contact number distribution is set by the width of the size distribution only, the shape of the contact number distribution does depend on the distribution of particle sizes used, which will be shown in the next chapter in Figure 3.3.5.

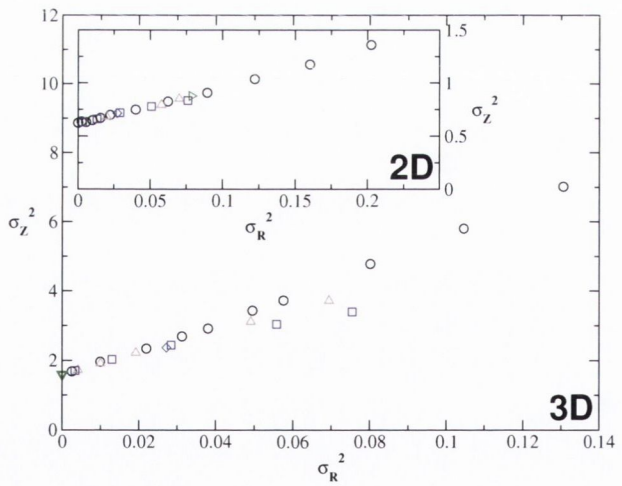

Figure 2.3.5: Relationship between the variance of the radius distribution σ_R^2 and the variance of the contact number distribution σ_Z^2 in 3D. Plotted in the inset is the variance of the radius distribution σ_R^2 versus σ_Z^2in 2D. The data is labelled the same as in Figure 2.3.2.

Chapter 3

Local Contact Properties of Disordered Packings

While a large body of literature on random packings is devoted to the bulk properties of monodisperse and bidisperse packings near the jamming transition [18, 22, 24, 54], the properties of polydisperse packings have been left comparatively neglected. Important results on the local structure of polydisperse packings have emerged only in recent years [44, 50, 59].

Prior to this, there have been some studies on the relationship between the size of cells and contact number on a local scale [41]. Research has also focussed on the local mechanical properties through the study of force chains [60, 61, 62].

In this chapter, we take inspiration from the pioneering work by Clusel et al. [50] that established a link between the size distribution and the local structure of packings. This was achieved by taking a granocentric approach, viewing the packing from the perspective of a particle in the bulk. We expand on this work by investigating how the correlations between particle size and contact number depend upon the polydispersity of packings.

3.1 The Granocentric Approach

The first to take a granocentric viewpoint was Dodds [63]. Dodds formulated a simple model to predict the variation of the average contact number distribution with polydispersity of first 2D, and then 3D polydisperse packings, by enumerating all of the possible local arrangements particles of different sizes could form in a disordered packing. However, Dodds model underestimated the average contact number of the packings systematically.

More recently, Clusel et al. [50] have proposed a statistical model that describes the contact number distribution for polydisperse packings, as well as predicting the packing fraction. Their model confronts the problem of disordered packings by treating each particle as undergoing a similar local stochastic process.

In this model, the contact distribution is modeled on the idea that each particle is undergoing two independent random processes. The first is the formation of the neighbourhood of the granocentric particle, where the available solid angle of a particle is filled up to a certain defined limit (Ω_{max}) that is less than the overall solid angle of a sphere 4π, in the manner shown in Figure 3.1.1. This neighbourhood is defined by the available solid angle of the granocentric particle with particles whose radius is drawn from the size distribution $P(R)$ and then linked this to the solid angle by a Laplacian transform. The second process is the selection of the fraction of contacts that are formed from the neighbours around this central particle. This fraction is found to be independent of the central particle's size. The result is a two parameter model that describes the contact number distribution quite well. A third parameter of the model, the average distance between the particle and non-contacting neighbours, then allows a prediction of the packing fraction.

This granocentric model makes a couple of assumptions that we will address in the next chapter, that the disordered packing is homogeneous and does not contain any spatial correlations in the distribution of particle sizes and contact numbers.

Initially the granocentric model of Clusel et al. [50] worked only for polydisperse packings, where the disorder is due to the range of particle size distribution rather than the positional disorder found in monodisperse packings. With some alterations to the method of implementing the granocentric model, it was later shown to be able to describe packings of with low polydispersity [55]. Recently a mean-field version of the model has been proposed to describe the various relations between size and coordination number in 2D and 3D cellular structures [59].

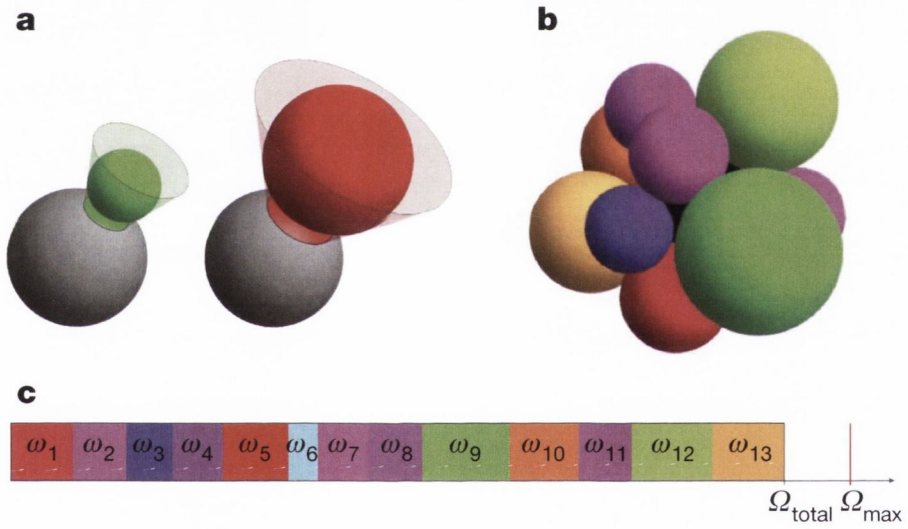

Figure 3.1.1: Granocentric view of a random packing, reproduced from Clusel et al. [50]. **a** The space occupied by a neighbour around a central particle is measured by the solid angle it subtends, which is shown to depend on the neighbour size (green, smaller; red, larger). **b** Neighbouring particles cover the surface of the central particle. **c** Space-filling around the central particle in **b** is represented by a sum of the colour-coded solid angles ω occupied by each neighbour. The sum of all the solid angles ω add up to the total solid angle occupied by the surrounding particles Ω_{total}.

3.2 Contact Number of a Particle of a Given Size

We now investigate the local structure of jammed packings by examining how contact number correlate with the size of a particle. In light of the results of the granocentric model of Clusel et al. [50], we examine the results of our simulations first in three dimensions, before turning our focus towards two dimensions.

3.2.1 Three Dimensions

To study the local contact number properties of these packings, we look at the average number of contacts a particle has for a given size. We define the average contact number for particles of a given size as,

$$\langle z|x\rangle = \sum_{z=4} zP(z|x), \tag{3.2.1}$$

where $P(z|x)$ is the contact number distribution for particles of a given dimensionless size x, which can be the radius, surface area or volume. The summation in Equation (3.2.1) is bounded below at $z = 4$ in order to omit rattlers. This average contact number for particles of given size x at ϕ_c is plotted for a wide range of size distributions of different widths and shape in Figure 3.2.1. We scaled the data in three different ways, in terms of the normalised radius, normalised surface area and normalised volume in Figure 3.2.1(a), (b) and (c) respectively. In the three scalings, $\langle z|x\rangle$ for all size distributions and polydispersities follow similar trends. Namely, larger particles have more contacts on average. This can be explained in the context of the granocentric model [44, 50, 55].

Larger particles can accommodate more neighbours on average since the solid angle subtended by the neighbouring spheres is smaller for a larger central particle. One of our key results is that these correlations are independent

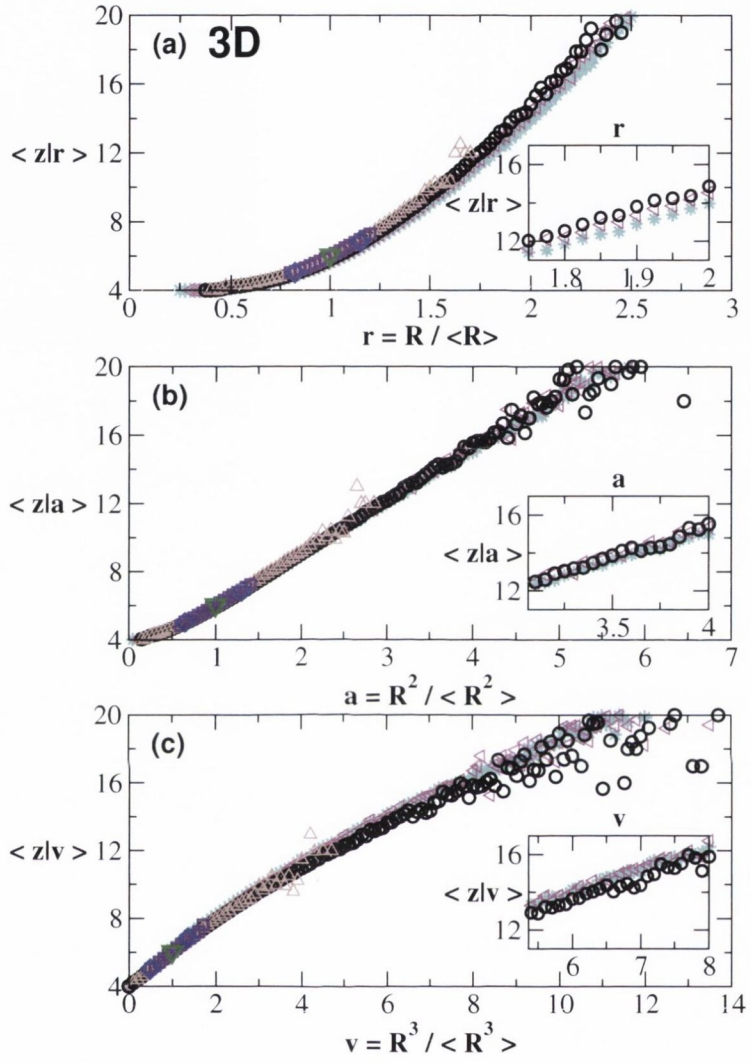

Figure 3.2.1: The average of the contact number distribution for a particle of a given size for the six different size distributions at ϕ_c: ($\triangledown$) monodisperse; ($\Diamond$) bidisperse, radius ratio 1:1.4; ($\square$) uniform $\sigma_R = 0.11$; ($\triangle$) Gaussian $\sigma_R = 0.14$; ($\circ$) lognormal $\sigma_R = 0.20$; ($\triangleleft$) lognormal $\sigma_R = 0.28$; ($*$) lognormal $\sigma_R = 0.32$. We present three different scalings: (a) in terms of the normalised radius r; (b) in terms of the normalised area a; (c) in terms of the normalised volume v. The data are plotted over a range that illustrates the quality of the collapse. Plotted in each inset is a magnification of the data on an equivalent range for each scaling that emphasises the quality of the collapse for that scaling.

of polydispersity.

While all scalings appear to lead to a collapse, a close look at the data in the insets of Figure 3.2.1 reveals that the best collapse is observed when the scaling is in terms of the normalised area,

$$x = a = \frac{R^2}{\langle R^2 \rangle}. \tag{3.2.2}$$

This is shown in Figure 3.2.1(b). This collapse of the data is well described by a linear fit,

$$\langle z|a \rangle = \langle z \rangle + \gamma(a - 1), \tag{3.2.3}$$

which is plotted in Figure 3.2.2. When we look at a wide selection of polydispersities and plot the contact number average in terms of this normalised

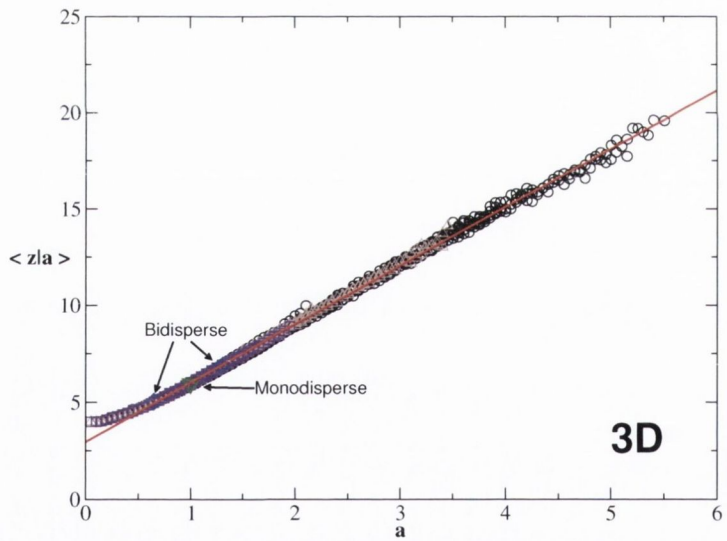

Figure 3.2.2: The average contact number for particles of a given area a at ϕ_c in 3D for all (▽) monodisperse, (◇) bidisperse, (□) uniform, (△) Gaussian and (○) lognormal size distributions at all the widths σ_R we have considered (see Figure 2.3.2). The solid red line is a fit to Equation (3.2.3).

surface area at ϕ_c, all the polydispersities collapse onto the same linear trend that can be seen in Figure 3.2.2. The contact number average for the discrete distributions (monodisperse, bidisperse) have the same value as that of the continuous distributions despite the significant difference in the composition of the packing. Figure 3.2.2 shows that at ϕ_c, the relationship between z and a is universal and independent of size distribution. This suggests that the contact properties of a particle depends only on its surface area.

The form of Equation (3.2.3) ensures that the isostatic constraint

$$\langle z \rangle = \int_0^\infty \langle z|a \rangle P(a) da = 6, \tag{3.2.4}$$

is satisfied. The fitting parameter is found to be $\gamma = 3.032 \pm 0.004$.

It must be noted that because we omit rattlers from our analysis that for low a, the average $\langle z|a \rangle$ is constrained to be a minimum of 4. Also for large values of a the number of particles of that size are few and therefore the value of the average $\langle z|a \rangle$ becomes more scattered. For all equations fitted and figures plotted of averaged quantities, any binned data with less than 100 particles are omitted from Part I of this thesis. This is a standard procedure to avoid showing scatter in the tails, for more details see Appendix A.

In Figure 3.2.3 a number of different distributions are plotted for narrow intervals of a, and for each a interval plotted all the $P(z|a)$ collapse independent of size distribution. This confirms what is suggested in Figure 3.2.2: that the contact number distribution for a particle in a packing at ϕ_c does not depend on the global size distribution of the packing but on the size of the particle only.

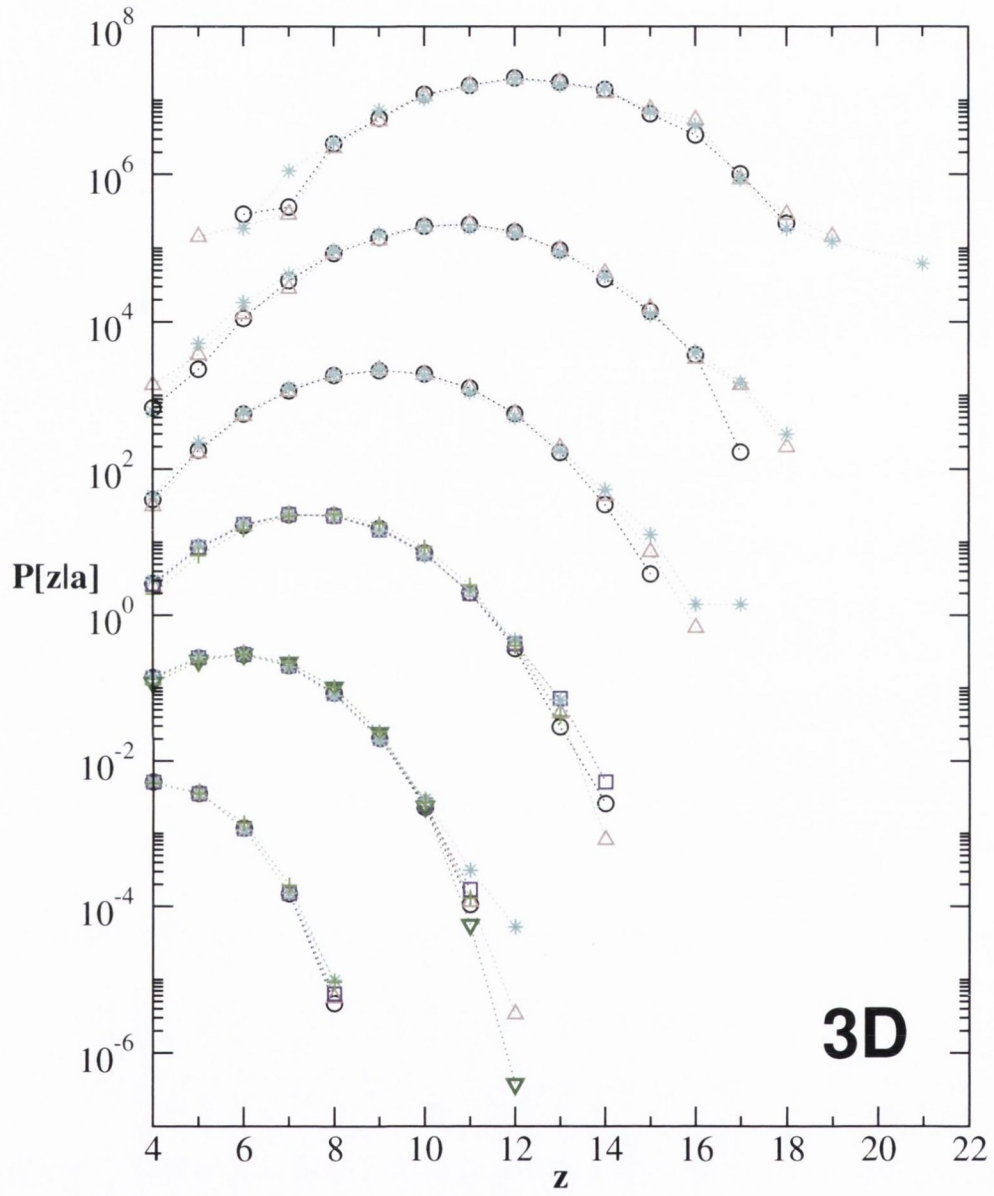

Figure 3.2.3: The contact number distribution for particles of a given size $P(z|a)$ for six different size distributions at ϕ_c in 3D. The data is labelled: ($\triangledown$) monodisperse; ($+$) lognormal $\sigma_R = 0.10$; ($\circ$) lognormal $\sigma_R = 0.20$; ($\triangle$) lognormal $\sigma_R = 0.22$; ($\square$) uniform $\sigma_R = 0.24$; ($*$) lognormal $\sigma_R = 0.32$. Plotted here is a selection of the $P(z|a)$ for 6 different intervals a with $P(z|a)$ for each interval shifted on the y-axis for clarity. Plotted in order of lowest to highest is $0.475 < a < 0.525$; $0.975 < a < 1.025$; $1.475 < a < 1.525$; $1.975 < a < 2.025$; $2.475 < a < 2.525$; $2.975 < a < 3.025$. For larger values of a the number of instances of that particle size becomes smaller.

3.2.2 Two Dimensions

Now we investigate whether this observation is particular to three dimensions, by examining if these local contact number size correlations can also be found in 2D. Furthermore, we address whether the simulation algorithm used affects the results of these correlations.

A similar treatment to that used in three dimensions works in two dimensions. In Figure 3.2.4(a), (b) and (c) the average contact number for particles of a given size x at ϕ_c is plotted and scaled in terms of the normalised radius, normalised surface area and normalised "volume". All size distributions follow similar trends, namely that larger particles have more contacts on average. Similar to the three-dimensional case, the best collapse is found when the scaling is,

$$x = \frac{R^{D-1}}{\langle R^{D-1} \rangle} \tag{3.2.5}$$

as in Figure 3.2.4(a). We conjecture that this may be true for $D > 3$ as well, however this conjecture for $D > 3$ is not explored in this work. Therefore the appropriate scaling variable for size-contact number correlations in 2D packings is $x = r$.

In Figure 3.2.5 a similar collapse of the average contact number for particles of a given radius $\langle z|r \rangle$ for a range of size distributions to that found for $\langle z|a \rangle$ in three dimensions. A linear relationship between $\langle z|r \rangle$ and r, which is similar to Equation (3.2.3), is given by,

$$\langle z|r \rangle = \langle z \rangle + \gamma_{2D}(r - 1), \tag{3.2.6}$$

is fit to the data in Figure 3.2.5 with the fit parameter $\gamma_{2D} = 2.023 \pm 0.007$.

The result is similar to that observed in two dimensional disc packings [64] for ϕ above the jamming transition, which was achieved using a packing algorithm based on the bubble model, described in Section 2.2.1. The data

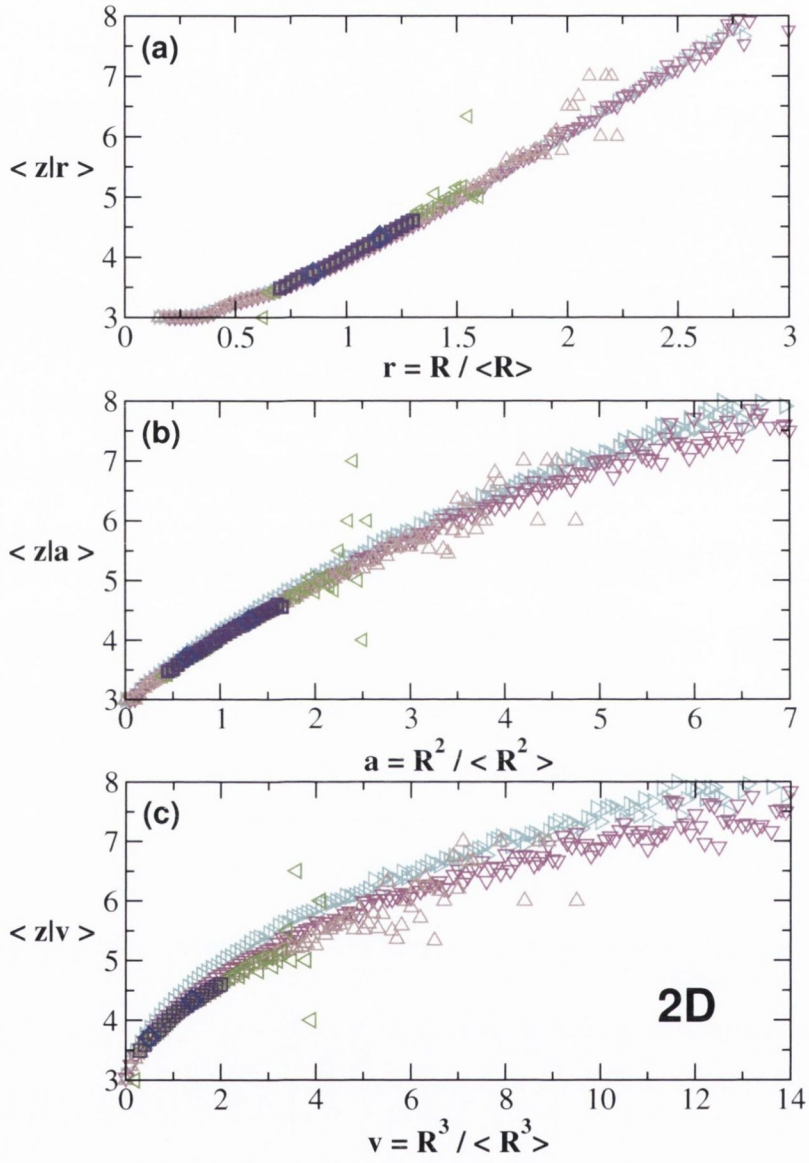

Figure 3.2.4: The average of the contact number distribution for a particle of a given size for the six different size distributions at ϕ_c in 2D: ($\Diamond$) bidisperse, radius ratio 1:1.4; ($\triangleleft$) lognormal $\sigma_R = 0.10$; ($\square$) uniform $\sigma_R = 0.17$; ($\triangle$) Gaussian $\sigma_R = 0.24$; ($\triangledown$) lognormal $\sigma_R = 0.35$; ($\triangleright$) lognormal $\sigma_R = 0.45$. We present three different scalings: (a) in terms of the normalised radius r; (b) in terms of the normalised area a; (c) in terms of the normalised volume v. The data are plotted over a range so that deviations from a perfect collapse can be discerned.

obtained from this second algorithm, a Gaussian size distribution $\sigma_R = 0.28$ and close to ϕ_c with $\langle z \rangle = 4.06$, plotted in 3.2.5, corroborates the results found with the conjugate gradient minimization algorithm. Therefore, the results do not depend upon the packing algorithm.

The results shown in Figure 3.2.5 suggests that all the conditional probabilities $P(z|r)$ collapse in 2D similar to that already seen in 3D. This is confirmed in Figure 3.2.6, where for each r interval plotted, all the $P(z|r)$ collapse independent of size distribution.

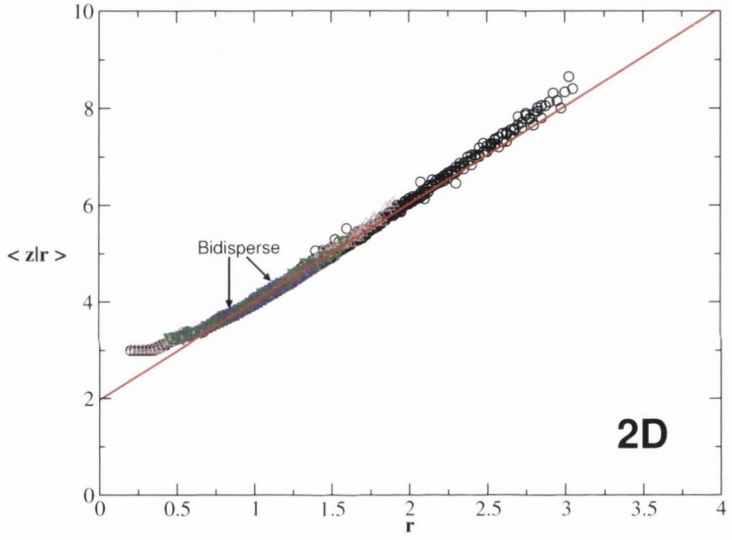

Figure 3.2.5: The average contact number for particles of a given radius r at ϕ_c in 2D for all ($\Diamond$) bidisperse, ($\square$) uniform, ($\triangle$) Gaussian, ($\triangledown$) Gaussian using bubble model code and ($\circ$) lognormal size distributions at all the widths σ_R we have considered (see Figure 2.3.2). The solid red line is a fit to Equation (3.2.6).

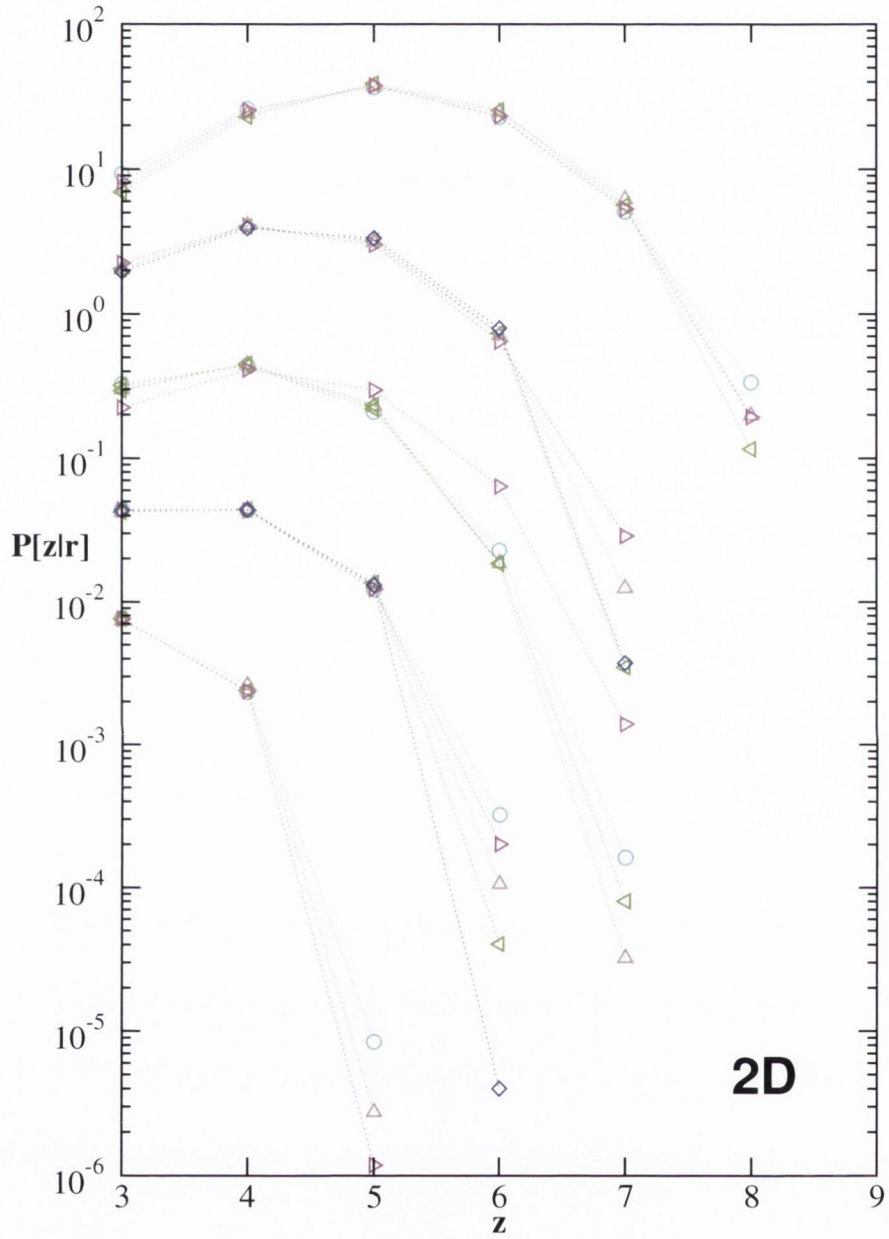

Figure 3.2.6: The contact number distribution for discs of a given radius r, $P(z|r)$ for the same size distributions as plotted in the the inset of Figure 3.2.4 at ϕ_c. Plotted here is a selection of $P(z|r)$ for five different intervals r with $P(z|r)$ for each interval shifted on the y-axis for clarity. Plotted in order of lowest to highest is $0.475 < a < 0.525$; $0.825 < a < 0.875$; $0.975 < a < 1.025$; $1.125 < a < 1.175$; $1.475 < a < 1.525$.

3.3 Mean Field Granocentric Model

In Section 3.1, we outlined the granocentric approach. In this section we draw inspiration from that approach to propose a model that will describe the contact number distribution of polydisperse packings. Given the results shown in Section 3.2, we will now develop a mean field granocentric model to describe these correlations.

3.3.1 Mean Field Granocentric Model in 3D

We have shown that the contact number distribution $P(z|a)$ for particles of a given size at ϕ_c depends not on the global size distribution of the packing but only on the size of the particle in question. This allows us to formulate a mean field granocentric model that is similar in spirit to the one of Newhall et al. [59], who investigated size-topology relations in tessellated packings.

If we consider a particle of a given radius R_c, we can then make a mean field assumption that all the particles surrounding it are of average radius $\langle R \rangle$ since local correlations are independent of the size distributions. This is a similar 'granocentric' approach to that taken by Clusel et al. [50]. In contrast to the original granocentric model [50], we explicitly exclude rattlers since their contact number is ill-defined.

In more detail, if a particle of size R_c is in contact with another particle of size R, the particle of size R will subtend a solid angle Ω of the central particle, which as in Corwin et al. [44], is given by

$$\Omega(R_c, R) = 2\pi \left(1 - \frac{1}{1 + \frac{R}{R_c}} \sqrt{1 + \frac{2R}{R_c}} \right). \tag{3.3.1}$$

Since the correlation between contact number and size appear independent of polydispersity, when scaled with a, we introduce our mean field assumption and rewrite Equation (3.3.1) with all contacting particles now assumed to

have an average radius $\sqrt{\langle R^2 \rangle}$:

$$\Omega(R_c, \sqrt{\langle R^2 \rangle}) = 2\pi \left(1 - \frac{1}{1 + \frac{\sqrt{\langle R^2 \rangle}}{R_c}} \sqrt{1 + \frac{2\sqrt{\langle R^2 \rangle}}{R_c}} \right). \tag{3.3.2}$$

For a particle of size a, this expression can be reformulated to give the solid angle subtended by any single contact as

$$\Omega(a) = 2\pi \left(1 - \frac{\sqrt{a}}{1 + \sqrt{a}} \sqrt{1 + \frac{2}{\sqrt{a}}} \right). \tag{3.3.3}$$

The maximum number of contacts a particle can have is simply

$$Z_{max}(a) = \left\lfloor \frac{4\pi}{\Omega(a)} \right\rfloor. \tag{3.3.4}$$

A correction must be made to Z_{max} to account for the interstices, similar to the familiar sphere kissing problem for monodisperse spheres where only 12 spheres can be in contact with a central sphere even though there is sufficient solid angle to fit 14 spheres [65].

A free parameter α is introduced into the model to limit the maximum number of contacts:

$$Z_{max}(a) = \left\lfloor \frac{2\alpha}{1 - \frac{\sqrt{a}}{1+\sqrt{a}} \sqrt{1 + \frac{2}{\sqrt{a}}}} \right\rfloor. \tag{3.3.5}$$

In order to recover the known result of the kissing problem for monodisperse spheres, the value of α would have to be 0.8708. In our model, however, the value of α will turn out to be less than that due to additional constraints.

We now make an ansatz that the distribution of number of particles in

contact with a particle of size a is given by a binomial distribution.

$$\begin{aligned} P(z|a) &= B(z; Z_{max}(a), p), \\ &= \frac{Z_{max}!}{z!(Z_{max}-z)!} p^z (1-p)^{Z_{max}-z}, \end{aligned} \tag{3.3.6}$$

where $B(z; Z_{max}(a), p)$ is a binomial distribution with Z_{max} giving the number of trials, that is the number of attempts to place particles in contact with the central particle of size a. p is the acceptance probability that a particle will be in contact. The probability p is the second free parameter in the model.

In order to omit rattlers, we truncate the binomial distribution for $z < 4$ by including a Heaviside function $H(z-4)$ and a normalisation constant C, so $P(z|a)$ becomes,

$$\begin{aligned} P(z|a) &= B'(z; Z_{max}(a), p), \\ &= C \frac{Z_{max}!}{z!(Z_{max}-z)!} p^z (1-p)^{Z_{max}-z} H(z-4), \end{aligned} \tag{3.3.7}$$

where C is given as,

$$C = \frac{6(1-p)^{Z_{max}}}{6(1-p)^3((\frac{1}{1-p})^{Z_{max}} - 1) - pZ_{max}(6 + p(11p-15) + pZ_{max}(pZ_{max} - 6p + 3))}. \tag{3.3.8}$$

Note that this is in contrast to the original granocentric model which did not exclude rattlers. This allows us to make a prediction for the contact number average for a given particle size,

$$\langle z|a \rangle = \sum_{z=4}^{Z_{max}(a)} zP(z|a), \tag{3.3.9}$$

and the corresponding variance of the contact number for a given particle

size

$$\langle \sigma_Z^2 | a \rangle = \left(\sum_{z=4}^{Z_{max}(a)} z^2 P(z|a) \right) - \langle z|a \rangle^2, \tag{3.3.10}$$

as well as a prediction of the global contact number distribution of the packing

$$P(z) = \int_0^\infty P(z|a)P(a)da. \tag{3.3.11}$$

Given a size distribution $P(a)$ and using Equation (3.3.7), a prediction for the contact number distribution can be made for any packing at ϕ_c. The acceptance probability p can be determined through a property of the binomial distribution. If $X \sim B(n,p)$ is a random variable taken from a binomial distribution B with n trials and acceptance probability p, then the mean is given by

$$E[X] = np,$$

and the variance is given by

$$Var[X] = np(1-p).$$

Thus, the ratio of the variance to the mean of a binomial distribution is a constant given in terms of p, which in the notation of our model gives

$$\frac{\langle \sigma_Z^2 | a \rangle}{\langle z|a \rangle} = 1 - p, \tag{3.3.12}$$

which allows a value of p to be found from the simulation data.

Equation (3.3.7) is a truncated binomial distribution and therefore the ratio $\frac{\langle \sigma_Z^2 | a \rangle}{\langle z|a \rangle}$ plotted in Figure 3.3.1 is only expected to reach a constant at sufficiently large values of a, where the effect of truncation is negligible. As mentioned, for values $a > 3$ the number of occurrences of particles of that size becomes low and results in scatter in the calculated ratio. For $a \gtrsim 2$ the ratio

plateaus at 0.342 ± 0.006 (dashed line in Figure 3.3.1), which corresponds to $p = 0.658 \pm 0.006$. This fixes the p parameter of our model.

After obtaining the probability p directly from the data, we can fix the second parameter α by imposing the additional constraint given by Equation (3.3.13), namely that the global average contact number of the packing $\langle z \rangle$ must be equal to 6. The free parameter α can be fixed by integrating the prediction from Equation (3.3.9) over the size distribution such that

$$\langle z \rangle = \int_0^\infty \langle z|a \rangle P(a) da = 6. \tag{3.3.13}$$

This results in α taking a value of 0.625. Surprisingly, α *does not* depend on

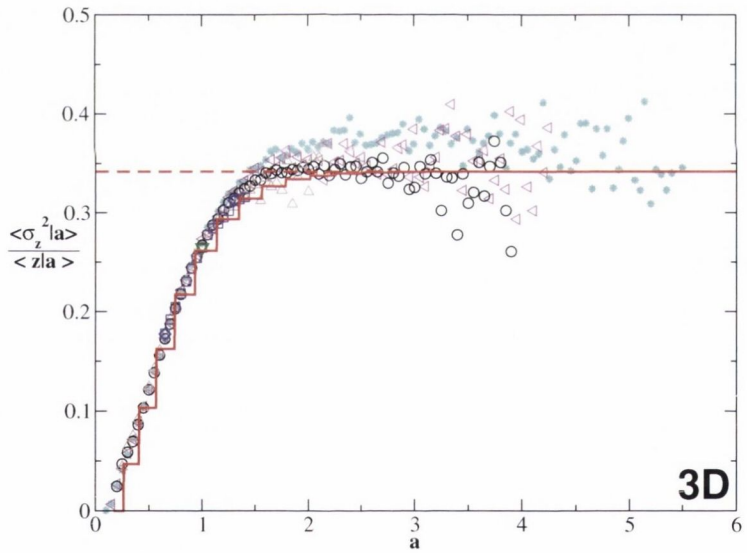

Figure 3.3.1: The ratio of the variance to the average of the contact number distribution for particles of a given size at ϕ_c for the same size distributions as in Figure 3.2.1. The dashed line denotes the value of the acceptance probability p as found from the data and the solid line identifies the model prediction of this ratio.

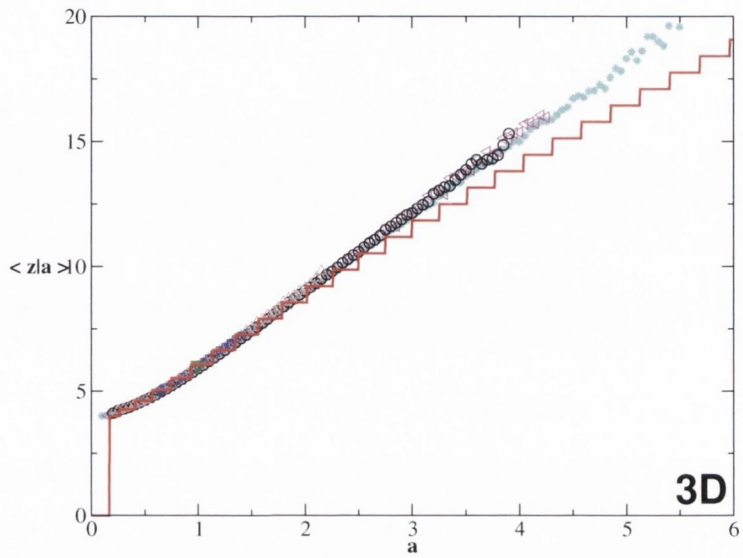

Figure 3.3.2: The average of the contact number distribution for particles of a given size at ϕ_c for the same size distributions as in Figure 3.2.1. The model prediction (Equation (3.3.9)) is plotted as the solid red line.

polydispersity, therefore the two free parameters of the model, α and p, can be fixed for all size distributions at ϕ_c. This may be related to the fact that ϕ_c without rattlers, which are explicitly omitted in this model, is a constant (Figure 2.3.2).

The constancy of the two parameters is a significant simplification to the original granocentric model, where the acceptance probability and maximum solid angle need to be determined for each polydispersity separately.

Plotting the prediction of the average $\langle z|a \rangle$ from Equation (3.3.9) against the average $\langle z|a \rangle$ from the data plotted in Figure 3.2.2 in Figure 3.3.2, it can be seen over a large range of a that the model prediction is in good agreement with the data. Only for large values of a does it deviate slightly. The staircase structure of the model prediction seen in Figure 3.2.2 is due to the discrete nature of the binomial distribution.

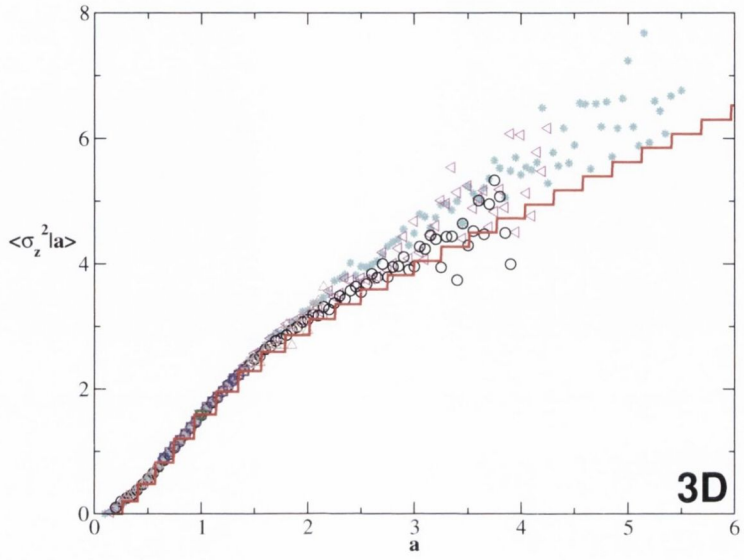

Figure 3.3.3: The variance of the contact number distribution for particles of a given size at ϕ_c for the same size distributions as Figure 3.2.1. The model prediction from Equation (3.3.10) is plotted as the solid red line.

Similarly, we can compare Equation (3.3.10) against the variance $\langle \sigma_Z^2 | a \rangle$ from the data in Figure 3.3.3. It can be seen over a large range of a that the model prediction is in good agreement with the data. Only for large values of a does the prediction begin to deviate from the data, this may be attributed to scatter due to low statistics. In both Figures 3.3.2 and 3.3.3 it can been seen that at low a there is a minimum size of particle predicted by the model. For this value of α the model predicts a non-zero $\langle z|a \rangle$ for $a > 0.14$, below this size a particle cannot form enough contacts to be locally stable, hence the prediction going to zero in Figure 3.3.2. The variance vanishes for $a \leq 0.26$ in Figure 3.3.3 because the maximum contact number predicted by the model is 4 for particles of that size. In both cases the data plotted takes a non-zero value below that predicted by the model but vanishes for $a > 0$.

Again we can compare the prediction of the distribution $P(z|a)$ from

Equation (3.3.7) against the conditional probability distributions from the data plotted in Figure 3.2.3, in Figure 3.3.4. Figure 3.3.4 reveals some new information about the model, namely that for low values of a, that is $a \leq 2$, the prediction of the distribution is extremely accurate but does not predict the low probability of occurrences for large z (indeed some are explicitly not allowed by the model parameters) but for larger $a \geq 2$, the model accurately predicts the full distribution but also accounts for low values of z that do not occur in simulations.

Finally, we can match our prediction for the contact number distribution given a size distribution from Equation (3.3.11) to the contact number distribution from the data. For all the distributions plotted in Figure 3.3.5 there is very good agreement between the prediction and simulation data. The same parameters α and p are used for all the size distributions. For the continuous size distributions, the model predicts the $P(z)$ of the simulation data excellently. There are only slight deviations between model and data for large values of z. For the discrete size distributions though there is a discrepancy for higher values of z. This model appears to be unable to capture the low probability particles that have very many contacts for their size. However, the model is in very good agreement with $P(z)$ for low z.

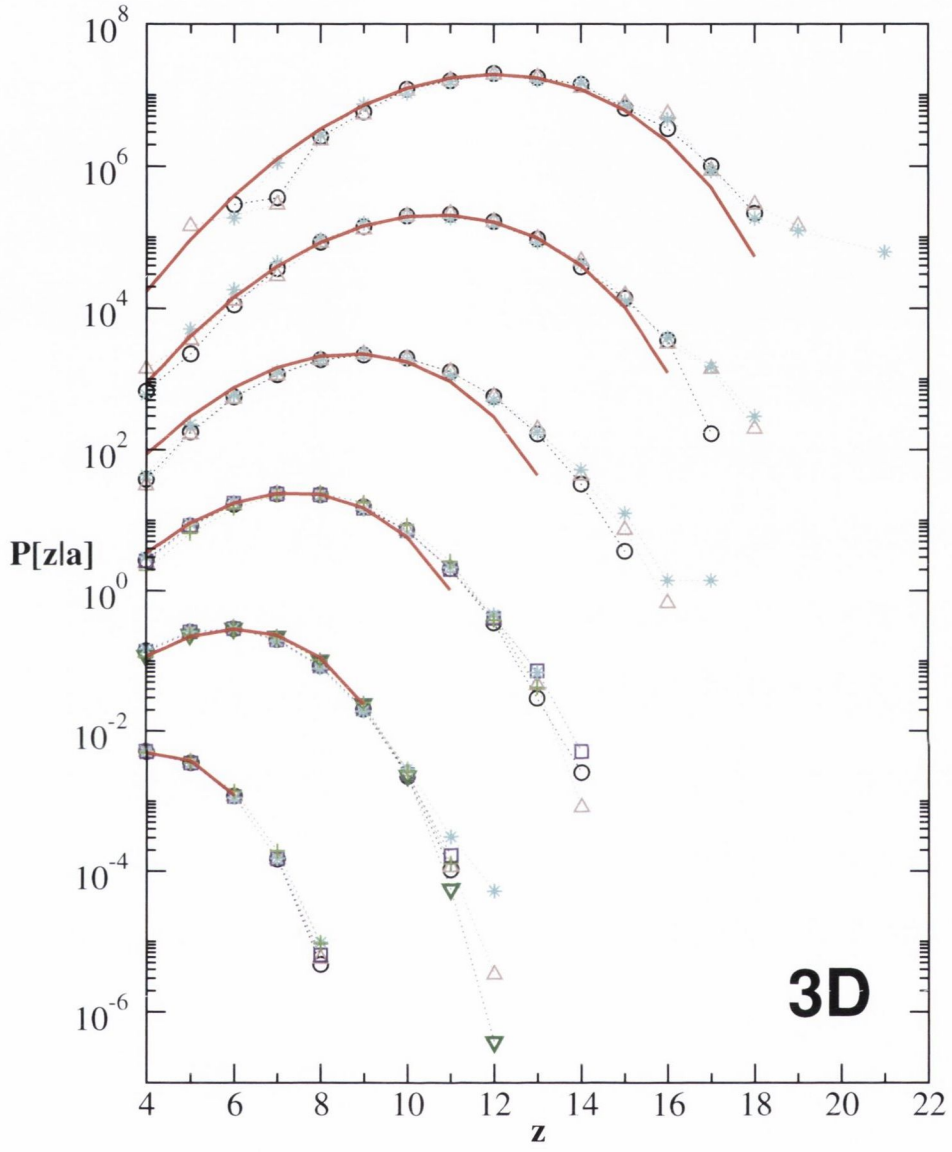

Figure 3.3.4: The contact number distribution for particles of a given size $P(z|a)$ for the same size distributions as Figure 3.3.2 at ϕ_c. Plotted here is a selection of the $P(z|a)$ for six different intervals a with $P(z|a)$ for each interval shifted on the y-axis for clarity. Plotted in order of lowest to highest is $0.475 < a < 0.525$; $0.975 < a < 1.025$; $1.475 < a < 1.525$; $1.975 < a < 2.025$; $2.475 < a < 2.525$; $2.975 < a < 3.025$. The solid red line model prediction of the distributions from Equation (3.3.7).

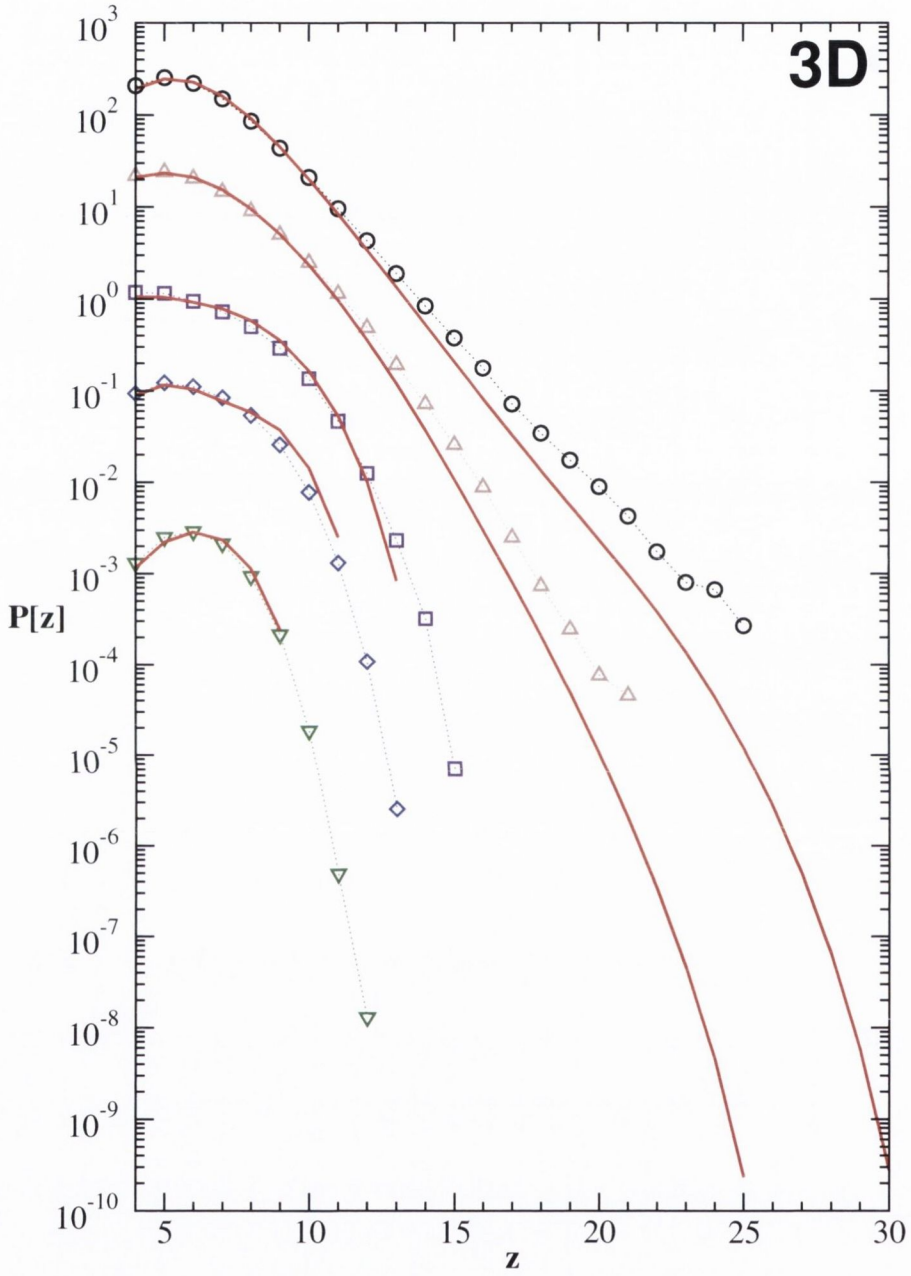

Figure 3.3.5: The contact number distribution for a number of polydispersities at ϕ_c. The open symbols represent the simulation data and the solid red line represents the model prediction from Equation (3.3.11). Data is labelled the same as in Figure 3.3.4 with the addition of the bidisperse data set ($\Diamond$).

3.3.2 Comparison with Original Granocentric Model

In Figure 3.3.6, using data provided by Clusel [66] from the original granocentric model, a comparison is made between the original granocentric model described in [44] and the mean field model outlined in this thesis. Predominantly both models describe the data well, however the original granocentric model does not capture the large z behaviour.

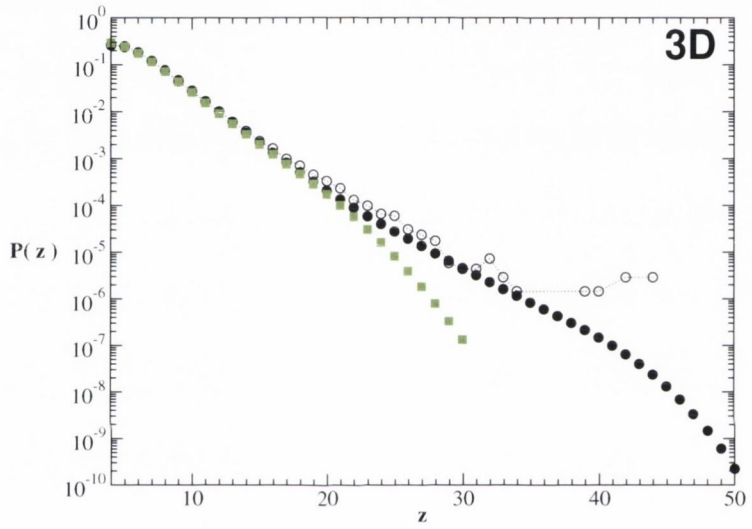

Figure 3.3.6: Comparison with the original granocentric model. The contact number distribution for a lognormal size distribution ($\sigma_R = 0.28$) ($\circ$) for simulation is compared with the prediction of the original granocentric model ($\bullet$) and the mean-field model described here ($\bullet$). Data from the granocentric model prediction provided by Clusel [66].

3.3.3 Mean Field Granocentric Model in 2D

A similar treatment to that used in three dimensions works in two dimensions. In Figure 3.3.7 we plot the two dimensional equivalent of Figure 3.3.2, except with the size of the particle now represented by the normalised radius r instead of the normalised surface area a. The model prediction plotted in Figure 3.3.7(a) for $\langle z|r\rangle$ is similar to the model outlined in the previous section. The principle adjustment is that the maximum number of discs that can be placed in contact with a disc of radius r must now be expressed in terms of the available angle rather than the available solid angle. Now, Equation (3.3.5) is altered for two dimensions to read as

$$Z_{max}(r) = \left\lfloor \frac{\alpha\pi}{\sin^{-1}\left(\frac{1}{1+r}\right)} \right\rfloor . \tag{3.3.14}$$

Another consideration is that in two dimensions, rattlers are particles with less than 3 contacts rather than 4.

The two free parameters of the system are affected by this change of dimension. The acceptance probability p can be found as before from the ratio between the variance of the contact number for particles of a given radius $\langle \sigma_Z^2|r\rangle$ and the average $\langle z|r\rangle$, seen in Figure 3.3.7(c), which goes to a constant value for sufficiently large values of r. The value for p found from the data plotted in Figure 3.3.7(c) is 0.78 ± 0.02.

The value of the contact limiting parameter α changes with the change of dimension. Analogous to the 3D case (Equation (3.3.13)), α is determined by the isostatic constraint, which is

$$\langle z\rangle = \int_0^\infty \langle z|r\rangle P(r)dr = 4, \tag{3.3.15}$$

in two dimensions with the size distribution now given in terms of r rather than a. The value of α for two dimensions is found to be 0.894. The equiva-

lent value of α that would recover the correct answer for the kissing problem in 2D is 1.

The justification for this model is that the correlation between size and contact number is independent of of polydispersity, analogous to the results in three dimensions. Similar to Figure 3.3.4, a number of different size distributions are plotted for given intervals of r in Figure 3.3.8. For each r interval plotted, all the $P(z|r)$ collapse independent of size distribution, therefore validating the basis of the model. However, Figure 3.3.8 highlights some of the weaknesses of the model, which are particularly illustrated for the lowest interval of r where the data shows a range of contact numbers z but the model predicts that only 3 discs can fit around a disc of that size. This discrepancy at low r is due the influence of the maximum contact limiting parameter α. This limiting parameter results in the model prediction of $\langle z|r\rangle$ vanishing for $r \leq 0.24$ and $\langle \sigma_z^2|r\rangle$ for $r \leq 0.55$. For large values of r the model prediction for the distribution of contacts around a disc of a given radius is in better agreement.

The global contact distribution can then be predicted from the two dimensional equivalent of Equation (3.3.11),

$$P(z) = \int_0^\infty P(z|r)P(r)dr. \tag{3.3.16}$$

In Figure 3.3.9, it is shown that there is good agreement between the predictions and data for a large range of σ_R and different types of size distribution. Similar to results in three dimensions, for wider size distributions the prediction is in closer agreement with the data.

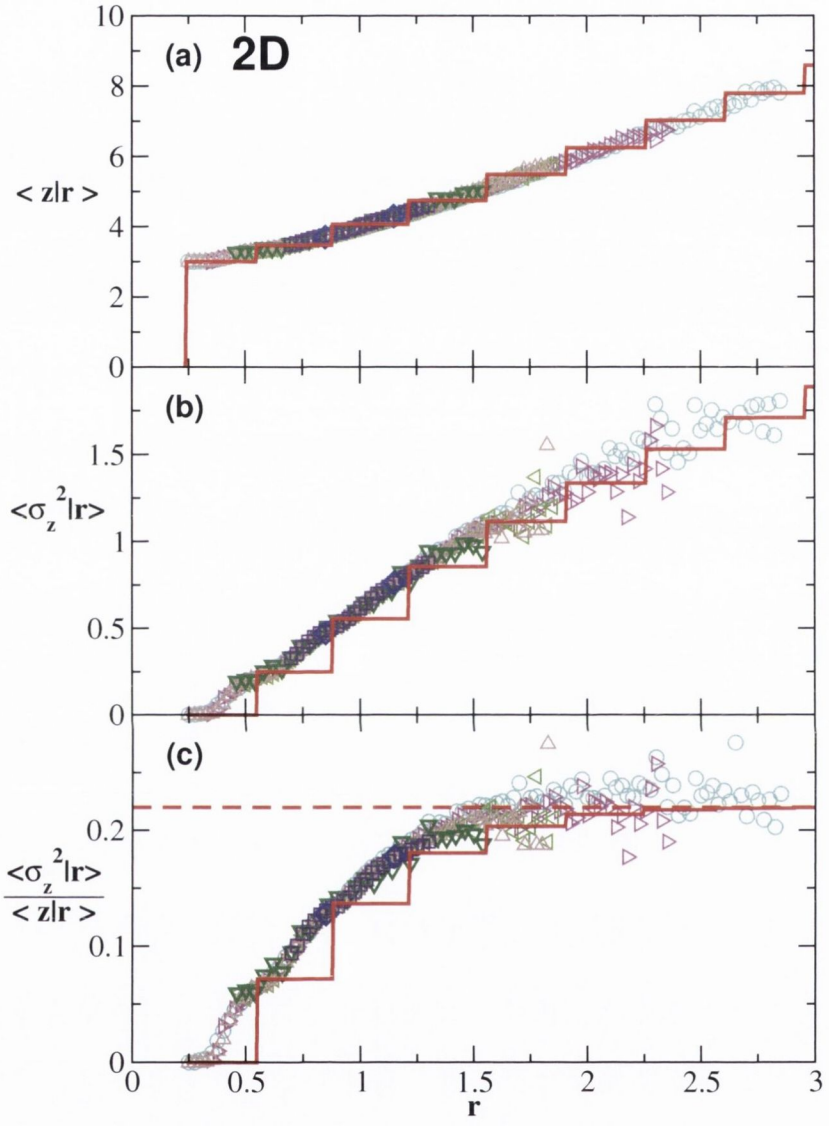

Figure 3.3.7: (a) The average of the contact number distribution for particles of a given radius r in 2D for a number of different size distributions at ϕ_c. The data is labelled the same as in Figure 3.2.4 with the addition of ($\triangledown$) Gaussian $\sigma_R = 0.28$ using the bubble model code. In all three panels, the model prediction for that quantity is plotted as the solid red line. (b) The variance $\langle \sigma_Z^2 | r \rangle$ for the same size distributions. (c) The ratio of the variance to the average of the contact number distribution for particles of a given size r. The dashed red line denotes the value of the acceptance probability p as found from the data.

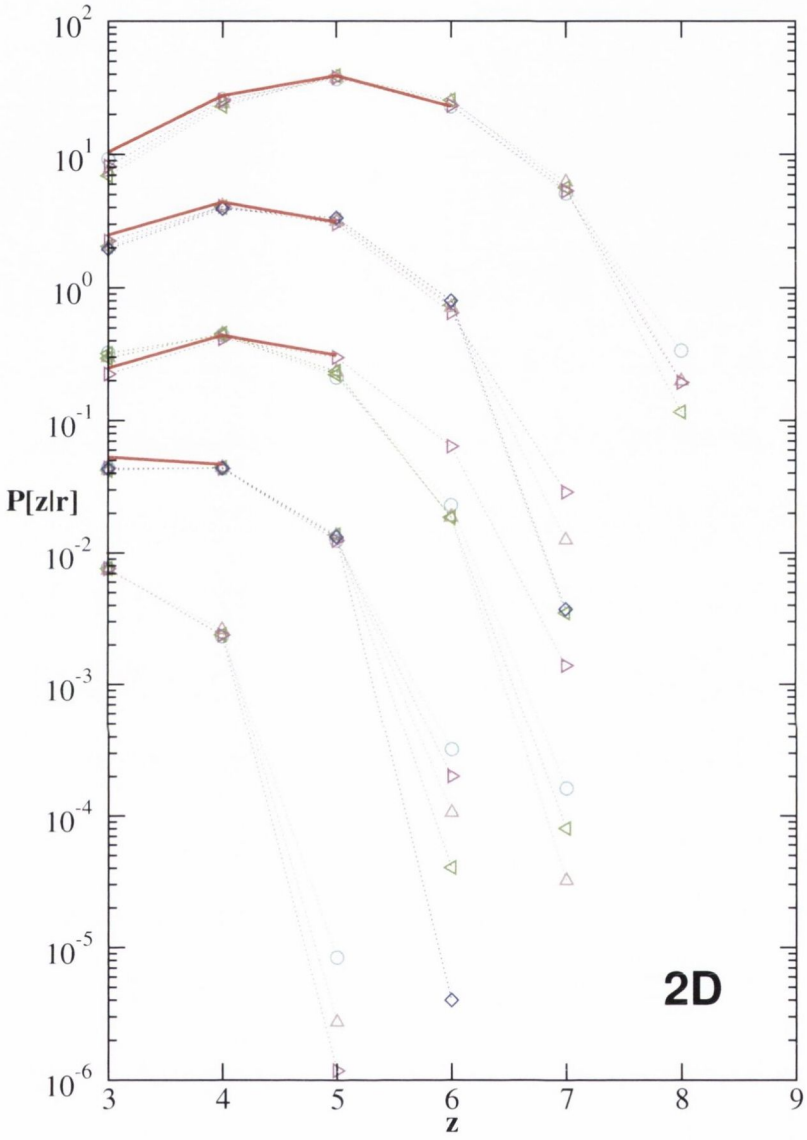

Figure 3.3.8: The contact number distribution for discs of a given radius r, $P(z|r)$ for the same size distributions as plotted in the the inset of Figure 3.3.7 at ϕ_c. Plotted here is a selection of $P(z|r)$ for five different intervals r with $P(z|r)$ for each interval shifted on the y-axis for clarity. Plotted in order of lowest to highest is $0.475 < a < 0.525$; $0.825 < a < 0.875$; $0.975 < a < 1.025$; $1.125 < a < 1.175$; $1.475 < a < 1.525$. The solid red line is the model prediction of $P(z|r)$.

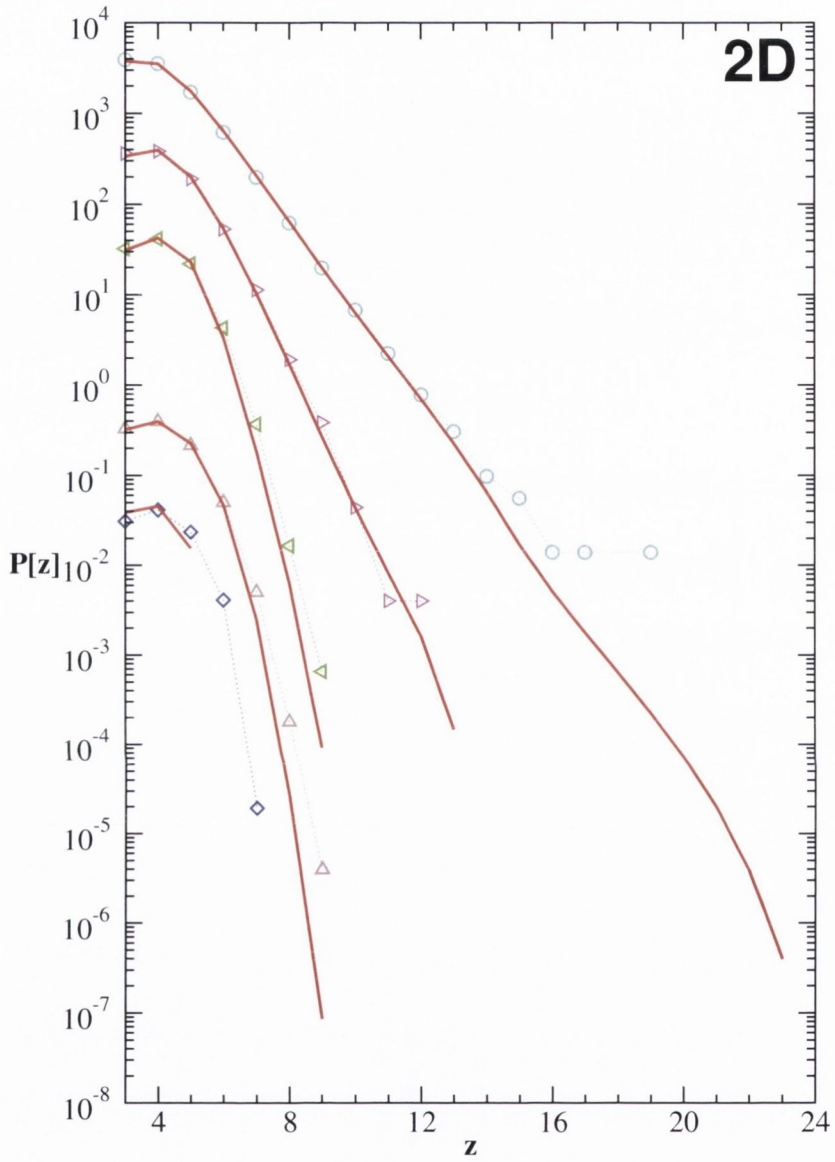

Figure 3.3.9: The contact number distribution for a number of different polydispersities at ϕ_c in two dimension. The data from simulation is plotted as open symbols and the prediction from the model is plotted as the solid red line. The parameters $p = 0.78$ and $\alpha = 0.894$ are used for all size distributions. The same size distributions are plotted with the same symbols as in Figure 3.3.7.

3.3.4 Conclusions & Outlook

We have shown that a surprising number of features of frictionless packings are insensitive to polydispersity.

Our key result is the universal correlations we observe between size and contact number of a particle, which are independent of the shape and width of the size distribution. This holds in both two and three dimensions and allows a mean field formulation of the granocentric model. The contact number distributions emerging from the model agree well with the data for a wide range of polydispersities. The two parameters that appear in the model are also found to be insensitive to polydispersity.

While the binomial distribution is a good approximation for $P(z|a)$ and $P(z|r)$, it does not capture the whole distribution. Particularly, there is a tendency to overlook the existence of large z occurring for large particles. It remains a subject for investigation of whether another distribution can provide a superior description of $P(z|a)$ and $P(z|r)$.

3.4 Particle Size with Contact Number z

In this section we look at the opposite correlation to that studied in Section 3.2, and investigate how a packing at ϕ_c is structured when viewed from a particle with a given contact number. This is an approach that has been taken before in the study of force networks [67] and of disordered cellular structures [68, 69]. We will now investigate how the correlations found in the first part of this chapter change when inspected in this manner.

3.4.1 Three Dimensions

Though we have shown a link between the surface area available to a particle in a polydisperse random close packed packing and its average contact number, and that this relationship is independent of the size distribution, it is important to emphasise that the converse is not necessarily true. The average area of particles that have z contacts, $\langle a|z\rangle$, is not equal to $\langle z|a\rangle$. The average $\langle a|z\rangle$ is defined as

$$\langle a|z\rangle = \int_0^\infty aP(a|z)da. \tag{3.4.1}$$

In the bottom inset of Figure 3.4.1, it shown that $\langle a|z\rangle$ is not independent of size distribution. The $\langle a|z\rangle$ of continuous size distributions, lognormal and Gaussian, that have tails in $P(a)$, are fit by

$$\langle a|z\rangle = 1 + \lambda(z - \langle z\rangle), \tag{3.4.2}$$

and in Figure 3.4.1 show good agreement with a range of polydispersities. When rescaled by the fitting parameter λ, the $\langle a|z\rangle$ for all lognormal and Gaussian size distributions collapses, as seen in the top inset of Figure 3.4.1. While the overall trend of $\langle a|z\rangle$ for lognormal and Gaussian distributions is linear, there are deviations. The size distributions that lack tails have a

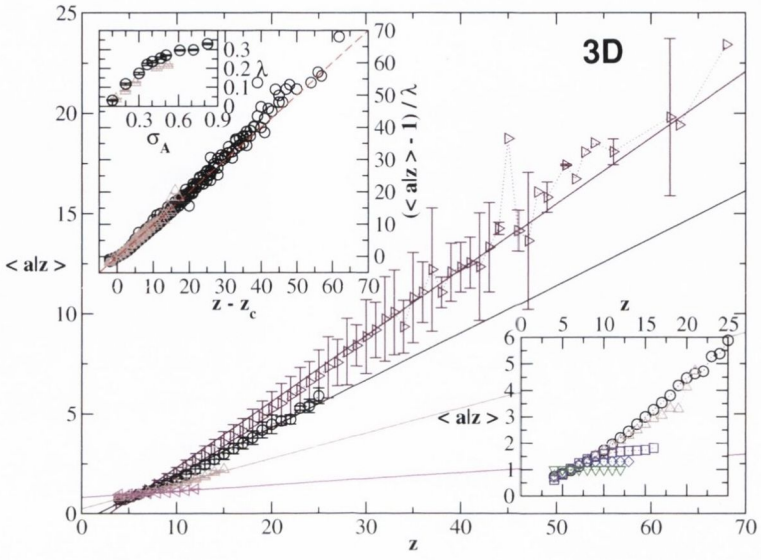

Figure 3.4.1: The average area of particles with a given contact number for four different size distributions in three dimensions at ϕ_c: (◁) lognormal $\sigma_R = 0.05$; (△) Gaussian $\sigma_R = 0.14$; (○) lognormal $\sigma_R = 0.20$; (▷) lognormal $\sigma_R = 0.36$. The solid lines are fits to Equation (3.4.2). The top inset shows the average area of particles with a given contact number for all (○) lognormal and (△) Gaussian size distributions at ϕ_c, collapsed by fitting the data to Equation (3.4.2). The dashed red line corresponds to a slope of 1. Inset of the top inset shows the fit parameter λ as a function of σ_A. The bottom inset shows relationship between $\langle a|z \rangle$ versus z for the same size distributions as plotted in Figure 3.3.5.

different functional form in $\langle a|z \rangle$ because there are large populations of large spheres that can take a range of z as seen in Figure 3.3.4. Without a tail in the bidisperse and uniform size distributions, the plateau of $\langle a|z \rangle$ seen in the bottom inset of Figure 3.4.1 results. This linear relationship between size and contact number is similar to a relationship known to exist in two-dimensional cellular structures and is known as Lewis' law [69]. This link between the arrangement of cellular structures and that of disordered packings will be explored further in Chapters 4 and 5.

The two different relationships between a and z (Equations (3.4.2) and (3.2.3)) arise from being calculated from two different conditional probabilities, the discrete distribution $P(z|a)$ and the continuous distribution $P(a|z)$, which are related by Bayes Theorem [70],

$$P(z|a) = P(a|z)\frac{P(z)}{P(a)}. \tag{3.4.3}$$

As described in the previous section, $P(z)$ and $P(a)$, in addition to being discrete and continuous distributions respectively, are related but are not the same. Hence the fitting parameter λ is not equal to the inverse of γ, which we recall is the fitting parameter of Equation (3.2.3).

From Equation (3.4.3), the two conditional averages $\langle z|a\rangle$ and $\langle a|z\rangle$ can be related by

$$\int_0^\infty a\langle z|a\rangle P(a)da = \sum_{z=4}^{\infty} z\langle a|z\rangle P(z). \tag{3.4.4}$$

Then by substituting the linear fits of Equation (3.2.3) and Equation (3.4.2) into Equation (3.4.4) a relationship can be found between the width of the size distribution and the width of the contact number distribution,

$$\sigma_Z^2 = \frac{\gamma}{\lambda(\sigma_A)}\sigma_A^2, \tag{3.4.5}$$

where σ_A is the standard deviation of the normalised surface area distribution with rattlers omitted and is defined as,

$$\sigma_A = \sqrt{\frac{\langle R^4\rangle}{\langle R^2\rangle^2} - 1}. \tag{3.4.6}$$

This is not trivially related to σ_R and is a useful measure of the size distribution of packings in 3D.

While γ is a constant, the fitting parameter λ from Equation (3.4.2) is a function of σ_A. This is seen in the inset of the top inset of Figure 3.4.1.

3.4.2 Two Dimensions

Similar correlations are also observed in two dimensions. By defining the average radius for particles with a given contact number $\langle r|z\rangle$ as,

$$\langle r|z\rangle = \int_0^\infty rP(r|z)dr, \tag{3.4.7}$$

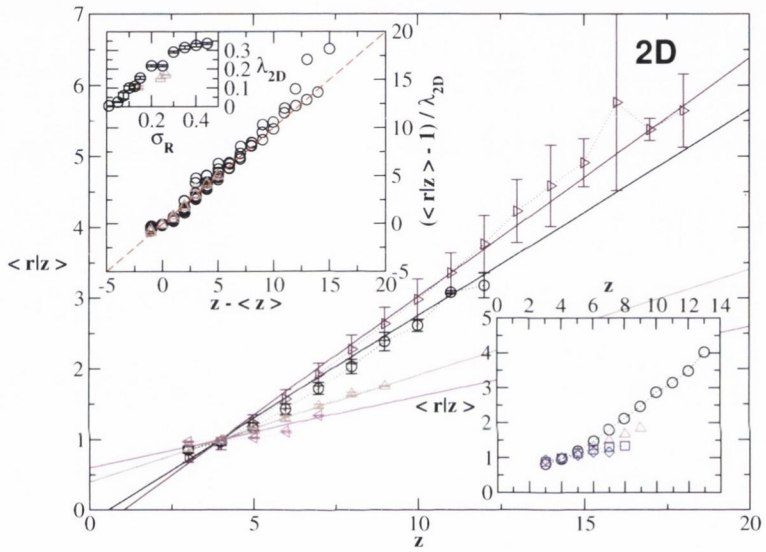

Figure 3.4.2: The average radius of particles with a given contact number for four different size distributions in two dimensions at ϕ_c: (◁) lognormal $\sigma_R = 0.10$; (△) Gaussian $\sigma_R = 0.24$; (○) lognormal $\sigma_R = 0.30$; (▷) lognormal $\sigma_R = 0.45$. The solid lines are fits to Equation (3.4.8). The top inset shows the average area of particles with a given contact number for all (○) lognormal and (△) Gaussian size distributions at ϕ_c, collapsed by fitting the data to Equation (3.4.8). The dashed red line corresponds to a slope of 1. Inset of the top inset shows the fit parameter λ as a function of σ_A. The bottom inset shows relationship between $\langle a|z\rangle$ versus z for the size distributions: (◇) bidisperse; (□) uniform $\sigma_R = 0.23$; (△) Gaussian $\sigma_R = 0.27$; (○) lognormal $\sigma_R = 0.35$.

a relationship similar to Equation (3.4.2) found in three dimensions can be written for two dimensions. The equation,

$$\langle r|z\rangle = 1 + \lambda_{2D}(z - \langle z\rangle), \tag{3.4.8}$$

is then fit to $\langle r|z\rangle$ of the two-dimensional Gaussian and lognormal distributions in Figure 3.4.2 with good agreement. In the bottom inset of Figure 3.4.2, as seen for three dimensions, the distributions without tails plateau for large z, though this is less pronounced than in three dimensions due to the smaller range of contact numbers. In the top inset of Figure 3.4.2, all the lognormal and Gaussian data are rescaled such that a trend with slope 1 would indicate agreement between the data and Equation (3.4.8). The correlation between size and contact number is well described by Equation (3.4.8). The fitting parameter of Equation (3.4.8), λ_{2D}, is plotted in the inset of the top inset of Figure 3.4.2 and is a function of the polydispersity.

Through an analysis similar to that described in the previous section for three dimensions, a relationship between the standard deviations of the size distributions and the contact number distributions can be written,

$$\sigma_Z^2 = \frac{\gamma_{2D}}{\lambda_{2D}(\sigma_R)}\sigma_R^2. \tag{3.4.9}$$

The prediction of the contact number variances σ_Z^2 made for 3D and 2D by Equation (3.4.5) and (3.4.9) are plotted in Figure 3.4.3 and its inset. The behaviour of σ_Z^2 in 3D, adheres to a much clearer linear trend when plotted in terms of σ_A^2 than the trend of σ_Z^2 with σ_R^2 plotted in Figure 2.3.5. The agreement between Equation (3.4.5) and the 3D data is best for broad distributions but less accurate for narrow distributions where $\langle a|z\rangle$ is not well approximated by the linear fit of Equation (3.4.2). Equation (3.4.9) fits the 2D data best for wider distributions as well. For the narrow distributions σ_Z^2 is not captured as well as it was in 3D. This discrepancy can be attributed to the same reasons as advanced for 3D but is also in some part due to

the partial crystallisation that occurs in 2D for $\sigma_R < 0.1$. The type of size distribution used appears to have an effect with predictions of the contact number variance for Gaussian distributions being more accurate than those made for lognormal distributions.

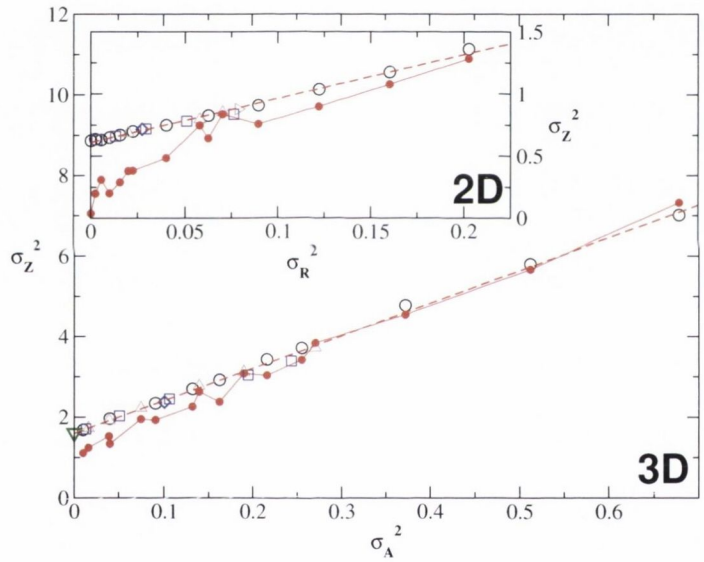

Figure 3.4.3: Relationship between the variance of the area distribution σ_A^2 and the variance of the contact number distribution σ_Z^2. The dashed line corresponds to a linear fit to the data: $\sigma_Z^2 = 1.60 + 8.09\sigma_A^2$. The closed symbols (•) are the predictions from Equation (3.4.5). Plotted in the inset is the variance σ_Z^2 versus the variance of the radius distribution σ_R^2 for two dimensional packings. The dashed line corresponds to a linear fit to the data: $\sigma_Z^2 = 0.61 + 3.52\sigma_R^2$. The closed symbols (•) are the predictions from Equation (3.4.9). The data is labelled the same as in Figure 2.3.2.

3.4.3 Conclusions

Despite the correlations shown to be independent of polydispersity when viewed from the perspective of particle size, when viewed from the standpoint of contact number, the relationship between contact number and size becomes more complex. The relationship between these approaches is not straightforward. However, the behaviours of $\langle a|z\rangle$ in 3D and $\langle r|z\rangle$ in 2D are found to be linear with contact number for packings with sufficiently wide tails in their size distribution.

The linear relationship found in this section, along with the linear relationship found in Section 3.2, allows for a prediction of the global contact number variance, given information on the variance of the size distribution.

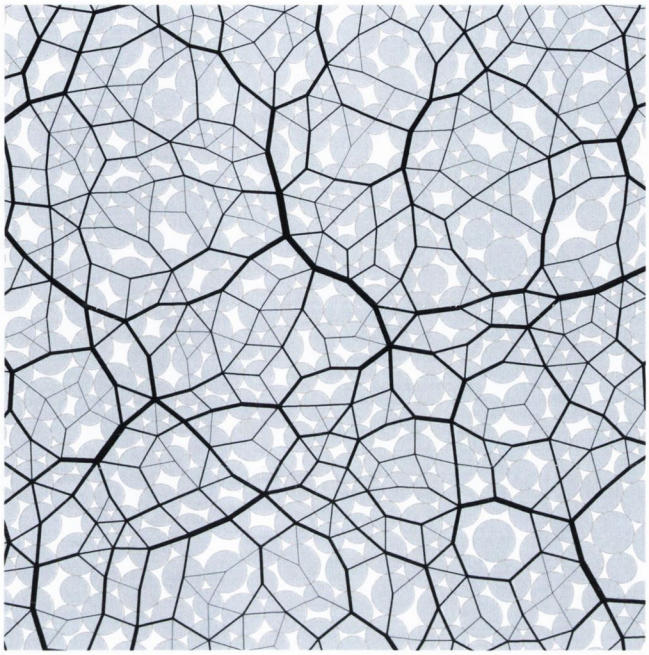

Figure 3.5.1: Visualisation of a 2D soft disc packing simulation at ϕ_c with a bidisperse distribution of radii. The discs are linked by a solid black line when in contact and the thickness of the line is proportional to the strength of the interaction.

3.5 The Force Network in Disordered Packings

We have shown that disordered packings have various local contact correlations that are independent of polydispersity. This has allowed a connection to be made between the size distribution and the contact number distribution. The next natural step is to investigate whether the distribution of forces can similarly be predicted from the size distribution. Previous work on the local structure of the force distribution at ϕ_c has focussed on the existence of force chains [60, 61]. A 2D example of force chains is plotted in Figure 3.5.1. Our results in this section are related to these observations.

3.5.1 Introduction to Force Distributions

The force network of jammed packings is known to be highly heterogeneous. This effect can be characterised by the probability density of contact forces $P(f)$. For jammed particles $P(f)$ typically has a maximum for $f < 1$ [71] and a long tail for $f > 1$, where f is the normalised force $f = f_i/\langle f_i \rangle$ and f_i is the interaction force between particles. Experimentally, the force network of packings has typically been difficult to determine in the bulk. Until recently, the experimental procedure has measured the forces through imprints on carbon paper at the boundaries of a granular assembly [53]. These experiments obtained a $P(f)$ that displayed an exponential rather than a Gaussian decay for large forces. With the advent of techniques that allow inspection of the contact forces inside the bulk of packings, such as confocal microscopy in jammed packings of emulsions [53, 72] and the use of photo-elastic particles [60], a faster than exponential decay has been observed. This faster than exponential decay has also been found for 2D wet foams [54].

There have been many numerical studies on the shape of the $P(f)$ distribution. O'Hern et al. [71] has linked the existence of the maximum of $P(f)$ to packings developing a yield stress, and in [24] it was shown that packings at ϕ_c have different forms of $P(f)$ depending on whether f is normalised by the global average of many packings or by the average of each individual packing, this property is called a lack of self averaging. Using different simulation techniques, Makse et al. [62] and Radjai et al. [73] found that the force distribution displays exponential behaviour at large f.

More recently, van Eerd et al. [74] have shown with the Force Network Ensemble (FNE) approach [75] and using advanced sampling techniques to get good statistics to investigate the tail of $P(f)$ that these tails are faster than exponential and the role of dimension is important.

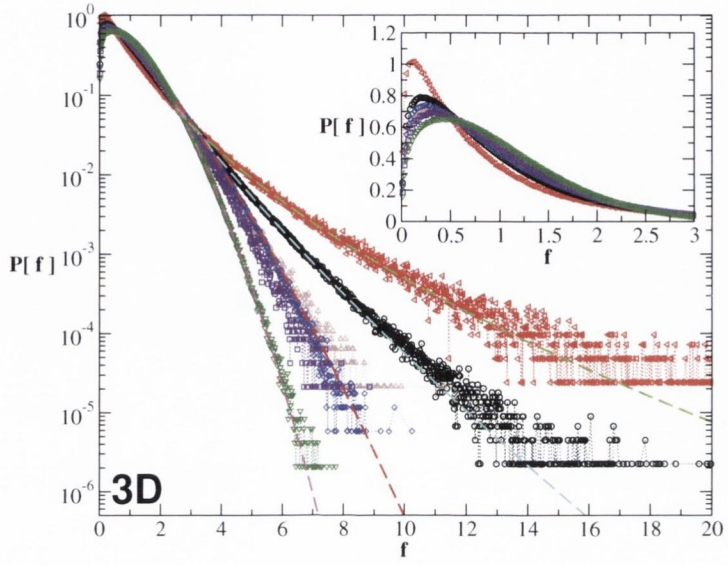

Figure 3.5.2: Force distributions of 3D packing simulations at ϕ_c for a range of polydispersities. The data plotted is labelled as: ($\triangledown$) monodisperse; ($\Diamond$) bidisperse; ($\square$) uniform $\sigma_R = 0.11$; ($\triangle$) Gaussian $\sigma_R = 0.14$; ($\circ$) lognormal $\sigma_R = 0.20$; ($\triangleleft$) lognormal $\sigma_R = 0.28$. The dashed lines are fits of Equation (3.5.1) to the tails of $P(f)$. Inset: Zoom on the peak of the force distributions.

3.5.2 Effect of Polydispersity on the Force Distribution

The effect of polydispersity on $P(f)$ has not been extensively studied; often research has been restricted to monodisperse, bidisperse or a particular sample of polydispersity. Work by Kondic et al. [76] has noted that the polydispersity has an effect on the structure of the force network and there is a note on how polydispersity affects the distribution of forces in a numerical study in 2D [61], which shows only small variation in the behaviour of force distributions for a small range of polydispersity. Work by Voivret et al. [77] has shown that polydispersity does have a pronounced effect on the force distribution but they did not comment on how the tails of $P(f)$ are affected.

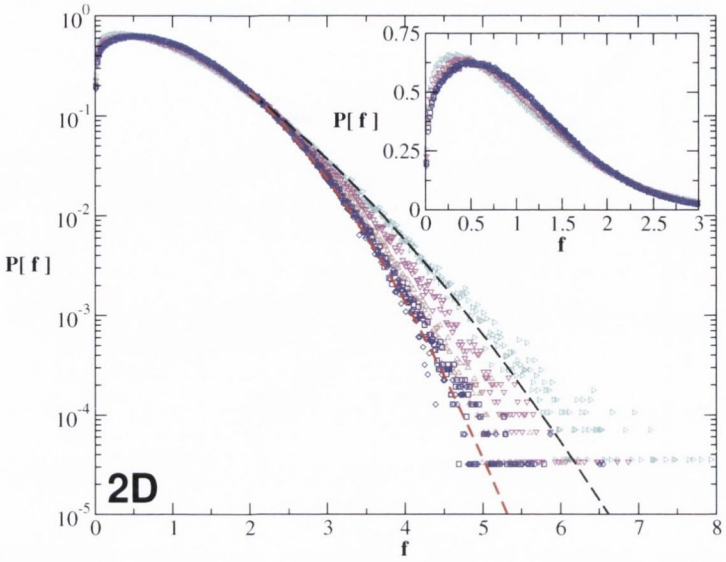

Figure 3.5.3: Force distributions of 2D packing simulations for a range of polydispersities at ϕ_c.The data plotted is labelled as: (◇) bidisperse; (□) uniform $\sigma_R = 0.17$; (△) Gaussian $\sigma_R = 0.24$; (▽) lognormal $\sigma_R = 0.30$; (▷) lognormal $\sigma_R = 0.40$. The dashed lines are fits of Equation (3.5.1) to the tails of $P(f)$. Inset: Zoom on the peak of the force distributions

We find that in both three dimensions and two dimensions, as shown in Figures 3.5.2 and 3.5.3 respectively, the force distribution depends upon the polydispersity of the packings. While the description of the tails of the distribution of disordered packings has been subject to some debate, with the question of whether the tails of the force distribution were described by a Gaussian, exponential or some other fall off, this dependence on polydispersity has not been considered. Using the FNE approach, van Eerd et al. [74] found that in 3D the tails were well described by a faster than exponential fall-off with

$$P(f) \sim \exp(-cf^a), \tag{3.5.1}$$

where $a = 1.7 \pm 0.1$ for 3D monodisperse disordered packings. In 2D bidis-

perse packings, the tails were well described by a Gaussian fall-off, $a = 2.0 \pm 0.1$. As in this work, all forces are normalised such that $\langle f \rangle = 1$. To avoid the difficulties of the lack of self averaging of the force distribution at ϕ_c [24], $P(f)$ is normalised by $\langle f \rangle$ for each packing rather than the ensemble. In our research, we find that $P(f)$ of monodisperse packings in three dimensions and of the bidisperse packings in two dimensions are in good agreement with the results of van Eerd et al. [74]. Equation (3.5.1) is fitted for a selection of size distributions to the tail of $P(f)$ in Figures 3.5.2 and 3.5.3 and demonstrates that the decay of $P(f)$ is strongly dependent on the polydispersity in 3D and slightly dependent in 2D. The value of the fit parameters of Equation (3.5.1) are displayed in Table 3.1.

Polydispersity	D	σ_R	c	a
Monodisperse	3	0.00	0.47 ± 0.01	1.74 ± 0.01
Bidisperse	3	0.17	0.82 ± 0.01	1.21 ± 0.01
Lognormal	3	0.20	1.87 ± 0.04	0.77 ± 0.01
Lognormal	3	0.28	2.90 ± 0.10	0.52 ± 0.01
Bidisperse	2	0.17	0.41 ± 0.02	1.99 ± 0.04
Lognormal	2	0.45	0.52 ± 0.02	1.63 ± 0.03

Table 3.1: Table of the fitting parameters of Equation (3.5.1) used to describe the tails of the polydisperse force distributions.

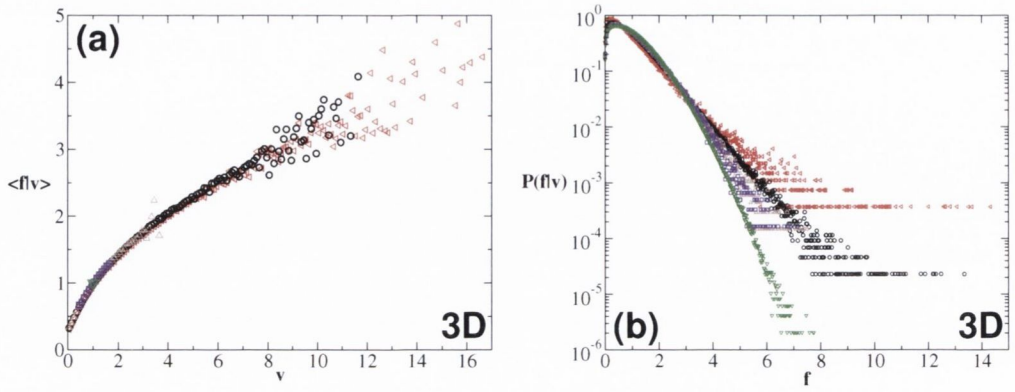

Figure 3.5.4: (a) The average of the distribution of interaction force on a particle given a volume $\langle f|v\rangle$ for 3D packings at ϕ_c. (b) The distribution of forces on a particle given a volume $P(f|v)$ for 3D packings at ϕ_c for $v = 1.00$. The data is labelled as in Figure 3.5.2.

3.5.3 Local Correlations in the Force Network

In the same way that local correlations were found in the contact network, we observe that force correlates with particle size in the force network in three dimensions. for all polydispersities we find that the average f collapses when binned by the normalised volume of a particle v, shown in Figure 3.5.4 (a). Figure 3.5.4 (a) shows that large particles tend to experience larger forces on average. This behaviour may be linked to force chains and the observation that large forces on particles tend to positively correlate with each other [61]. In Figure 3.5.4 (b) the conditional distribution $P(f|v)$ is plotted and unlike the case for contact number, revealed to be not quite independent of polydispersity. It should be noted that the tails of $P(f|v)$ are not as pronounced as for $P(f)$, and these two distribution are not the same.

Since we have shown that f is dependent on the size of the particle, this could suggest that the bulk modulus for the packing is inhomogeneous, since large particles experience larger forces than small particles. To explore this we investigate the total energy of particles as a function of size. The total

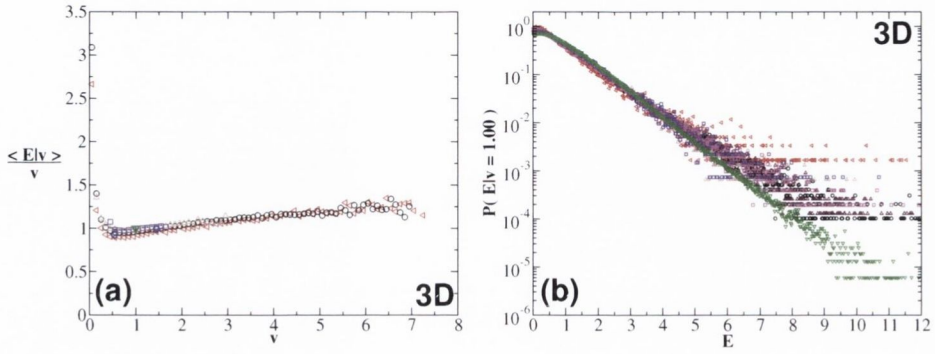

Figure 3.5.5: (a) The ratio of energy of particles of a certain volume v to the volume of the particles for 3D packings at ϕ_c. (b) The distribution of energy on a particles given a certain volume $P(E|v)$ for 3D packings at ϕ_c when $v = 1.00$. The data is labelled the same as Figure 3.5.4.

normalised energy is defined as

$$E_i = \frac{1}{\langle E \rangle} \sum_j \frac{k}{2} \delta_{ij}^2. \tag{3.5.2}$$

For 3D packings, in order for the bulk modulus to be homogeneous, it would require that the ratio of energy to volume, the energy density, to be $\frac{\langle E|v \rangle}{v} = constant$. In Figure 3.5.5(a), we find that despite a slight trend, the ratio is approximately constant, suggesting that inhomogeneities in the bulk modulus are negligible. In Figure 3.5.5(b) the conditional distribution $P(E|v)$ displays an exponential decay, which shows only small variation with σ_R.

3.5.4 Conclusions & Outlook

For the first time we have described how the decay of the tail of $P(f)$ depends upon the polydispersity of the packing in both 2D and 3D. We have shown that large particles tend to have larger forces in 3D. We have shown that the energy density does not vary with particle size, implying that the bulk modulus is roughly homogeneous.

Chapter 4

Nearest Neighbour Correlations

In Chapter 3 we focussed on predicting the contact properties of disordered packings and proposed a mean-field model based on the assumption that the packing is spatially uncorrelated. In this model we assumed that the contact number and size of a particle is uncorrelated to the contact number and size of the surrounding particles.

This assumption is often made by models attempting to explain the properties of disordered media. In recent years successful models like the granocentric model and its progeny make the assumption that the distribution of particle size in packings are homogenous, in other words that the distribution of particle size around a given particle is the same as the global size distribution. Other models to predict the packing density [78] or the distribution of forces [79] also assume that the distribution of contact numbers of particles is not spatially correlated.

In this chapter we investigate whether this assumption holds and to what extent is it a reasonable assumption to make. In order to do this we define the nearest neighbours of a central particle. The particles in contact with this central particle are called nearest neighbours.

4.1 Contact Number Correlations

Firstly, we investigate whether the contact network is spatially correlated by making an analogue to a correlation observed in two dimensional cellular networks called the Aboav-Weaire law. The Aboav-Weaire law states that cells with many neighbours are surrounded by cells with few neighbours and vice versa.

4.1.1 Dry Foams

Dry foams form cellular structures. In perfectly ordered cellular structures in 2D, the number of sides of each cell is 6 and there is no variation in the area distribution of the cells, resulting in the hexagonal honeycomb structure. While we note that monodisperse cellular structures can be disordered, once a wide distribution of cell sizes are allowed, the structure may become much more disordered. It can be proven explicitly that the average coordination number $\langle n \rangle$ of a 2D dry foam must be equal to 6 [80]. While $\langle n \rangle$ of all of the cells must remain constant, the number of sides of an individual cell can vary, giving rise to a distribution $P(n)$. The question is, are the number of sides n of individual cells randomly distributed throughout the foam? This is answered by the Aboav–Weaire law for dry foams.

4.1.2 Aboav–Weaire law

A relationship between the number of sides of cells and the number of sides of neighbouring cells was observed in disorder cellular structures by Aboav [81] in polycrystalline MgO ceramic. Aboav found a correlation between n and the average number of sides of the neighbours of cells with n sides, $m(n)$. He found that cells with many sides are surrounded by cells with few sides and vice versa. The expression that Aboav found to describe the relationship

between n and $m(n)$ was of the form:

$$m(n) = A + \frac{B}{n}, \tag{4.1.1}$$

where A and B are constants. This purely empirical relationship was given a theoretical reinforcement by Weaire [68].

It was noted by Weaire that $m(n)$ obeys a sum rule which is exact in any dimension,

$$\sum_n m(n) n P(n) = \sum_n n^2 P(n), \tag{4.1.2}$$

where n denotes the number of sides of a cell and $P(n)$ is the distribution of $n$sided cells.

This sum rule (Equation (4.1.2)) can be shown by a counting argument. In detail, the cell A (see Figure 4.1.1) has n_A sides each counted n_A times on the right hand side of Equation (4.1.2). The average number of sides of the

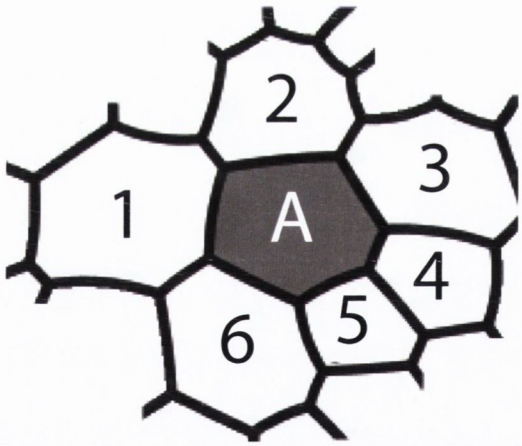

Figure 4.1.1: Aboav-Weaire correlations in cellular structures. The cells have been labelled in order to aid understanding of the Weaire sum rule.

neighbours of cell A is m_A, which is given by

$$m_A = \frac{1}{n_A} \sum_{i}^{n_A} n_i. \tag{4.1.3}$$

By averaging m for all cells with n neighbours, $m(n)$ is found. Considering the left hand side of Equation (4.1.2) then gives,

$$\sum_n m(n) n P(n) = \sum_n \left(\frac{1}{n} \sum_i^n n_i \right) n P(n) = \sum_n \left(\sum_i^n n_i \right) P(n). \tag{4.1.4}$$

Considering the right hand side of Equation (4.1.4), the first sum cycles through all the cells in the cellular structure. The sum in the bracketed expression then adds up the contribution n of all the neighbours of each cell counted in the first sum. Since only the contribution of the neighbouring cells are counted then each n appears n times because that cell has n neighbours. Then Equation (4.1.2) is a weighted sum of the contact numbers and therefore

$$\sum_n \left(\sum_i^n n_i \right) P(n) = \sum_n n^2 P(n), \tag{4.1.5}$$

which is identical to the right hand side of Equation (4.1.2), therefore the Weaire sum rule holds.

The contribution of Weaire was to show that Equation (4.1.1) must be of a form to satisfy Equation (4.1.2). The Aboav–Weaire law is then the simplest expression that both satisfies Equation (4.1.2) and describes the correlations between m and n. The resulting expression is,

$$m = 6 - a + \frac{6a + \mu_2}{n}, \tag{4.1.6}$$

where a is an empirical parameter whose value for a typical dry 2D foam is 1.2 [2] and μ_2 is the variance of the cell sides which is defined as $\mu_2 = \langle n \rangle^2 - \langle n^2 \rangle$.

The exact physical significance of the a parameter is unknown.

This relation, known as the Aboav–Weaire law (but is in fact a conjecture) is described as semi-empirical as the sum rule proposed by Weaire only gives consistency to Aboav's relation. It is reported as being found in all naturally disordered cellular structures [82]. However, some artificial structures such as the random Voronoï froth show small deviations from the Aboav–Weaire law [83]. There has been no successful proof of the Aboav-Weaire law and it has only be shown to be exact for some special cases [84].

In the absence of spatial correlations, m is a constant and is given by,

$$m(n) = \langle n \rangle + \frac{\mu_2}{\langle n \rangle}. \tag{4.1.7}$$

This uncorrelated arrangement in cellular structures is called a topological gas. The existence of such an uncorrelated structure is uncertain [85].

Most commonly this correlation has been investigated in two dimensions, though the Equation (4.1.6) has been altered to apply to polyhedra tesselations in 3D [86, 87],

$$m(f) = \langle f \rangle - a + \frac{a\langle f \rangle + \mu_2^f}{f}, \tag{4.1.8}$$

where f is the number of faces of the polyhedron, $m(f)$ is the average number of faces of neighbouring polyhedra, μ_2^f is the variance of the distribution of f and a is the Aboav–Weaire parameter in 3D. Equation (4.1.8) has found to be applicable to various type of cellular structure in 3D [86, 87], demonstrating that there are spatial correlations in 3D cellular networks as well.

4.1.3 Weaire Sum Rule in Disc Packings

Initially restricting ourselves to two dimensions, we return to packings and make an analogue with cellular structures for packings. We investigate whether the contact network is spatially correlated by defining $Z_{nn}(z)$ to be the average contact number of particles that are in contact with a particles that has z contacts. $Z_{nn}(z)$ is analogous to the quantity $m(n)$ in the Aboav–Weaire law.

The sum rule argument, which was originally developed for cellular structures, holds equally well for a contact network of disordered soft disc packings. The main difference, as shown before, is that in two-dimensional cellular structures with three-fold vertices, $\langle n \rangle = 6$, while frictionless packings in two dimensions have $\langle z \rangle = z_c = 4$ at ϕ_c [64]. The sum rule for the contact network in packings is then

$$\sum_z Z_{nn}(z) z P(z) = \sum_z z^2 P(z). \tag{4.1.9}$$

Z_{nn} is then a function of z that must satisfy Equation (4.1.9). For uncorrelated packings $Z_{nn}(z)$ is a constant ($\overline{Z}_{nn}$) which is independent of z and from Equation (4.1.9) is equal to

$$\overline{Z}_{nn} = \langle z \rangle + \frac{\sigma_z^2}{\langle z \rangle}. \tag{4.1.10}$$

This is the disc packing uncorrelated arrangement analogous to Equation (4.1.7).

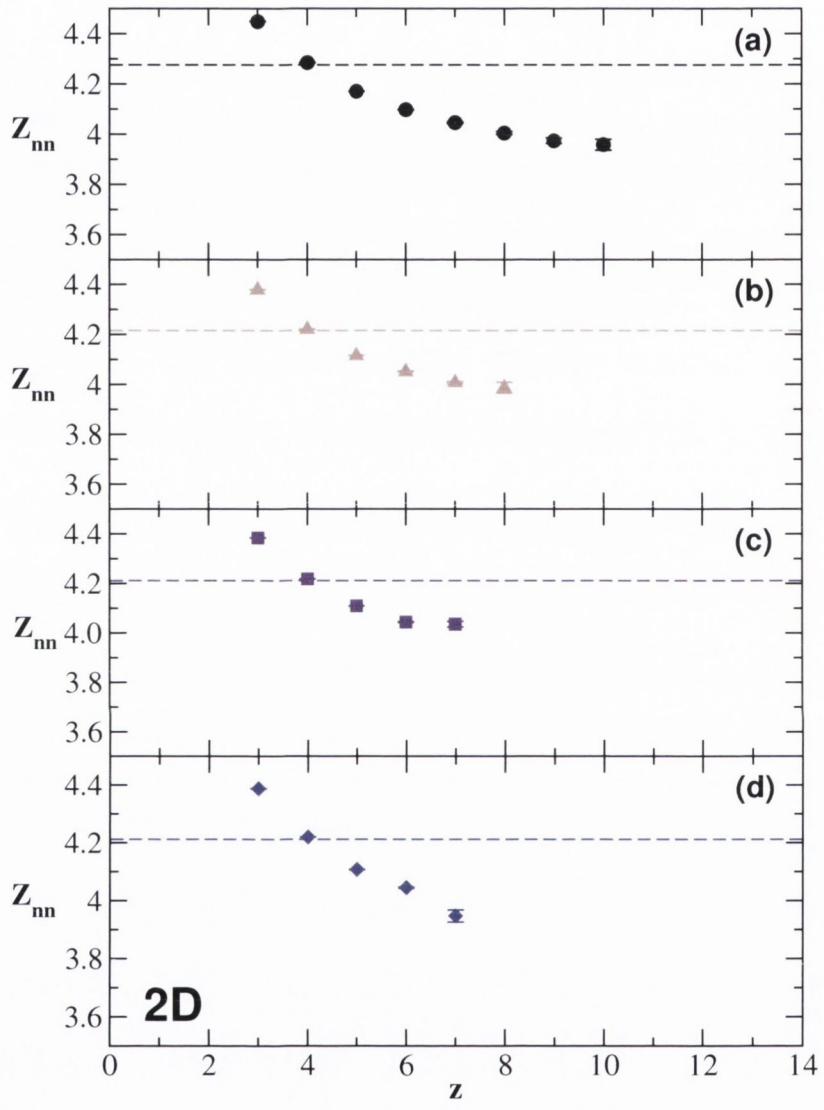

Figure 4.1.2: Contact number correlations for discs in contact at ϕ_c in 2D. The error bars are standard deviations from the mean. The dashed line is the prediction of an uncorrelated packing from Equation (4.1.10). The data plotted in each panel is: (a) lognormal $\sigma_R = 0.35$; (b) Gaussian $\sigma_R = 0.24$; (c) uniform $\sigma_R = 0.17$; (d) bidisperse.

4.1.4 Correlations in the Contact Network of Disc Packings

Plotted in Figure 4.1.2 is $Z_{nn}(z)$ for a variety of size distributions of discs in 2D at the random close packing density. For wide size distributions, independent of the type of size distribution, it is observed in Figure 4.1.2(a)-(d) that particles with less contacts than average are surrounded by particles with many contacts. Also, particles with more contacts than average are surrounded by particles with fewer contacts. The uncorrelated prediction $\overline{Z}_{nn}$ fails to capture the trend of $Z_{nn}(z)$ and therefore there are nearest neighbour anti-correlations in the contact network similar to cellular structures.

4.1.5 Aboav–Weaire in Disc Packings

Despite having shown in Chapter 3 the validity of making a mean field assumption for the model to predict $P(z)$ by implicitly assuming that disordered packings are uncorrelated, Figure 4.1.4 clearly shows that this is not the case. Correlations similar to the Aboav–Weaire law for cellular structures are found in two dimensional packing data.

Though there are correlations, it is not clear if they are of Aboav–Weaire form. $Z_{nn}(z)$ is an empirical function that must also satisfy Equation (4.1.9). A solution to Equation (4.1.9) can be found by a series expansion in terms of the moments of $P(z)$:

$$(Z_{nn} - \langle z \rangle)z - \sigma_Z^2 = -\sum_{i=1} c_i \left(z^i - \langle z^i \rangle \right), \tag{4.1.11}$$

where the c_is are arbitrary constants. If $c_i = 0$ for $i > 1$, one recovers the packing version of the Aboav–Weaire relationship,

$$Z_{nn} = \langle z \rangle - a + \frac{a\langle z \rangle + \sigma_Z^2}{z}. \tag{4.1.12}$$

We now take the data shown in Figure 4.1.2 and plot this data again in Figure 4.1.3 with axes chosen so that if the data was in agreement with Equation (4.1.12), there would be a straight line with negative slope. Figure 4.1.3 shows that contact anti-correlations in 2D disc packings are well described by Equation (4.1.12). In the inset of Figure 4.1.3 the a parameter is plotted showing a sharp decrease when the size distribution is sufficiently narrow as to allow crystalline patches to occur. This is compared to the a parameter for uncorrelated packings, in this case a typically takes a negative value.

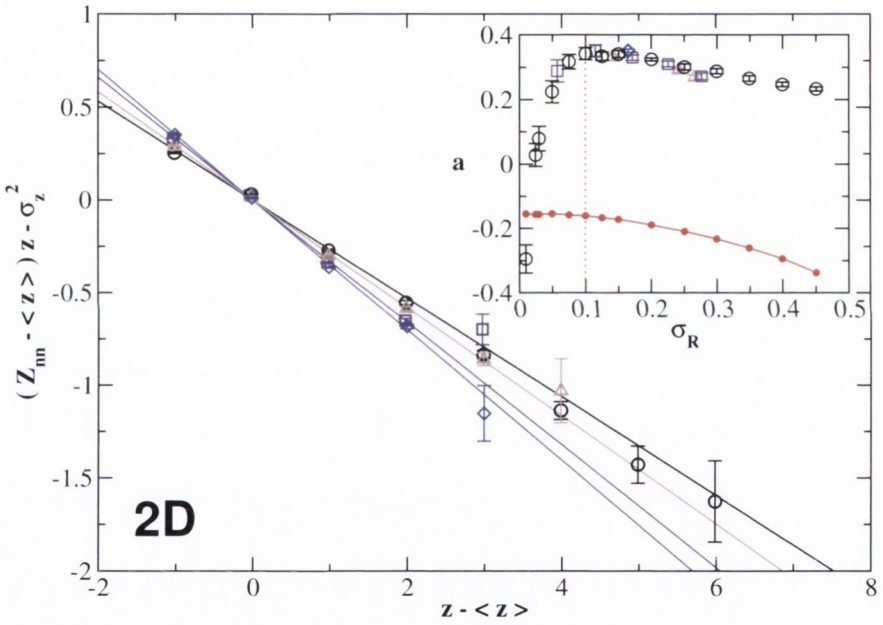

Figure 4.1.3: Contact number correlations for discs in contact at ϕ_c, for the same size distributions as in Figure 4.1.2(a)-(d). The error bars are standard deviations from the mean. The solid lines are fits to Equation (4.1.12). The inset shows the fit parameter a as a function σ_R. The dashed red line marks the σ_R at which crystallisation can occur. Inset: The data is labelled the same as in Figure 2.3.2. The solid red line is the value of the uncorrelated a for that σ_R.

This Aboav–Weaire anti-correlation can be interpreted as a partial screening of topological charge $z - \langle z \rangle$ by its contacting neighbours whose combined charge is $z(Z_{nn} - \langle z \rangle)$. The parameter a can then be used as a measure of that screening of topological charge. For packings beyond the point at which crystallisation may occur, there is a steady decline in the value of a. This is reminiscent of the prediction for the a parameter in cellular structures to decline as the variance increases [88]. Recall that in Figure 3.4.3 the variance σ_Z^2 had a linear dependence on the σ_R^2.

4.1.6 Correlations in the Contact Network of Sphere Packings

Moving to three dimensions the same argument applies as in the 2D case. The principle change is that $\langle z \rangle = 6$ in 3D. Figure 4.1.4 shows $Z_{nn}(z)$ for various size distributions in 3D. All distributions exhibit clear anti-correlations, particles with few contacts are surrounded by particles with many contacts and vice versa. However, deviations from the uncorrelated prediction $\overline{Z}_{nn}$ are usually less than 10%, suggesting a cause of the success of the mean field granocentric approach, despite the correlations in the contact network.

4.1.7 Aboav–Weaire Correlations in Sphere Packings

Plotting $Z_{nn}(z)$ in the manner of Figure 4.1.4 clearly shows that there are spatial correlations in the contact network, however it is difficult to resolve whether Equation (4.1.12) perfectly captures the correlations. In order to get a clear idea of how well the data is described by the classic Aboav–Weaire correlation, we re-plot the data in Figure 4.1.5 as $(Z_{nn} - \langle z \rangle)z - \sigma_Z^2$ versus $z - \langle z \rangle$. Should the data have a strictly linear behaviour with negative slope then it would be described by the original Aboav–Weaire correlation. Instead a non-linear behaviour is observed for all distributions with deviations from the linear trend observed at high and low $z - \langle z \rangle$.

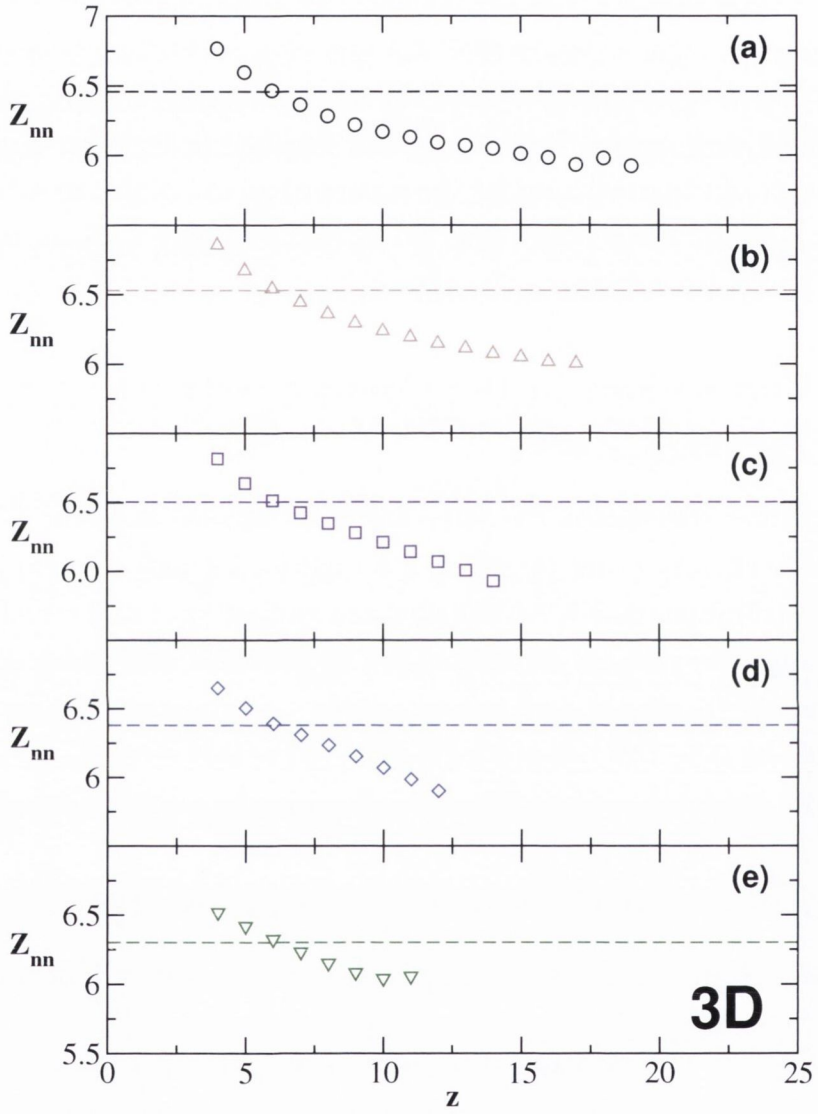

Figure 4.1.4: Contact number correlations for spheres in contact at ϕ_c. The dashed line is the prediction of an uncorrelated packing from Equation (4.1.10). The data plotted in each panel is: (a) lognormal $\sigma_R = 0.20$; (b) Gaussian $\sigma_R = 0.22$; (c) uniform $\sigma_R = 0.24$; (d) bidisperse; (e) monodisperse.

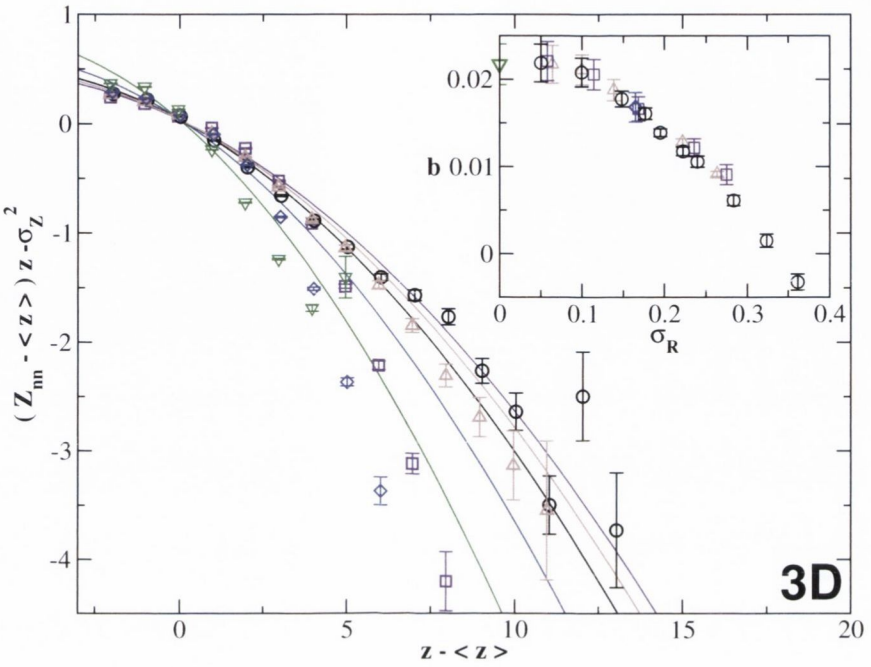

Figure 4.1.5: Contact number correlations for spheres in contact at ϕ_c, for the same size distributions as in Figure 4.1.4. The error bars are standard deviations from the mean. The solid lines are fits to Equation (4.1.13). The inset shows the fit parameter b as a function σ_R. The data in the inset is labelled the same as in Figure 2.3.2.

In order to account for these deviations from the linear trend of the classic Aboav–Weaire correlation, we revisit Equation (4.1.11). In two dimensions for ϕ_c it was found that to describe the data it was sufficient to only make $c_1 \neq 0$; because of the deviations from linearity observed in three dimensions, we investigate higher powers of i. By only making the second term non-zero ($c_2 \neq 0$), the deviations in the data can be described by a modified Aboav–Weaire correlation

$$Z_{nn} = \langle z \rangle - bz + \frac{b\langle z \rangle^2 + \sigma_Z^2(1+b)}{z}, \tag{4.1.13}$$

where $b = c_2$.

Equation (4.1.13) captures the trend of the data for all size distributions in Figure 4.1.5, however only the Gaussian data is fully described by this equation. In the inset of Figure 4.1.5 the fit parameter b is plotted for increasing values of σ_R. b does not depend on the shape of the size distribution but only on the width σ_R. Note that all size distributions regardless of shape or width exhibit these anti-correlations in the contact network. The physical meaning of b like the equivalent parameter a in the cellular Aboav-Weaire law is not clear [2]. Of course various combinations of powers of i can be introduced from Equation (4.1.11) to better describe the correlations but the simplest expression that describes the trend in Z_{nn} is to keep only the second term in the expansion in Equation (4.1.11) non-zero.

The existence of these contact number correlations in the contact network are not obvious, as cellular structures and packings are governed by different global and local constraints. Although polydisperse packings can be tessellated into a cellular structure [50, 86], not all faces of a cell correspond to contacts, therefore the existence of correlations in packings does not follow naturally from similar correlations in disordered cellular structures.

4.2 Size-Size Correlations

We have shown in Section 3.2 that a relationship between the size of a particle and the contact number of a particle exists, where small particles typically have a lower coordination number than larger particles. As well, we have shown in the previous sections that there are spatial correlations in the contact network of the disordered packings, where particles with a low coordination number tend to be in contact with particles that have a high coordination number. We now investigate whether the size of nearest neighbour particles are correlated.

There has been limited study of the relationship between size of particles in contact in packings. The only examples of previous investigations of this phenomenon in cellular structures is the work of Sire and Seul [89] and Seul et al. [90]. These works examined the relative size of neighbouring cells in 2D cellular structures and found that cells sizes were anti-correlated to the size of its neighbour.

4.2.1 Size-Size Correlations in 3D

We begin by looking at size correlations in 3D sphere packings. In order to explore potential size correlations, $A_{nn}(a)$ is defined as the average normalised surface area of all particles in contact with a particle with surface area a. In Figure 4.2.1(a), A_{nn} is plotted versus a for four different size distributions, and we find that there are spatial correlations in the size of particles in disordered packings. On average larger particles are surrounded by smaller particles and vice versa. The trend in the data differs from that which describes a packing in which the size of particles in contact is uncorrelated, defined as $\overline{A}_{nn}$ in Equation (4.2.3).

4.2.2 Relationship of Size-Size Correlations in 3D

Restricting our attention initially to 3D, the same counting argument that is used to formulate Equation (4.1.9) can be applied to particle size in a similar fashion. Analogous to Equation (4.1.9), A_{nn} must satisfy the following relation:

$$\int_0^\infty A_{nn}(a)\langle z|a\rangle P(a)da = \int_0^\infty a\langle z|a\rangle P(a)da. \tag{4.2.1}$$

In the scenario where there are no correlations in the size distribution of neighbouring particles, then $A_{nn}(a)$ becomes a constant ($\equiv \overline{A}_{nn}$) and Equation (4.2.1) becomes

$$\overline{A}_{nn}\int_0^\infty \langle z|a\rangle P(a)da = \int_0^\infty a\langle z|a\rangle P(a)da, \tag{4.2.2}$$

and then integrating on the left hand side and rearranging gives,

$$\overline{A}_{nn} = \int_0^\infty a\left(\frac{\langle z|a\rangle}{\langle z\rangle}P(a)\right)da. \tag{4.2.3}$$

In Figure 3.2.2 it was shown that $\langle z|a\rangle$ was well described by Equation (3.2.3). A simple prediction of the average size of neighbours in an uncorrelated packing can be found by substituting Equation (3.2.3) into the previous expression, and then simplifying to

$$\overline{A}_{nn} = 1 + \frac{\gamma}{\langle z\rangle}\sigma_A^2, \tag{4.2.4}$$

where at ϕ_c, $\langle z\rangle = z_c$ is a constant, as is the fit parameter of Equation (3.2.3), $\gamma = 3.03$. This relation is plotted in Figure 4.2.2.

Alternatively, the sum rule analogue for particle size can be written as the sum

$$\sum_z \langle A_{nn}|z\rangle z P(z) = \sum_z z\langle a|z\rangle P(z), \tag{4.2.5}$$

where $\langle A_{nn}|z\rangle$ is the average area of a particle with z contacts. In this case

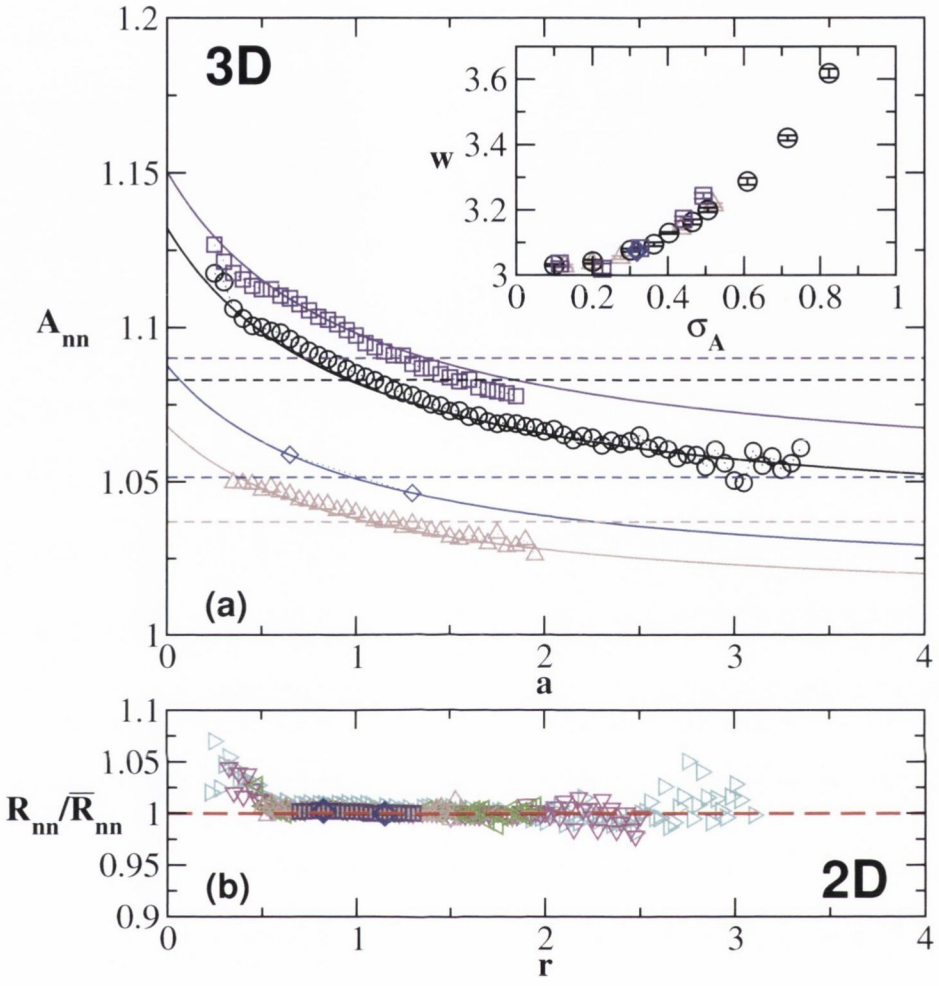

Figure 4.2.1: (a) Correlations between size of spheres in contact. All symbols represent the same size distributions as in Figure 4.1.5 except: (△) Gaussian $\sigma_R = 0.14$. The solid lines are fits to the data using Equation (4.2.8) with the dashed lines being the uncorrelated prediction calculated from Equation (4.2.6). The inset shows the fit parameter w as a function of σ_A. The data in the inset is labelled the same as in Figure 2.3.2. (b) Correlations between size of discs in contact in two dimensions rescaled by the predicted uncorrelated radius $\overline{R}_{nn}$. Five different size distributions are plotted: (◊) bidisperse, radius ratio 1:1.4; (□) uniform $\sigma_R = 0.17$; (△) Gaussian $\sigma_R = 0.14$; (◁) lognormal $\sigma_R = 0.20$; (▽) lognormal $\sigma_R = 0.30$; (▷) lognormal $\sigma_R = 0.40$.

when A_{nn} is uncorrelated, it can be calculated from

$$\overline{A}_{nn} = \frac{1}{\langle z \rangle} \sum_z z \langle a|z \rangle P(z), \tag{4.2.6}$$

which is the data plotted in Figure 4.2.2.

In order to describe the trend of A_{nn} seen in Figure 4.2.1 (a), we formulate a series expansion in terms of the moments of $P(a)$ that satisfies Equation (4.2.1),

$$A_{nn}(a) = \frac{\int_0^\infty a \langle z|a \rangle P(a) da + \sum_i w_i (a^i - \langle a^i \rangle)}{\langle z|a \rangle}, \tag{4.2.7}$$

where w_i are arbitrary constants.

Substituting this expression into Equation (4.2.7) and taking only the first term in the expansion ($i = 1$) gives,

$$A_{nn}(a) = \frac{\langle z \rangle + \gamma \sigma_A^2 + w(a - 1)}{\langle z \rangle + \gamma (a - 1)}, \tag{4.2.8}$$

where $w = w_1$. This one parameter fit to data, with γ constrained to fit $\langle z|a \rangle$, is shown in Figure 4.2.1(a). Equation (4.2.8) is found to be a good description of the correlations between the size of particles in packing.

Plotted in the inset of Figure 4.2.1(a) is the behaviour of w with increasing width. Similar to the parameter a used as a measure of disorder of the contact network, w can be used to quantify the strength of anti-correlations in the particle size network. Packings with larger w have stronger separation of particle sizes. Therefore the more polydisperse a packing, the less the distribution of sizes of nearest neighbours resembles the global size distribution.

4.2.3 Relationship of Size-Size Correlations in 2D

We reported in [64] an equivalent sum rule to Equation (4.2.1) for disc radius in two dimensions:

$$\int_0^\infty R_{nn}(r)\langle z|r\rangle P(r)dr = \int_0^\infty r\langle z|r\rangle P(r)dr, \tag{4.2.9}$$

where $R_{nn}(r)$ is the average normalised radius in contact with a particle of radius r, which is plotted in Figure 4.2.1(b). In contrast to the results for three-dimensional sphere packings, the relationship between the radius of a disc and the average radius of its contacts is well described by the uncorrelated prediction, given as

$$\overline{R}_{nn} = \int_0^\infty r\left(\frac{\langle z|r\rangle}{\langle z\rangle}P(r)\right)dr, \tag{4.2.10}$$

for all polydispersities. There are some deviations from the uncorrelated prediction at low r. These deviations can be attributed to the presence of small particles with a low number of contacts that can only remain in the connected network when in contact with much larger spheres.

Using the same arguments as in three dimensions, the relationship between $\overline{R}_{nn}$ and the width of the size distribution can be found to be

$$\overline{R}_{nn} = 1 + \frac{\gamma_{2D}}{\langle z\rangle}\sigma_R^2, \tag{4.2.11}$$

where γ_{2D} and $\langle z\rangle$ are constant at ϕ_c.

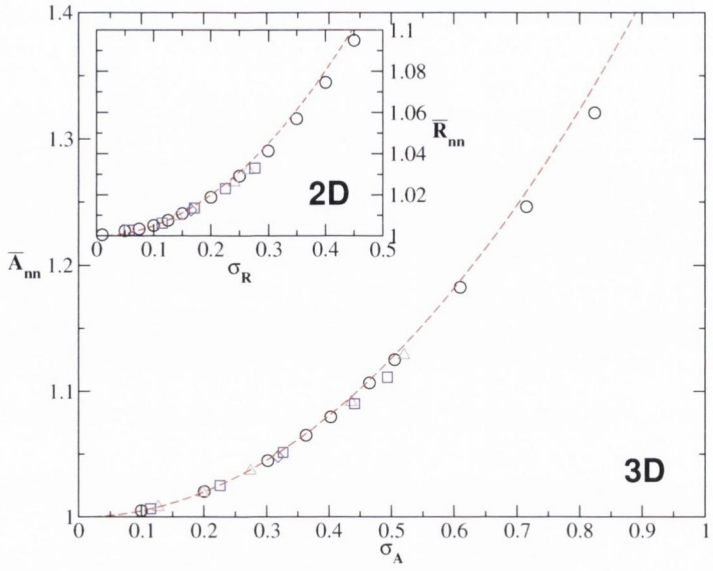

Figure 4.2.2: The uncorrelated prediction $\overline{A}_{nn}$ for a range of different size distributions in three dimensions. The data plotted is calculated from Equation (4.2.6). The dashed line is the uncorrelated prediction of $\overline{A}_{nn}$ calculated from Equation (4.2.4). Inset: The uncorrelated prediction $\overline{R}_{nn}$ for a range of different size distribution in two dimensions. The data plotted is calculated from Equation (4.2.10). The dashed line is the uncorrelated prediction of $\overline{R}_{nn}$ calculated from Equation (4.2.11). The data is labelled the same as in Figure 2.3.2.

4.2.4 Uncorrelated Prediction

As can be seen from Figure 4.2.2, the relationship between the uncorrelated prediction of the average size of neighbouring particles is the same in 2D and 3D but for a change in variable. Figure 4.2.2 shows that as σ_A increases so do the values of $\overline{A}_{nn}$. $\overline{R}_{nn}$, which is plotted in the inset of Figure 4.2.2, increases with increasing σ_R. Both $\overline{A}_{nn}$ and $\overline{R}_{nn}$ are well described by Equation (4.2.4) and Equation (4.2.11), respectively. $\overline{A}_{nn}$ and $\overline{R}_{nn}$ are greater than 1 because particles with more contacts tend to be larger and therefore large particles

tend to be included in the calculation of A_{nn} and R_{nn} more often than smaller particles, which on average have less contacts. Equations (4.2.4) and (4.2.11) show that as packings become more polydisperse this contribution of larger particles becomes more pronounced.

The uncorrelated predictions in Equations (4.2.4) and (4.2.11) can be recast as the average of the size distribution of neighbouring particles. This allows from the bracketed expressions in Equation (4.2.4) and Equation (4.2.11), an expression for the size distribution of neighbouring particles to be formed as,

$$P(A_{nn}) = \left(\frac{\langle z|a \rangle}{\langle z \rangle} P(a) \right) \Bigg|_{a=A_{nn}} \tag{4.2.12}$$

and

$$P(R_{nn}) = \left(\frac{\langle z|r \rangle}{\langle z \rangle} P(r) \right) \Bigg|_{r=R_{nn}}, \tag{4.2.13}$$

respectively. Due to the behaviour of $\langle z|a \rangle$ and $\langle z|r \rangle$ from Equation (3.2.3) and Equation (3.2.6), for all polydisperse packings the size distribution of nearest neighbours is not the same as the global size distribution of the packings. This has consequences for mean field models such as the granocentric model that assume the size distribution of contacts is the same as the global size distribution $P(R)$ [44]. This assumption becomes progressively worse with increasing polydispersity.

4.3 Conclusions & Outlook

We have shown in this chapter that, despite their name, random disordered packings contain robust correlations between neighbouring particles. For the first time we have shown that random packings of discs and spheres are structured in such a way that Aboav–Weaire type anti-correlations exist in the contact network. We note that at ϕ_c, the anti-correlations in contact number are described by two different terms of Equation (4.1.11), we do not have an explanation for why these trends are subtly different in 2D and 3D. We note that while we do not have a physical explanation of the origin of these Aboav–Weaire correlations in packings, the analogy with cellular structures may continue to extend to explaining these correlations similarly in terms of maximum entropy (for a description of maximum entropy see Weaire and Rivier [82]). The description of these correlations in packings could potentially be used to characterise the disorder of packings through the measure of the parameters a and b and to what extent topological charge is screened.

Also presented in this chapter is the interesting result of anti-correlation of particle size with neighbouring particle size in 3D but curiously this is not found in 2D. The significance of this result is that the size distribution of contacts is not homogeneous in 3D. A more damaging result for models that rely on the assumption that the size distribution of nearest neighbours is the same as the global size distribution, such as the granocentric model, is the increase of the uncorrelated predicted average for wider size distributions in both 2D and 3D. This result states even if the distribution of particles sizes is homogeneous, the mean of the resulting distribution of sizes of neighbouring particles will still increase with polydispersity, due to the trend of larger particles having more contacts.

We can only attribute the success of the granocentric model to the fact that the nearest neighbour correlations are typically weak.

Perhaps the discovery of these correlations can point the way to a more comprehensive method of describing the structure of disordered packings.

Chapter 5

Effect of Packing Fraction on the Structure of Disordered Packings

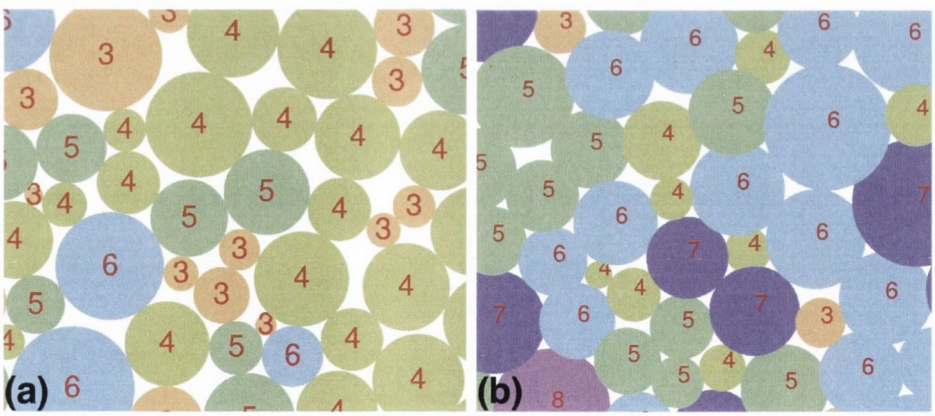

Figure 5.0.1: Examples of discs in contact in a packing with Gaussian size distribution of width $\sigma_R = 0.28$ at (a) $\phi = \phi_c$ and (b) $\phi = 1.00$.

Previously we have described various local and global contact properties of disordered packings at ϕ_c. How do these contact network correlations change for polydisperse packings as we move away from the isostatic point?

There have been many studies of the properties of jammed matter with changing density. Computationally, Bolton and Weaire [3], were the first to show that properties of wet foams like the shear modulus and the average contact number scale with the distance from the rigidity loss transition. More recently, the landmark study by O'Hern et al. [24] described the scaling of quantities such as the elastic moduli with distance from the jamming point. Other work based on foams has shown that various properties scale with the distance from ϕ_c. Experimentally, Katgert and van Hecke [54] have confirmed what has previously been shown computationally, that the average contact number $\langle z \rangle$ scales with distance from jamming, as also observed in experiments of frictional discs [91]. Recently Zhao et al. [92] have shown that there is a regime change at very high packing fraction $\phi = 1.18$ for simulations of bidisperse particles in 3D, above which packings are referred to as deeply jammed. At this point the scalings reported by O'Hern et al. [24] break down and different scalings are found. Note, in soft particle simulations the overlap between particles is counted twice in the calculation of ϕ [18]. It is difficult to compare ϕ calculated in soft particle simulations to ϕ measured in experiments due to the deformation of particles at high ϕ in real foams.

Also of interest is the analogy with dry foams, which we have made in Chapter 4. Many of the correlations seen at ϕ_c are also observed for cellular structures like dry foams. Recent work on the granocentric model has made predictions for cellular structures [59].

We study packings which range from ϕ_c up to $\phi = 1.00$ for a variety of polydispersities in 3D, which is less than the value found for where a regime change occurs and deep jamming occurs [92]. In two dimensions, we study packings up to $\phi = 1.20$, where the average contact number reaches $\langle z \rangle = 6$. Examples of 2D packings at different ϕ are shown in Figure 5.0.1.

5.1 Contact Number Distributions

First we look at the contact number distribution beyond the jamming point. Figure 5.1.1 shows the distribution of the relative contact number, $P(z-\langle z\rangle)$, for different packing fractions and different polydispersities. The shape of the $P(z-\langle z\rangle)$ distributions are independent of the packing fraction as evidenced by the collapse of $P(z-\langle z\rangle)$ onto a master curve which is dependent upon the polydispersity. The $P(z-\langle z\rangle)$ collapse is surprising and means that the shape of $P(z)$ around its mean depends on $P(R)$ but not on ϕ.

As shown in the inset of Figure 5.1.1, $\langle z\rangle$ increases as the square root of the distance of ϕ from the isostatic point, which is consistent with previous results in both experiment [54, 91] and simulations [24, 42]. This increase in the average contact number $\langle z\rangle$ is described by [24]

$$\langle z\rangle = z_c + Z_0\sqrt{\phi-\phi_c}, \tag{5.1.1}$$

where Z_0 is the fit parameter. This relationship is valid in both 2D and 3D. This equation is fit to the simulation data and for a select group of size distribution the fits are plotted in the top inset of Figure 5.1.1 for 2D and the top inset of Figure 5.1.2 for 3D. The value Z_0 for various polydispersities can be found in Table 5.1.

There is good agreement between Z_0 found by fitting Equation (5.1.1) to the polydisperse data presented here and the bidisperse data found in [24], where $Z_0 = 3.6 \pm 0.5$ in 2D and $Z_0 = 8.4 \pm 0.5$ in 3D. The one notable discrepancy between the results is that for monodisperse which is found to be larger in this work than in [24] (where $Z_0 = 7.7 \pm 0.5$), this may be attributed to the wider range of densities explored in this work. The result is that the average contact number in dense monodisperse packings is larger in this work than predicted by O'Hern et al. [24].

For 3D data, the shape of the distribution is independent of the packing fraction when the relative contact number is rescaled by the standard

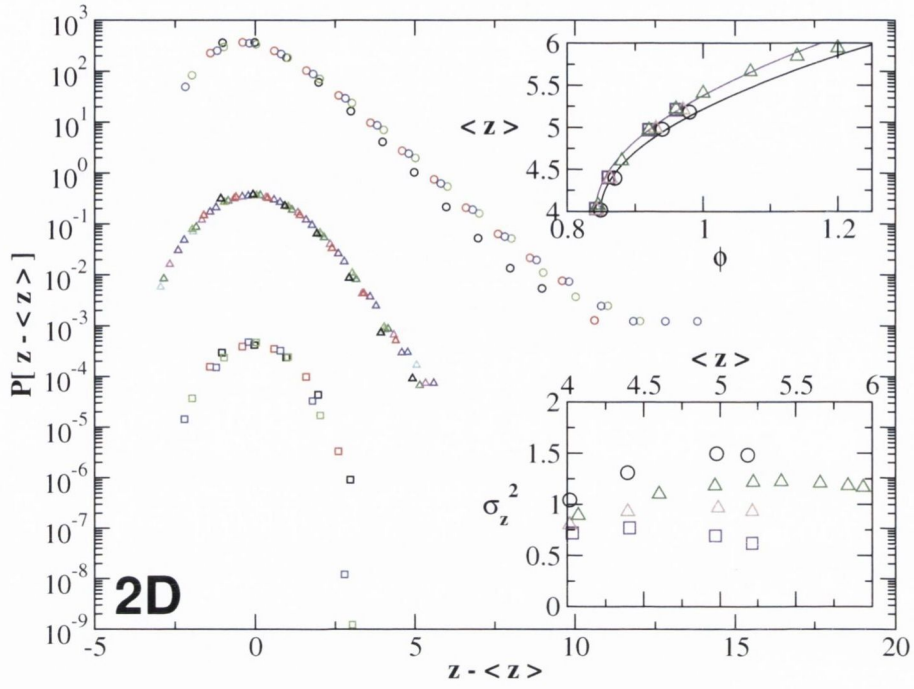

Figure 5.1.1: Contact number distributions for increasing packing fraction ϕ in 2D are plotted for a lognormal size distribution of width $\sigma_R = 0.35$ (top, represented by (○)), a Gaussian distribution of width $\sigma_R = 0.28$ using the bubble model packing algorithm (middle, (△)) and a uniform size distribution of width $\sigma_R = 0.17$ (bottom, (□)). The distributions are shifted on the y-axis so that different polydispersities can be compared. The packing fractions plotted have an $\langle z \rangle$ represented in the top and bottom insets. The $P(z - \langle z \rangle)$ are colour coded with ϕ_c coloured in black; and then in increasing $\langle z \rangle$ (and hence ϕ) coloured as red; green; blue; purple; pink; dark green; cyan. Top Inset: Contact number average $\langle z \rangle$ versus ϕ. The data plotted are: (□) uniform $\sigma_R = 0.17$; (△) Gaussian $\sigma_R = 0.24$; (△) Gaussian $\sigma_R = 0.28$ (using bubble model algorithm); (○) lognormal $\sigma_R = 0.35$. The solid lines are Equation (5.1.1) fitted to the uniform data (in purple) and to the lognormal data (in black). Bottom Inset: Contact number variance σ_z^2 versus $\langle z \rangle$. The data are labelled the same as in top inset.

Polydispersity	D	σ_R	Z_0
Lognormal	2	0.35	3.03 ± 0.1
Gaussian	2	0.28	3.29 ± 0.1
Gaussian	2	0.24	3.33 ± 0.1
Uniform	2	0.17	3.45 ± 0.1
Lognormal	3	0.20	8.3 ± 0.2
Gaussian	3	0.19	7.7 ± 0.3
Lognormal	3	0.10	8.1 ± 0.3
Monodisperse	3	0.00	9.0 ± 0.1

Table 5.1: Prefactor Z_0 of Equation (5.1.1) for different polydispersity in 2D and 3D packings.

deviation of the contact number distribution σ_Z, as evidenced by the collapse of $P\left((z - \langle z \rangle)/\sigma_z\right)$ onto a master curve in Figure 5.1.2. Again it is the polydispersity that sets $P(z)$ in a non-trivial manner.

The same rescaling with σ_Z in 2D does not work generically; in particular the lognormal data is clearly not described by such a collapse. The corresponding variance σ_Z^2 in 2D, plotted in the bottom inset of Figure 5.1.1, varies slightly. This is partly due to the fact that the minimum contact number is restricted to 3 while $\langle z \rangle$ plateau at 6. Packings with wide size distributions have wider contact number distributions as the density is increased, due to more particles forming contacts, as seen in Chapter 3, Equation (3.2.6), leading to a larger contact number variance. For narrower distributions σ_Z^2 is close to unity and relatively constant with increasing density. The choice of rescaling in 2D does not alter dramatically the collapse of $P(z)$ but for wider distributions σ_Z^2 is larger and rescaling by σ_Z is inappropriate.

The relationship in 3D for σ_Z^2 is more complex for increasing density. The polydisperse packings have σ_Z^2 increasing with ϕ and the rate of increase appears to be linked to σ_R. In the monodisperse case σ_Z^2 slowly decreases, suggesting that the monodisperse packing becomes more ordered as ϕ increases. Common to both trends is that the variance reaches a constant

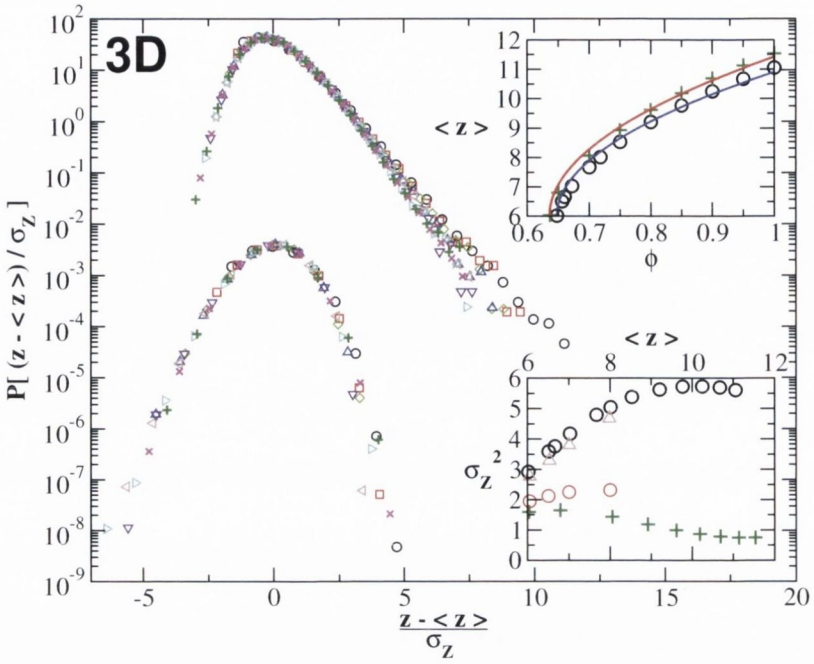

Figure 5.1.2: Contact number distributions for increasing packing fraction ϕ are plotted for a lognormal size distribution with $\sigma_R = 0.20$ (above) and a monodisperse size distribution (below). The distributions are shifted on the y-axis so that different polydispersities can be compared. The packing fractions plotted are $\phi =$: (○) ϕ_c; (□) 0.65; (◇) 0.70; (△) 0.75; (◁) 0.80; (▽) 0.85; (◁) 0.90; (×) 0.95; (+) 1.00. Top Inset: Contact number average $\langle z \rangle$ versus ϕ. The data plotted are: (+) monodisperse; (○) lognormal. The solid lines are Equation (5.1.1) fitted to the monodisperse data (in red) and to the lognormal data (in blue). Bottom Inset: Contact number variance σ_z^2 versus $\langle z \rangle$. The data are labelled the same as in top inset with the addition of lognormal $\sigma_R = 0.10$ (○) and Gaussian $\sigma_R = 0.19$ (△) size distributions.

value for packings with $\langle z \rangle > 9$.

Finally, we show in Figure 5.1.3 the percentage of rattlers in 3D packings, with the percentage of rattlers in 2D shown in the inset of Figure 5.1.3. The presence of rattlers in denser packing fractions and the point at which the population of rattlers becomes negligible has not been reported on previously.

As the relationship between ϕ and the average contact number $\langle z \rangle$ has been shown to be robust for different dimensions and polydispersities, we use $\langle z \rangle$ to parameterize the packing density in Figure 5.1.3. This is the approach we will take for the remainder of this chapter and proves to be a useful measure for the contact properties we will report upon. The behaviour of the rattlers with increasing ϕ is that of diminishing at a similar rate independent of the polydispersity. For 3D, the number of rattlers are all but negligible for $\langle z \rangle > 9$ and the same is true in 2D for packings with $\langle z \rangle > 5.5$.

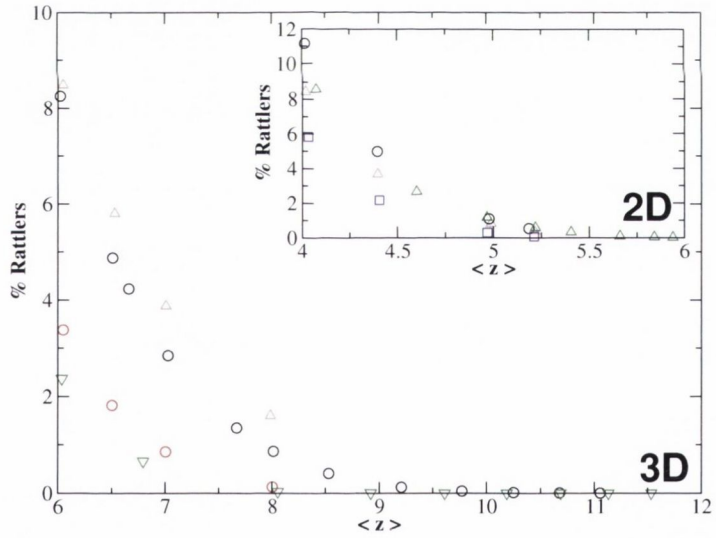

Figure 5.1.3: Percentage of rattlers for increasing ϕ in 3D. The data are labelled the same as in top inset of Figure 5.1.2. Inset: Percentage of rattlers for increasing ϕ in 2D. The data are labelled the same as in top inset of Figure 5.1.1.

5.2 Relationship Between Contact Number and Size

In Chapter 3, we described a relationship between contact number and size in packings at ϕ_c that was linear and independent of polydispersity. In this section we ask does this relationship persist at higher ϕ? Indeed in Figure 5.2.1

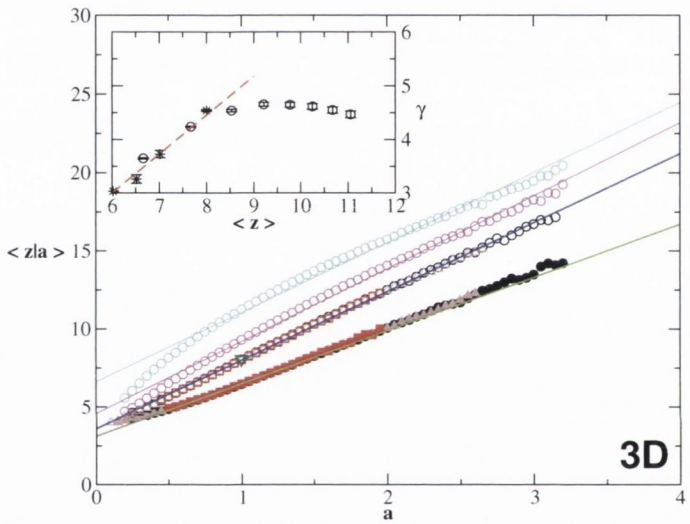

Figure 5.2.1: Average of the contact number distribution for a given area $\langle z|a\rangle$ for increasing packing fraction in 3D. Four size distribution are plotted: monodisperse ($\triangledown$); lognormal $\sigma_R = 0.10$ ($\square$); Gaussian $\sigma_R = 0.19$ ($\triangle$); lognormal $\sigma_R = 0.20$ ($\circ$). The open symbols are for ϕ when $\langle z\rangle = 8.0$ and the closed symbols for $\langle z\rangle = 6.5$. The solid green line is a fit of Equation (3.2.3) to the $\langle z\rangle = 8.0$ data and the solid blue line is a fit of Equation (3.2.3) to the $\langle z\rangle = 6.5$ data. The data in pink is for lognormal $\sigma_R = 0.20$ for $\langle z\rangle = 9.2$ and the data in cyan is for lognormal $\sigma_R = 0.20$ for $\langle z\rangle = 11.05$. Inset: The variation of the fitting parameter γ with $\langle z\rangle$. The data represented by ($*$) are fits to all size distributions. The data represented by ($\circ$) are fitted to the lognormal $\sigma_R = 0.20$ size distribution. The dashed red line is a fit to Equation (5.2.1) for data with $\langle z\rangle < 9$.

for 3D packings, we find a linear trend that is independent of polydispersity. It is important to note that the collapse of $\langle z|a\rangle$ for various polydispersity occurs with the same $\langle z\rangle$.

The linear trend recalls the result shown in Figure 3.2.2 in Section 3.2.1 and therefore Equation (3.2.3) is fitted to the data, with excellent agreement found for $\langle z\rangle < 9$. The functional variation of the fit parameter of Equation (3.2.3), γ, which is plotted in the inset of Figure 5.2.1, is approximately linear for $\langle z\rangle < 9$, which we fit with the following equation,

$$\gamma = \frac{z_c}{2} + \rho\left(\langle z\rangle - z_c\right), \tag{5.2.1}$$

where ρ is a fit parameter and takes a value of $\rho = 0.73 \pm 0.04$ in 3D. As the packings become more dense, and $\langle z\rangle$ increases above 9 the fit to Equation (3.2.3) becomes poorer and the trend in $\langle z|a\rangle$ becomes sub-linear. For the packings with $\langle z\rangle > 9$, the linear fit becomes progressively worse as $\langle z\rangle$ increases. This behaviour is reflected in the behaviour of γ which plateaus for $\langle z\rangle > 9$, however for $\langle z\rangle > 8$ we only have data for the lognormal size distribution.

Stepping down a dimension to 2D, we recover the same relationship that was observed at ϕ_c. In Figure 5.2.2, a linear trend is found for a variety of polydispersities that is well captured by Equation (3.2.6), which was described in Section 3.2.2 for ϕ_c. Unlike in 3D, this linear relationship continues up to the densest ϕ studied. The variation of γ_{2D} with distance to the isostatic point $\langle z\rangle = 4$ is plotted in the inset of Figure 5.2.2, which shows γ_{2D} is linearly increasing up to $\langle z\rangle = 5.5$ and then appears to level out as $\langle z\rangle \to 6$. γ_{2D} for packings with $\langle z\rangle < 5.5$ is found to be fit well by Equation (5.2.1) with the fitting parameter in 2D, $\rho_{2D} = 0.75 \pm 0.05$.

As the average contact number $\langle z\rangle \to 6$, the analogy with a cellular structure becomes more apt. It is interesting to compare this linear relation between contact number and radius to that observed in a variety of cellular structure between the coordination number and cell area called Lewis's

law [69]. This relation has been studied extensively for dry foams [95, 96] but with conflicting results as to whether for polydisperse foams, the relation is better described by Desch's law [97] (also known as Feltham's law [98]), where the contact number is related to the perimeter of the cell.

In both of these relations, the average size of the cell rather than the average contact number is the quantity calculated. As we have previously described in Section 3.4, these two averages are not the same.

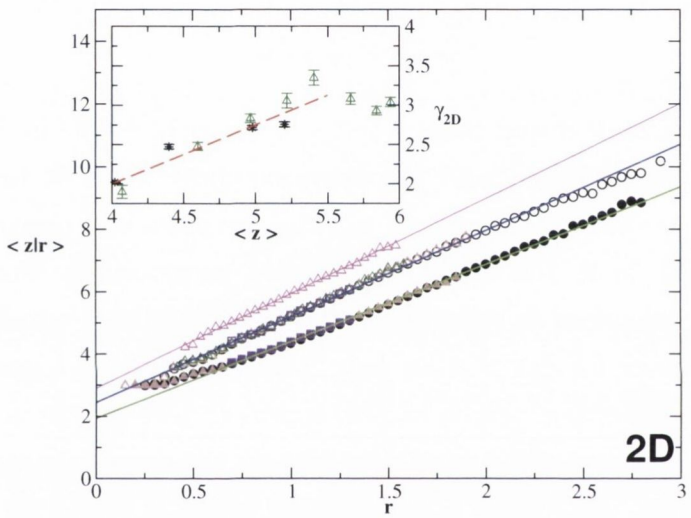

Figure 5.2.2: Average of the contact number distribution for a given size for increasing packing fraction ϕ in 2D. Four size distribution are plotted uniform $\sigma_R = 0.17$ (□); Gaussian $\sigma_R = 0.24$ (△); Gaussian $\sigma_R = 0.28$ (using bubble model code) (△); lognormal $\sigma_R = 0.35$ (○). The open symbols are for ϕ when $\langle z \rangle = 5.2$ and the closed symbols for $\langle z \rangle = 4.4$. The solid red line is a fit of Equation (3.2.6) to the $\langle z \rangle = 5.2$ data and the solid blue line is a fit of Equation (3.2.6) to the $\langle z \rangle = 4.4$ data. The data in pink is for Gaussian $\sigma_R = 0.28$ for $\langle z \rangle = 5.94$. Inset: The variation of the fitting parameter γ_{2D} with $\langle z \rangle$. The data represented by (∗) are fits to all size distributions with the same $\langle z \rangle$. The data represented by (△) are fitted to the Gaussian $\sigma_R = 0.28$ size distribution. The dashed red line is a fit to Equation (5.2.1) for data with $\langle z \rangle < 5.5$.

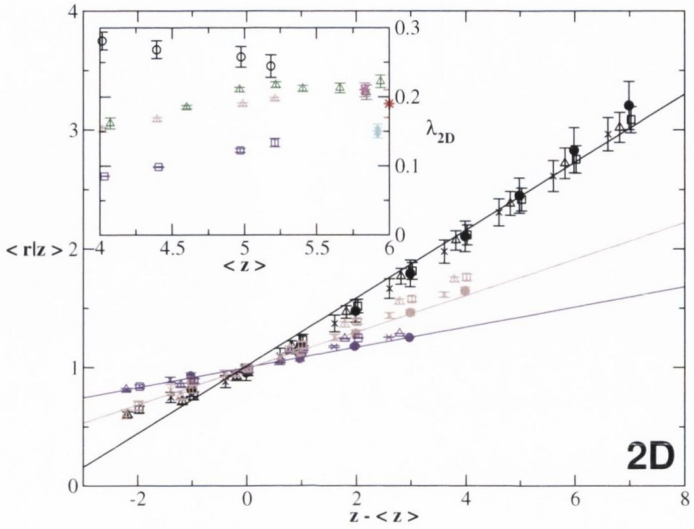

Figure 5.2.3: Average of the radius distribution for particles with a given contact number for increasing packing fraction ϕ in 2D. Three size distribution are plotted uniform $\sigma_R = 0.17$ (purple); Gaussian $\sigma_R = 0.24$ (brown); lognormal $\sigma_R = 0.35$ (black). The data labelled as: $\langle z \rangle = 4.0$ (•); $\langle z \rangle = 4.4$ (×); $\langle z \rangle = 4.98$ (□); $\langle z \rangle = 5.2$ (△). The solid lines are fits of Equation (3.4.8) to the data $\langle z \rangle = 4.0$. Inset: Variation of the fitting parameter λ_{2D} with $\langle z \rangle$. The data is labelled as in top inset of Figure 5.1.1. Comparison is made with experimental data for dry foam: (∗) from [56]; (∗) from [93]; (∗) from [94].

We begin by looking at 2D in order to make the comparison with 2D dry foam results. The average radius for discs with a given contact number $\langle r|z \rangle$ is plotted in Figure 5.2.3 for a variety of size distributions and for increasing packing fraction. Equation (3.4.8) was used in Section 3.4 to fit packings of 2D discs and we find that it describes the trend of the data, particularly for the uniform and Gaussian distributions. The lognormal distribution does deviate from the linear trend and it is not clear that Equation (3.4.8) is the final functional form of $\langle r|z \rangle$. In the limit of large ϕ when the comparison with a cellular structure becomes most appropriate, this would be in best agreement with Desch's law [97].

In the inset of Figure 5.2.3 the behaviour of the fit parameter of Equation (3.4.8), λ_{2D}, is plotted for increasing packing density. Each polydispersity appears to exhibit a linear trend that converges to $\lambda_{2D} \approx 0.2$. We find good agreement with the trend of our data when we compare our results to recent research that fits Desch's law to: 2D foams [94]; the 2D surface of 3D foams [93]; a combination of 2D foams and 2D Potts model and Surface Evolver simulations [56].

Returning to 3D, the situation is similar. As shown in Figure 5.2.4, Equation (3.4.2), which was introduced to describe the trend of $\langle a|z \rangle$ for ϕ_c, describes the behaviour of $\langle a|z \rangle$ with increasing ϕ. However, there are more systematic deviations than observed in 2D. Again, at higher densities, it is

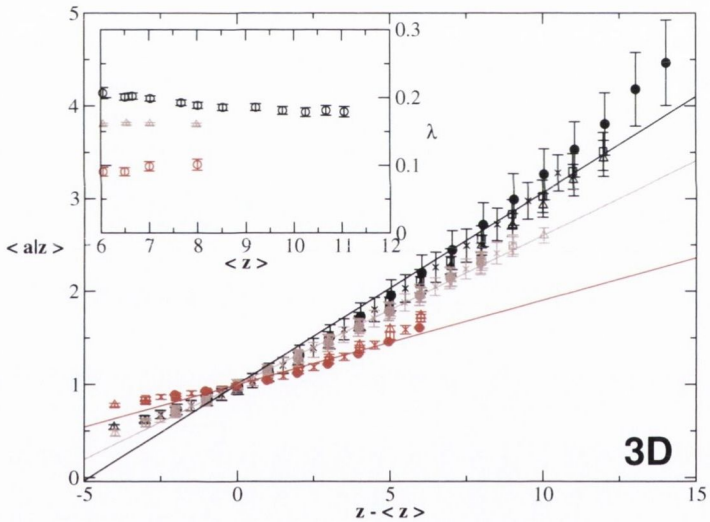

Figure 5.2.4: Average of the area distribution for particles with a given contact number for increasing packing fraction ϕ in 3D. Three size distribution are plotted lognormal $\sigma_R = 0.10$ (red); Gaussian $\sigma_R = 0.19$ (brown); lognormal $\sigma_R = 0.20$ (black). The data labelled as: $\langle z \rangle = 6.0$ (•); $\langle z \rangle = 6.5$ (×); $\langle z \rangle = 7.0$ (□); $\langle z \rangle = 8.0$ (△). The solid lines are fits of Equation (3.4.2) to the data $\langle z \rangle = 6.0$. Inset: Variation of the fitting parameter λ with $\langle z \rangle$. The data is labelled by colour as before.

not completely clear that binning the particle size in terms of a is the best choice. Another difference with the results found for 2D is that there is very little variation of the fitting parameter λ in Equation (3.4.2). Though due to the trend of the data there is reason to suspect that all distributions tend towards a constant $\lambda \approx 0.15$ for large ϕ.

The upshot of using the $\langle a|z \rangle$ linear fit is that it allows us to make a prediction for the contact number variance σ_Z^2, if we have information on the the size distribution through the use of Equations (3.2.3) and (3.4.2). As can be seen in Figure 5.2.5, our prediction underestimates the value of σ_Z^2 but captures the the trend of σ_Z^2. The type of distribution used has an effect on the quality of the prediction, which is linked to the quality of the fit made for $\langle r|z \rangle$ and $\langle a|z \rangle$. Particularly in two dimensions, the prediction is quite successful.

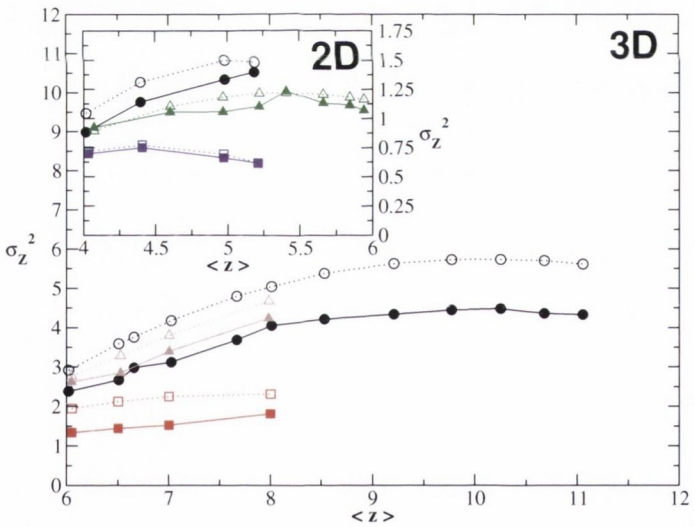

Figure 5.2.5: Variance of the contact number distribution for increasing packing fraction ϕ in 3D with prediction plotted as the closed symbols. Packing data is plotted as open symbols. Inset is the same graph in 2D. The data is labelled as before.

5.3 Granocentric Approach with Increasing Packing Fraction

5.3.1 Three Dimensions

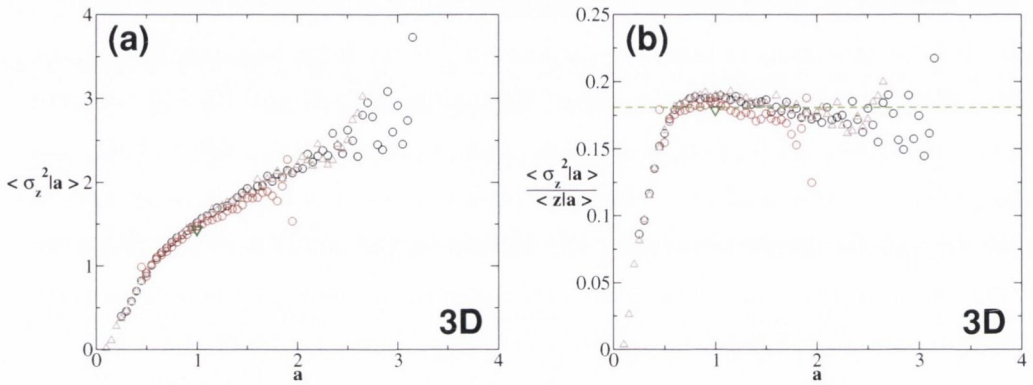

Figure 5.3.1: Collapse of variance and ratio of variance to mean for $\langle z \rangle = 8$ in 3D. Same size distributions plotted as in Figure 5.2.1. (a) The variance of the distribution $P(z|a)$. (b) The ratio of the variance to the average of $P(z|a)$. The dashed green line represents the average value of the plateau.

Having shown that the collapse of $\langle z|a \rangle$ occurs for values of the average contact number $\langle z \rangle$ other than z_c in the previous section, we now investigate whether the mean field approach to predict $P(z)$ taken in Chapter 3 is valid at higher ϕ. Using packings with $\langle z \rangle = 8$ as an example that is typical of denser packings in 3D, the variance $\langle \sigma_Z^2|a \rangle$ and the ratio of the variance to the average contact number are plotted in Figure 5.3.1(a) and (b) respectively. We observe the collapse of both quantities at increased packing fraction with the independence of local contact correlations from the global size distribution persisting at higher packing fractions.

In Figure 5.2.1, the average $\langle z|a \rangle$ collapses for all polydispersities when the $\langle z \rangle$ is the same. The granocentric model was based on the observation that $\langle z|a \rangle$ collapses for all size distribution at ϕ_c, and the demonstration

that $P(z|a)$ depends only on the size of the particle and not the global size distribution. This can be inferred from looking at the width of $P(z|a)$, the variance $\langle \sigma_Z^2 | a \rangle$, which for $\langle z \rangle = 8$ is plotted in Figure 5.3.1 (a). The same collapse for different polydispersities is observed as for ϕ_c, suggesting that $P(z|a)$ is insensitive to polydispersity.

The ratio between $\frac{\langle \sigma_Z^2 | a \rangle}{\langle z|a \rangle}$ for sufficiently large a in Figure 5.3.1 (b), is found to be constant. This plateau suggests an acceptance probability of $p = 0.819$ for the mean field granocentric model. By enforcing that

$$\langle z \rangle = \int_0^\infty z P(z|a) P(a) da = 8, \tag{5.3.1}$$

a value of α can be found. For $\langle z \rangle = 8$ this space limiting parameter is

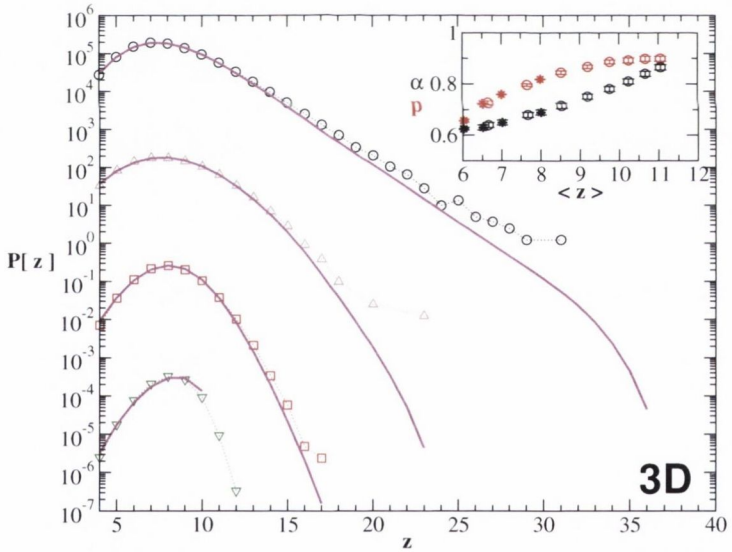

Figure 5.3.2: Model prediction of packings at $\langle z \rangle = 8.0$ for: monodisperse ($\triangledown$); lognormal $\sigma_R = 0.10$ ($\circ$); Gaussian $\sigma_R = 0.19$ ($\triangle$); lognormal $\sigma_R = 0.20$ ($\circ$). The solid pink line is the model prediction. Inset: Model parameters α ($*$) and p ($*$) with increasing $\langle z \rangle$.

$\alpha = 0.69$.

Using the mean field granocentric model outlined for ϕ_c, a prediction of the contact number distribution is made for the size distributions plotted in Figures 5.3.1. The granocentric prediction plotted in Figure 5.3.2 is in good agreement with the data, indicating that this model is just as applicable at $\phi > \phi_c$. The same values of model parameters α and p are used for each size distribution. In the inset of Figure 5.3.2, p and α are plotted and show that both parameters increase for increasing ϕ.

5.3.2 Two Dimensions

We now investigate whether the variance and the ratio of the variance to the mean collapse for 2D disc packings. Using packings with $\langle z \rangle = 5.2$ as an example that is typical of denser packings in 2D, the variance $\langle \sigma_Z^2 | r \rangle$ and the ratio of the variance to the average contact number is plotted in Figure 5.2.2. We observe a similar collapse as the packing fraction is increased with the independence of local contact-size correlations from the global size

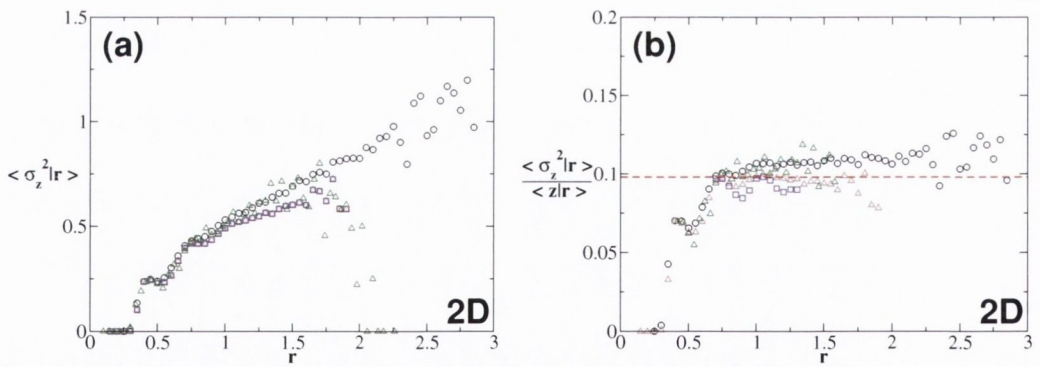

Figure 5.3.3: Collapse of variance and ratio of variance to mean for $\langle z \rangle = 5.2$ in 2D. Same size distributions plotted as in Figure 5.2.2. (a) The variance of the distribution $P(z|r)$. (b) The ratio of the variance to the average of $P(z|r)$. The dashed red line represents the average value of the plateau.

distribution persisting at higher packing fractions.

Having already seen in Figure 5.2.2 that the average $\langle z|r\rangle$ collapses for all polydispersities when the $\langle z\rangle$ is the same, we make the same inference from Figure 5.3.3 that $P(z|r)$ is the same for all r independent of packing fraction, given the variance $\langle \sigma_Z^2|r\rangle$ collapses, similar to that observed for ϕ_c.

A plateau is observed for the ratio between $\frac{\langle \sigma_Z^2|r\rangle}{\langle z|r\rangle}$ for sufficiently large r in Figure 5.3.3 (b). The plateau suggests an acceptance probability of $p = 0.92$. By enforcing that

$$\langle z\rangle = \int_0^\infty zP(z|r)P(r)dr = 5.2, \tag{5.3.2}$$

a value of α can be found. For $\langle z\rangle = 5.2$ this parameter is $\alpha = 1.02$.

Using the mean field granocentric model, a prediction of the contact num-

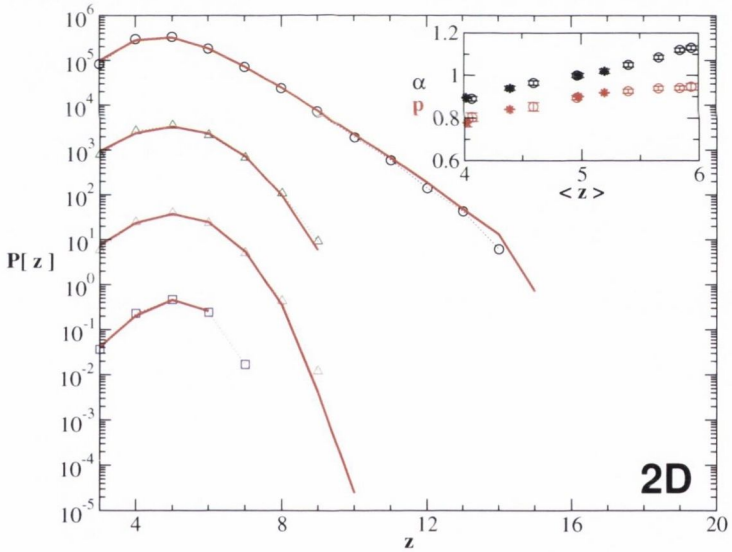

Figure 5.3.4: Model prediction of packings at $\langle z\rangle = 5.2$ in 2D for the same size distributions as previously. The solid red line is the model prediction. Inset: Granocentric model parameters α (*) and p (*) with increasing $\langle z\rangle$ in 2D.

ber distribution for $\langle z \rangle = 5.2$ is made in Figure 5.3.4. The granocentric prediction is in good agreement with the data, indicating that this model is applicable at $\phi > \phi_c$ for 2D as well. The value of α and p are independent of size distribution. In the inset of Figure 5.3.4 the model parameters p and α are plotted, and show that for increasing ϕ both these parameters grow.

5.4 Correlations in Nearest Neighbour Contacts

In Chapter 4 we outlined how structure of disordered packings at ϕ_c exhibits spatial correlations in the contact network. In this section we examine the manner in which these correlations persist in denser packings.

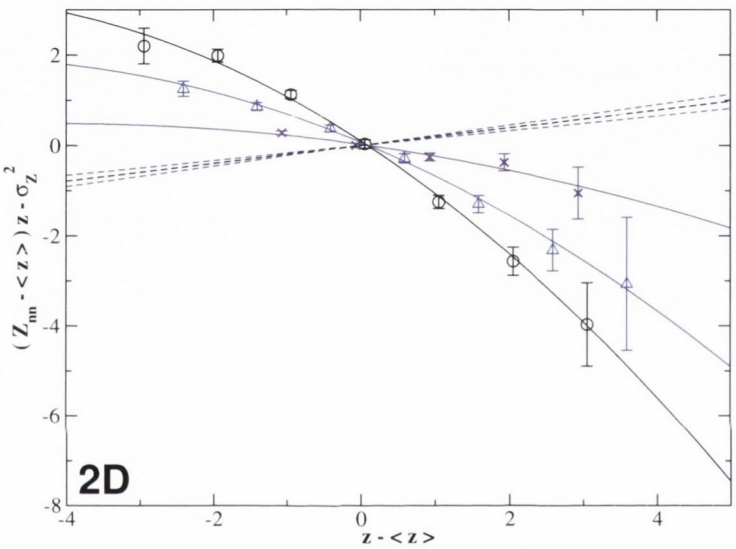

Figure 5.4.1: Anti-correlation of neighbouring particles contact number for increasing packing fraction ϕ in 2D packings using the bubble model algorithm. Three densities for a Gaussian ($\sigma_R = 0.28$) distribution are plotted: $\langle z \rangle = 4.07$ ($\times$); $\langle z \rangle = 5.40$ ($\triangle$); $\langle z \rangle = 5.94$ ($\circ$). The solid lines are Equation (4.1.13) fitted to the data and the dashed lines are the uncorrelated prediction of Equation (4.1.10).

5.4.1 Contact Number Correlations in 2D

First turning our attention to 2D, we look at results for Z_{nn}, which are shown in Figure 5.4.1, where we plot $(Z_{nn} - \langle z \rangle)z - \sigma_z^2$ versus $(z - \langle z \rangle)$ for

three different packing fractions. If the original form of the Aboav-Weaire correlation for discs (Equation (4.1.12)) is to hold we expect the data to follow a line with slope $-a$. Clearly, the data does not follow the uncorrelated prediction (Equation (4.1.10)). Instead we observe anti-correlations in the contact network: discs with few contacts are surrounded by discs with many contacts and vice versa. We note that there are the deviations from purely linear behaviour, especially at higher packing fractions. This suggests that the relation used in Chapter 4 for 2D packings at ϕ_c is not adequate.

We turn to the second term in the expansion of Equation (4.1.11) and keeping only the second term non-zero, we recover Equation (4.1.13) proposed

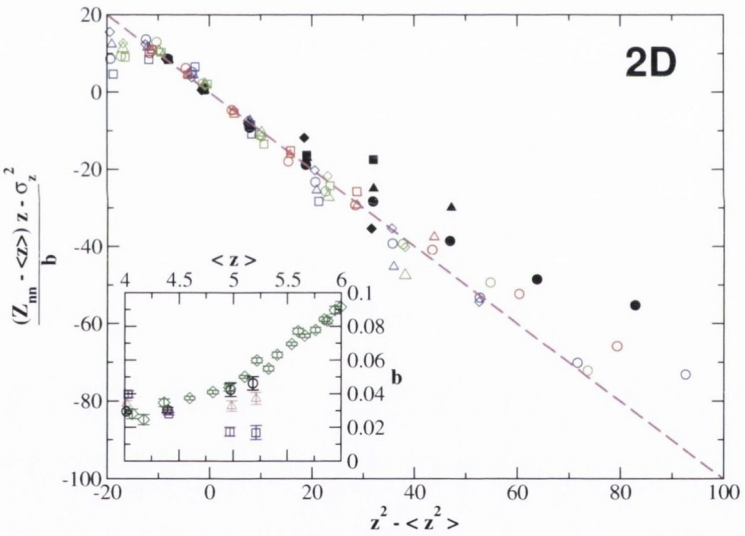

Figure 5.4.2: Anti-correlation of neighbouring particles contact number for increasing density in 2D for a variety of size distributions. Four different size distributions are plotted: uniform $\sigma_R = 0.17$ (□); Gaussian $\sigma_R = 0.24$ (△); Gaussian (dynamic) $\sigma_R = 0.28$ (◇); lognormal $\sigma_R = 0.35$ (○). The data is labelled for increasing $\langle z \rangle \approx$: 4.0; 4.4; 4.98; 5.2.The dashed line has a slope of -1. Inset: Fit parameter b as function of $\langle z \rangle$. Data is labelled the same as Figure 5.2.3.

previously for 3D, which we rewrite below,

$$\frac{(Z_{nn} - \langle z \rangle)\, z - \sigma_Z^2}{b} = -1 \left(z^2 - \langle z^2 \rangle \right). \tag{5.4.1}$$

As shown in Figure 5.4.1, Equation (5.4.1) captures the non-linearity well and leads to a much improved fit compared to Equation (4.1.12). Including higher order terms in the expansion Equation (4.1.11) does not improve the fit significantly.

We find that Equation (4.1.13) best captures the trend of the data for other polydispersities plotted in Figure 5.4.2. Plotting the data in Figure 5.4.2 with axes such that agreement with Equation (5.4.1) gives a trend with slope -1, we find excellent agreement for all data with $\langle z \rangle > z_c + 0.05$ with only slight deviation for low z at higher densities.

For data at the isostatic point, the trend typically deviates upwards in Figure 5.4.2 (the black filled symbols) from that predicted by Equation (5.4.1). This indicates that this data is better described by the original form of the Aboav-Weaire correlation (Equation (4.1.12)) as seen in Section 4.1.5. We do not have an explanation for why this crossover from one trend to the other is observed.

The inset of Figure 5.4.2 shows the change of the parameter b with $\langle z \rangle$. The behaviour of the a parameter in the Aboav-Weaire law for cellular structures has been linked to σ_Z^2 (see Figure 5.2.5). It is interesting to note that the general trend of b is similar to that of σ_Z^2. Packings with wide size distributions have wider contact number distributions as the density is increased and a larger b. The opposite is true of narrow distributions such as the uniform $\sigma_R = 0.17$, where σ_Z^2 is a decreasing function of density and the resulting b also decrease.

5.4.2 Contact Number Correlations in 3D

Turning our attention to 3D sphere packings at higher densities, we find that in the case of polydisperse packings the contact number correlations reported at ϕ_c persist. In Figure 5.4.3 the relationship between z and $Z_{nn}(z)$ is plotted in the manner of Equation (5.4.1), where perfect agreement would lead to a slope of -1 and for much of the range of data there is excellent agreement. Only for dense packings and low z are deviations found that are not captured by Equation (5.4.1). Given the expansion that we use, it is difficult to find some form that would describe these deviations. We believe that the existence of these deviations for lower ϕ is due to the clusters of smaller particles that would be rattlers at a lower density but which are now in the contact network. These small particles with low contact number that join the contact network in clusters lower the average contact number of the surrounding particles.

The parameter b is plotted in the bottom inset of Figure 5.4.3. For polydisperse distributions the evolution of b with increasing density is more complicated than the case in 2D. Broadly, b for polydisperse distributions does not change significantly with increasing $\langle z \rangle$ in 3D, with the trend suggesting that b may tend to a constant 0.015 ± 0.005 for higher values of ϕ. In the case of monodisperse the trend is much clearer, linearly decreasing b with increasing $\langle z \rangle$.

The top inset of Figure 5.4.3 shows the contact correlations for a monodisperse packing at $\phi = 0.75$ and it is clear that relationship between Z_{nn} and z is not well described by Equation (5.4.1). Large z are no longer anti-correlated but positively correlated, particles with large contact numbers are typically in contact with particles that have larger than average contact number. This behaviour may indicate crystalline ordering as discussed in Appendix B. The physical significance of the b parameter has yet to be determined but could be of interest as a measure of the transition from disordered structures to ordered structures.

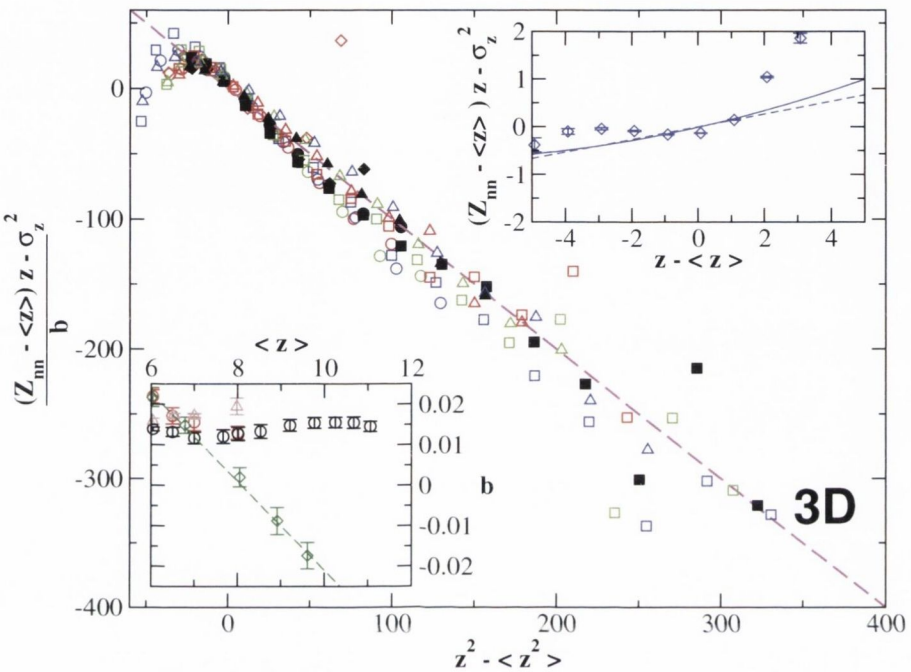

Figure 5.4.3: Anti-correlation of neighbouring particles contact number for increasing density in 3D. Four different size distributions are plotted: monodisperse (◇); lognormal $\sigma_R = 0.10$ (□); Gaussian $\sigma_R = 0.19$ (△); lognormal $\sigma_R = 0.20$ (○). The dashed line has a slope of -1. The data is colour coded for increasing $\langle z \rangle \approx$: 6.0; 6.5; 7.0; 8.0 or in the case of the monodisperse packing the order in which the packings appear in the bottom inset. Bottom inset: Fit parameter b as function of $\langle z \rangle$. Data is labelled the same as Figure 5.2.4. The dashed line is a linear fit to monodisperse data to act as a guide to the eye. Top inset: Anti-correlation of neighbouring particles contact number for monodisperse distribution at $\langle z \rangle = 8.9$ with fit to Equation (5.4.1) represented by solid line. The dashed line represents the trend expected from an uncorrelated packing.

5.5 Correlations in Nearest Neighbour Size

5.5.1 Size Correlations in 2D

As observed for 2D packings at ϕ_c, there are no strong correlations in the size of nearest neighbours for denser packings. In Figure 5.5.1, there is little deviation from the expected uncorrelated value of the average neighbour radius. In Figure 5.5.1 (a) and (b) for small r there are deviations due to particles that might otherwise be rattlers being in contact with larger particles. The only way such particles are counted in this analysis is if they can form sufficient contacts in the interstices between large particles. Figure 5.5.1 (d) shows that there is little variation of $\overline{R}_{nn}$ with ϕ.

5.5.2 Size Correlations in 3D

Figure 5.5.2(a)-(c) shows for 3D packings that Equation (4.2.8) continues to describe the correlation between a and the average area of neighbouring particles A_{nn}, for data with $\langle z \rangle < 9$. Deviations from the uncorrelated prediction are small.

The exception to that behaviour is the transition of A_{nn} for lognormal distributions, which become flat for $\langle z \rangle = 11.05$ and is plotted in Figure 5.5.2(a). The transition is continuous from the correlations observed at $\langle z \rangle = 8$, similar to those at ϕ_c, to the lack of correlations at high ϕ. There is no data for other polydispersities with $\langle z \rangle > 8$ to compare to the dense lognormal data.

Figure 5.5.2(d) shows some small variation with $\langle z \rangle$, the amount of increase in $\overline{A}_{nn}$ appears to be σ_R dependent. The slight increase of $\overline{R}_{nn}$ and $\overline{A}_{nn}$ is due to larger cells having more contacts with increasing ϕ.

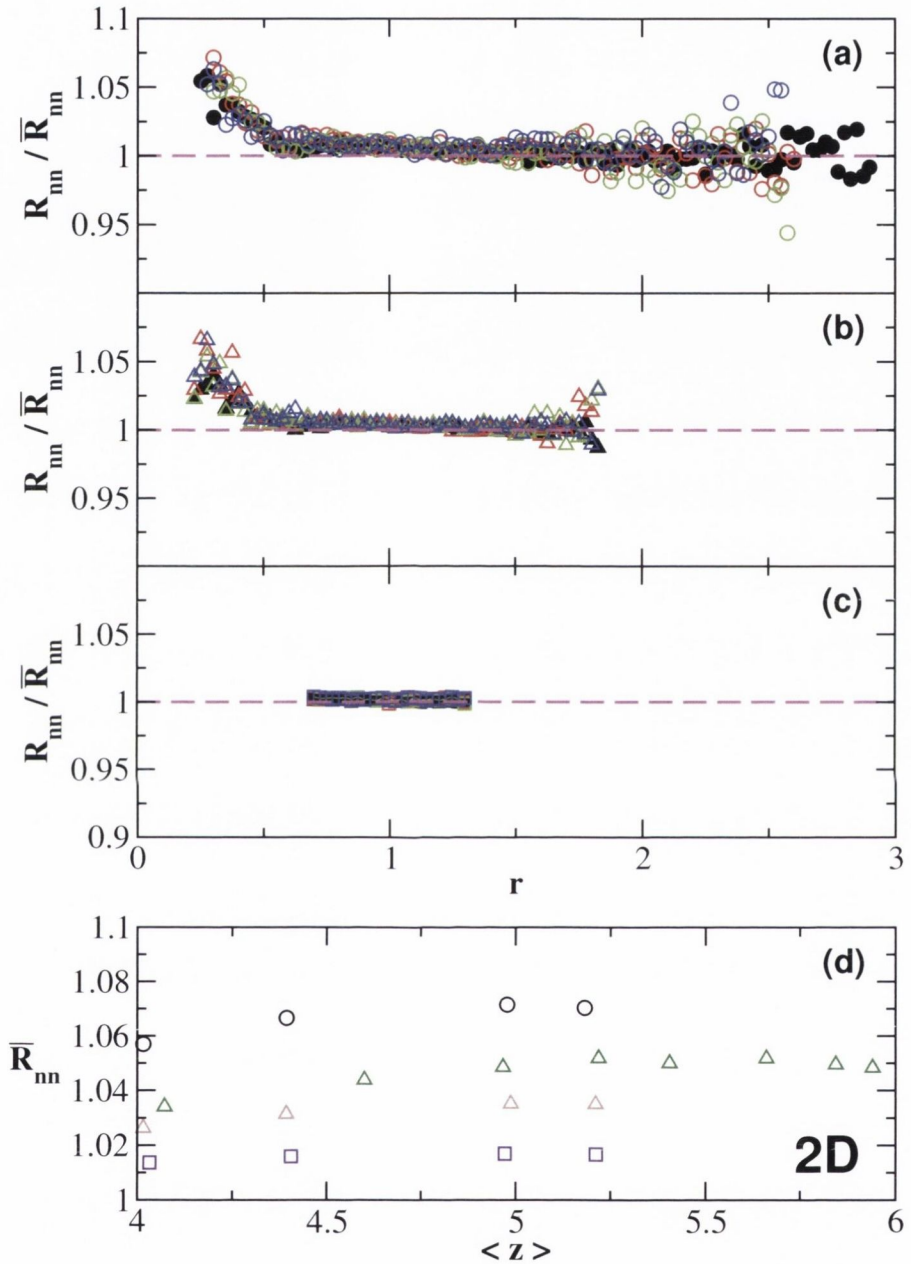

Figure 5.5.1: Correlations between size of discs in contact for increasing ϕ in 2D. (a)-(c) Three different size distributions with the same symbols and coloured in the same manner as in Figure 5.4.2. The dashed line represents the uncorrelated prediction. (d) Uncorrelated prediction $\overline{R}_{nn}$ with increasing $\langle z \rangle$ for the same distribution as in Figure 5.4.2.

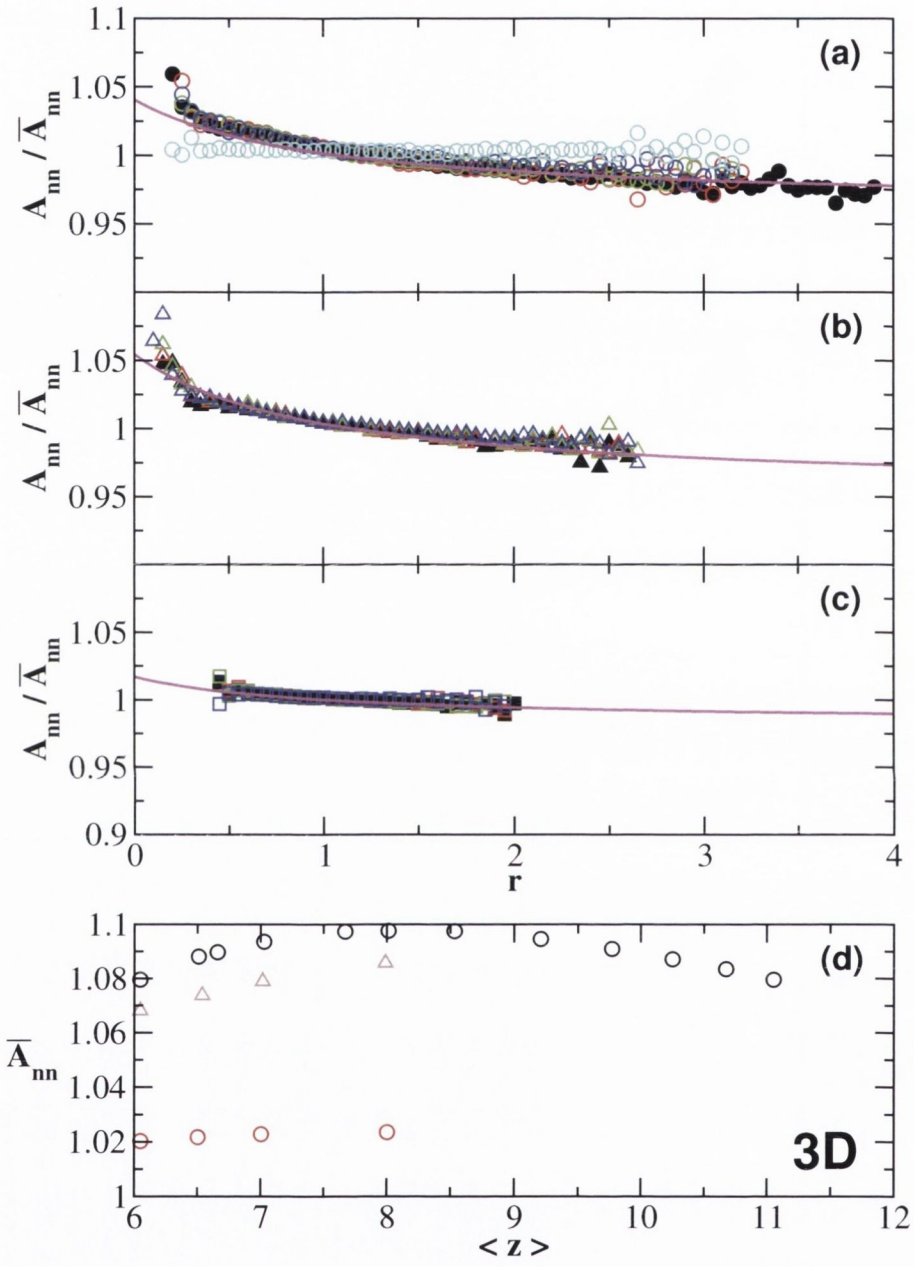

Figure 5.5.2: Correlations between size of spheres in contact for increasing ϕ in 3D. Plotted in (a) is lognormal $\sigma_R = 0.20$, (b) is Gaussian $\sigma_R = 0.19$, (c) is lognormal $\sigma_R = 0.10$. The plot is coloured in the same manner as in Figure 5.4.3 with the addition of (○) lognormal $\langle z \rangle = 11.05$ in (a). The solid line represents a fit of Equation (4.2.8) to the isostatic data set. (d) Uncorrelated prediction $\overline{A}_{nn}$ with increasing $\langle z \rangle$ for the same distribution as in Figure 5.4.3.

5.6 Conclusions & Outlook

We conclude that packing fraction does not have a strong effect on the shape of $P(z)$ for soft particle packings due to the manner in which it can be generically rescaled for both 2D and 3D for a given size distribution. This again demonstrates that the dominant factor in setting the contact distribution is the size distribution.

The linear trends observed in $\langle z|a\rangle$ and $\langle z|r\rangle$ persist at higher ϕ in 3D and 2D, respectively. Although for 3D packings with $\langle z\rangle > 9$, this linear trend begins to break down. The parameters of the linear fits over the range in which they are applicable are described by the same equation in 2D and 3D.

Similar to the averages, the variance and the ratio of variance to mean of particles of a given a and r, in 3D and 2D respectively, collapse independent of polydispersity, provided $\langle z\rangle$ is the same. This suggests the use of the mean field granocentric model, which successfully predicts the $P(z)$ for all polydispersities with $\phi > \phi_c$.

We find that the linear descriptions of $\langle a|z\rangle$ and $\langle r|z\rangle$ found at ϕ_c are also valid at higher densities. For very dense packings the fitting parameters of both relations in 3D and 2D appear to tend to constants that are independent of polydispersity. The value of this fitting parameter for $\langle r|z\rangle$ as $\langle z\rangle \to 6$ is similar to that found for Desch's law in dry foams.

Spatial correlations in nearest neighbour size and nearest neighbour contact network also persist in denser packings, but remain weak. Notable dissimilarities between the results at high ϕ to those found at ϕ_c include the observation that 2D nearest neighbour contact correlations are described using only the second term in Equation (4.1.11) rather than the first used at ϕ_c. Also, 3D monodisperse packings show a tendency of their contact network to be positively correlated in contact number for dense packings. The fitting parameter b describing the trend of this correlation decreases linearly suggesting ordering for monodisperse packings at higher ϕ. Nearest neighbour

correlations in size disappear for the lognormal distribution for $\langle z \rangle > 9$ in 3D.

There is a suggestion of a transition at $\langle z \rangle = 9$ in 3D. This has only been studied for polydisperse lognormal packings and in order to elucidate the structure of dense disordered packings it merits further investigation.

Part II

Rheology

Chapter 6

Introduction to Rheology

In Part I of this thesis we reported on the static contact properties of jammed collections of particles and investigated how these properties change as the distance from the jamming point is increased, this distance being tuned by the packing fraction. In Part II, we look at wet foam where bubbles are simulated as soft discs as outlined in Section 2.2.1. Our focus is on the transition between jammed solid-like properties of disordered particles to unjammed fluid-like behaviour by applying a shear stress, thereby investigating the jamming phase diagram (see Figure 1.2.1) through the other axis.

In Chapter 7, we will examine the constitutive equation for foam in an annular geometry where the shear stress is inhomogenous and investigate whether proposed models of flow in foams and emulsions describe the flow of soft discs in this geometry.

In Chapter 8, we will study some emergent properties of soft disc packings under shear in a rotating drum setup, which are inspired by recent results in foams and granular media. Among the properties that the two materials share, we are particularly interested in the static angle of repose and the shear dilatancy.

6.1 Foam Rheology

For most common fluids the viscosity $\eta = \sigma/\dot{\gamma}$ is a constant, where σ is the shear stress and $\dot{\gamma}$ is the strain rate. Liquids that have a constant η are called Newtonian fluids. Foams are non-Newtonian, in the class of fluids which are called shear thinning, where the viscosity decreases with strain rate.

Wet foams may be regarded as an elastic solid or a viscous fluid depending on whether the shear stress that is applied is greater than the yield stress σ_y, the threshold that separates the two behaviours. Below the yield stress the foam behaves like a solid and is subjected to elastic deformation, while if we now increase the stress so that it exceeds the yield stress σ_y, the foam will yield, and begin to flow so that the effective viscosity of the foam changes according to the shear stress applied. The yield stress of a foam is a function of the packing fraction of the foam [99].

While foams are a collection of interacting bubbles on the particle scale, there exist empirical models to account for the flowing behaviour using continuum approaches on the macroscopic scale. This leads to the Herschel–Bulkley model [100], the constitutive equation for foam flow:

$$\sigma = \begin{cases} \sigma_y + c_v \dot{\gamma}^{\beta}, & \text{if } \sigma > \sigma_y \\ \dot{\gamma} = 0, & \text{otherwise} \end{cases} \tag{6.1.1}$$

where c_v is called the consistency and is a measure of the fluid's resistance to flow, $\dot{\gamma}$ is the rate of strain, and β is known as the Herschel-Bulkley exponent.

In recent years progress has been made to connect foam rheology with that of granular materials [101]. We consider granular matter that, unlike foam, does not deform and possesses static friction in its particle interaction. In foams and emulsions the relationship between shear stress and shear strain rate is often measured at constant ϕ, and the model parameters of Equation (6.1.1) are dependent upon ϕ. For granular systems measuring at constant ϕ is difficult as grains dilate upon shear, affecting the packing fraction. There-

fore granular experiments are often conducted under a constant confining pressure. Equations of the form of Equation (6.1.1) also exist for the flow of granular materials but are given in terms of μ, the macroscopic friction coefficient, which is defined as the ratio of the shear stress σ to the normal stress P. Equations have been proposed that apply to both materials, of the form,

$$\mu = \mu_R + y(I), \tag{6.1.2}$$

where I is a dimensionless shear rate. In grains, I is related to $\dot{\gamma}$ by an inertial rearrangement timescale, while in foams and suspensions, I is scaled by a viscous timescale. y is a function for which some recent empirical models have been proposed [102, 103] and takes a form similar to that of the Herschel–Bulkley equation. Finally, μ_R is a critical macroscopic friction which for granular material has been known to take a value that resembles that of the static interaction friction of the material. Recent experiments and simulations of frictionless particles have shown that μ_R is non-zero despite the lack of solid friction between bubbles [103, 104, 105].

6.2 Herschel–Bulkley Rheology

In the last decade there has been much study of two-dimensional foams as a simplified model of three-dimensional foam. From an experimental point of view this allows tracking of individual bubbles moving in a sheared foam allowing velocity profiles to be found. In experiments the flow of two dimensional foams has been studied using a number of setups. These setups include a linear geometry with a confining top-plate, where the foam was sheared in opposite directions by the confining walls [45] and an annular Taylor-Couette setup where the outer wall sheared the foam and the inner wall was held fixed [106].

One of the first attempts to explain the empirical Herschel-Bulkley regime was by Princen [107]. Developed for ordered foams, this model is based upon the energy dissipation due to slip along the crystalline planes in the ordered structure. From the Princen model a theoretical value of the Herschel-Bulkley exponent $\beta = 2/3$ was predicted [108]. More recently, this model has been refined to account for surfactant effects on viscous dissipation in the films [109]. Another model by Tighe et al. [110] derives the Herschel-Bulkley rheology from a relaxation/dissipation ansatz.

A range of values have been found for the Herschel–Bulkley exponent β from 0.2 to 0.5 [45, 109, 112], which has been attributed to the chemistry of the surfactants used [47]. For the simulation of soft discs in a linear geometry, the Herschel–Bulkley exponent is $\beta \approx 0.5$ [43, 49, 113]. The principle difference between experiments have been the geometries in which they have been conducted. Recently, it has been shown that while the Herschel–Bulkley relation describes foam in a setup with linear shear [49], it is inconsistent with rheological measurements for a Taylor–Couette (circular) geometry shown in Figure 6.2.1 [111], this geometry is often referred to as a Couette geometry. The inconsistency between the flow in different geometries is elaborated on in the following analysis.

In a linear geometry the relationship between the shear stress σ and the

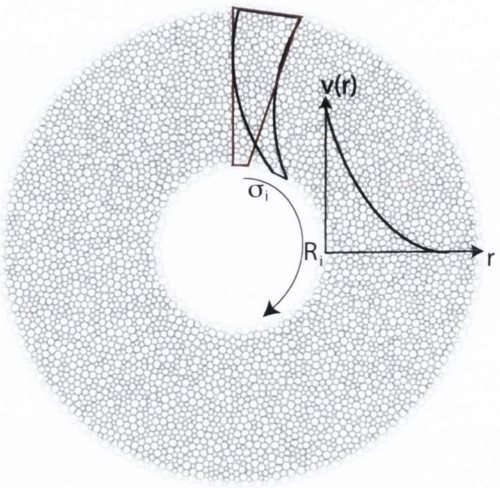

Figure 6.2.1: Sketch of the experimental setup used by Katgert et al. [111] to shear two dimensional foams in a Couette geometry. In this setup there is no confining top plate. The red triangle is a section of the foam that is deformed into the shape formed by the black border due to the strain γ applied to the foam. σ_i measures the stress on the inner wall from straining the foam. On the right is a sketch of the velocity profile of the foam flow, which is dependent upon r.

strain rate $\dot{\gamma}$ is unique for a given imposed shear, while in a Couette geometry this relationship can vary with distance to the shearing boundary. This non-unique relationship between σ and $\dot{\gamma}$ which depends upon the external forcing and the geometry is called non-local rheology. Shearing in a Couette geometry creates a more complicated flow than the linear geometry. For a continuum fluid a linear geometry will have a constant shear stress across the flow, while in the Couette case the shear stress will vary with $1/r^2$. For a sufficiently large number of particles between the confining walls this continuum approach is appropriate. This allows a direct probe of the Herschel–Bulkley relation for a single driving rate or applied stress, provided that the velocity

profile is measured. If we take a continuum description of foam and deal only with local averages of stress σ, strain γ and angular velocity u_θ then, for continuous shear of foam in a Couette geometry, the Cauchy equilibrium criterion in polar coordinates (see Appendix C.1) is,

$$\frac{\partial \sigma}{\partial r} + \frac{2\sigma}{r} = 0. \tag{6.2.1}$$

Equation (6.2.1) can be solved for the case of a moving inner boundary as,

$$\sigma(r) = \sigma_i \left(\frac{R_i}{r} \right)^2, \tag{6.2.2}$$

where σ_i is the stress on the inner boundary, R_i is the inner radius and r is the radial position in between the two concentric walls. The strain rate in this geometry is given by,

$$\dot{\gamma}(r) = \left| \frac{\partial u_\theta}{\partial r} - \frac{u_\theta}{r} \right|. \tag{6.2.3}$$

For more detail on strain rate in polar coordinate system see Appendix C.2. By substituting Equation (6.2.2) and Equation (6.2.3) into Equation (6.1.1) we obtain

$$\sigma = \sigma_y + c_v \left(\frac{u_\theta}{r} - \frac{\partial u_\theta}{\partial r} \right)^\beta. \tag{6.2.4}$$

An expression for the velocity profile can be found by substituting Equation (6.2.4) into Equation (6.2.1) giving

$$\frac{\partial^2 u_\theta}{\partial r^2} = \left(\frac{2}{\beta} - 1 \right) \left(\frac{u_\theta}{r^2} - \frac{1}{r} \frac{\partial u_\theta}{\partial r} \right) + \frac{2\sigma_y}{\beta c_v r} \left(\frac{u_\theta}{r} - \frac{\partial u_\theta}{\partial r} \right)^{1-\beta}. \tag{6.2.5}$$

In general Equation (6.2.5) can be solved numerically [114].

Previously, the Herschel–Bulkley equation had been found to successfully describe velocity profiles in a linearly sheared monolayer by balancing the stresses with the drag force due to an enclosing top plate. However, it has

been shown for a Couette geometry that this model fails. Katgert et al. [111] sheared a monolayer of foam in the setup shown in Figure 6.2.1, for various values of the wall velocity U_0. Equation (6.2.3) was used to calculate the local strain rate $\dot{\gamma}$ and Equation (6.2.2) to calculate the local stress $\sigma(r)$. Two surprising results were found. Firstly, the Herschel–Bulkley model predicts that the normalised velocity profiles should change with the driving velocity U_0 but the profiles did not change; the velocity profiles were rate independent. Secondly, as plotted in Figure 6.2.2, the calculated local stress $\sigma(r)$ and strain rate $\dot{\gamma}(r)$ for a given driving velocity did not collapse onto a single σ versus $\dot{\gamma}$ curve. Finally, it was noted that there was flow below the yield stress of the bulk material, which was calculated from fitting the Herschel–Bulkley equation to the shear stress measured at the inner boundary.

In other experiments it has been observed that for narrow gap systems of 3D emulsion flows that the local and global flow differ [115] (emulsions have similar rheological properties to foams). Goyon et al. [115] showed that in a narrow microchannel, where σ and $\dot{\gamma}$ varied throughout the channel, that the local flow curves did not collapse unto a single rheological curve for different forcing of the emulsion in the channel. This suggests a similar non-local continuum model to that of Goyon et al. [115] as an explanation for the difference between the local and global rheology noticed by Katgert *et al.* To account for this non-local behaviour, a fluidity parameter

$$f = \dot{\gamma}/\sigma, \tag{6.2.6}$$

was introduced. This parameter f, is the inverse viscosity and is essentially a measure of a material's propensity to flow. It is position dependent. The fluidity parameter arises due to plastic rearrangements in flowing foams inducing rearrangements elsewhere in the bulk foam. While plastic rearrangements are clearly visible in dry foams, wet foams also undergo analogous irreversible localised plastic rearrangements which is associated with a local yield stress between the interacting bubbles [116].

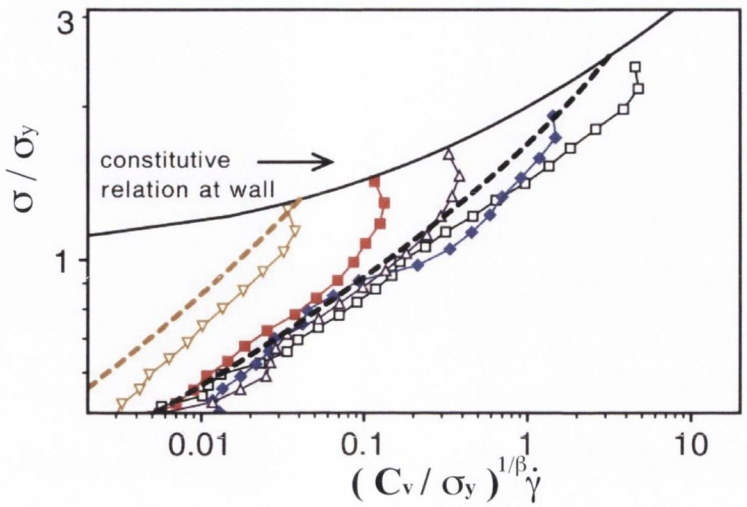

Figure 6.2.2: Scaled stress versus strain rate curve produced with setup in 6.2.1, as shown by Katgert et al. [111]. Local flow curves in Couette geometry for 5 different driving rates U_0: (□) 6.31 mm/s; (♦) 2.15 mm/s; (△) 0.615 mm/s; (■) 0.22 mm/s; (▽) 0.056 mm/s. The solid curve is the Herschel–Bulkley fitted to measurements taken on the inner shearing wall for different driving velocities. The dashed curve is the prediction of the fluidity model with ξ constant for the slowest and fastest driving velocities.

This non-locality is predicted when the relative stress gradient $\nabla\sigma/\sigma$ becomes comparable to the bubble scale. In general, a system with homogeneous stress will have a bulk fluidity f_b that depends only on the local shear rate and is given by,

$$f_b = \frac{1}{\sigma}\left(\frac{\sigma - \sigma_y}{c_v}\right)^{\frac{1}{\beta}} H(\sigma - \sigma_y), \tag{6.2.7}$$

where H is the unit step function. The most favourable configuration for the foam is to have $f = f_b$ everywhere, however due to the inhomogeneities in the flow there are spatial variations in f. It can be shown by taking the Taylor

expansion of $f(x) = f$ to the second order [116] that the fluidity obeys an equation of form,

$$f_b(x) - f(x) + \xi^2 \frac{\partial^2}{\partial x^2} f(x) = 0, \tag{6.2.8}$$

where ξ is the flow cooperativity length, which characterises the non-local effects and the first derivative in the expansion of f is zero because the fluidity must be a symmetric function. Effectively ξ measures the distance from where flow in one part of the system can affect flow in another part. In the emulsion flow experiment by Goyon et al. [115] it was typically several droplet diameters.

There have been many experiments undertaken for 2D foams in a Couette geometry, however, soft discs simulations have not been previously used to study the rheology in this geometry. In a recent work Mansard et al. [113] performed 2D simulations in a geometry with nonuniform stress across it, observing non-local flow.

The focus of this research is to test whether the experimental results found by Katgert et al. can be reproduced in soft disc simulations. Using Equation (6.2.2) and Equation (6.2.3) to calculate the local stress σ and strain rate $\dot{\gamma}$, we investigate whether they collapse onto a single rheological curve or whether a non-local rheology is observed. Furthermore, we compare this local stress-strain rate relation to the Herschel–Bulkley relation found in simulations of sheared soft discs in a linear geometry. Finally, we investigate the effect of changing packing fraction on the rheology.

6.3 Macroscopic Friction

Even though bubbles do not exhibit any static friction, recent experiments [104] and simulations [103, 117, 118, 105] have shown that there is an effective or macroscopic friction that affects the flow of foams. Does this macroscopic friction μ result in a stable pile of bubbles with a non-zero angle?

6.3.1 Static Angle of Repose

The static angle of repose is a well known property in granular media. One of the most common instances of this phenomenon is the piling of sand on a plane surface (Figure 6.3.1 (a)). When a sufficient amount of grains are poured, a conical heap is formed. The slope of the pile describes an angle with the surface. The static angle of repose θ_R is the maximum angle the pile forms before particles begin to fall down the slope. In the example of sand, a simple theory allows an estimate of the angle of repose formed by spherical particles, using Coulomb friction [119].

Considering a particle on top of a sand pile, the forces applied on it (as shown in Figure 6.3.1 (b)), are $\vec{\mathbf{S}}$, the force of the gravity on the particle; $\vec{\mathbf{N}}$, the normal force on the particle against the surface of the pile; $\vec{\mathbf{T}}$, the frictional force on the particle.

From Coulomb's theory of friction, T takes a value between 0 and μN,

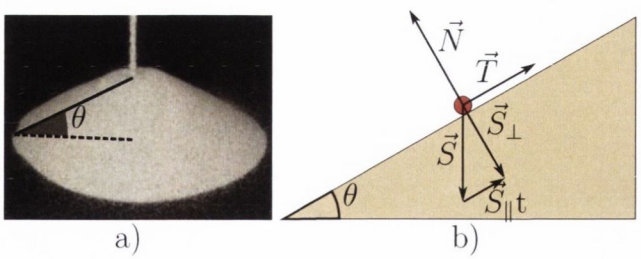

Figure 6.3.1: (a) Sand pile with an indication of the static angle of repose. (b) Vector diagram of the forces acting on a grain.

where μ is the coefficient of static friction. In equilibrium we obtain:

$$\vec{\mathbf{N}} + \vec{\mathbf{S}} + \vec{\mathbf{T}} = \vec{\mathbf{0}}. \tag{6.3.1}$$

$\vec{\mathbf{S}}$ is decomposed in two components: $S_\perp$, the normal component, perpendicular to the slope and $S_\parallel$, the shear component parallel to the slope. From the action reaction between the pile and the particle we get that:

$$N = -S_\perp = -S\cos\theta. \tag{6.3.2}$$

The projection of the forces (Equation (6.3.1)) on the slope gives:

$$T = -S_\parallel = -S\sin\theta. \tag{6.3.3}$$

If $S_\perp < T$, then the ratio of shear to normal stress, gives the angle of repose:

$$\tan\theta_R = \mu. \tag{6.3.4}$$

This has been shown to be a good estimator of the friction of a material.

Despite the great challenge to understand friction at a fundamental level [120], by knowing the effective friction μ we are able to estimate a value for the angle of repose. In foams, there is no static friction and $\mu = 0$, however it has been found in experiments of the flow of foams on inclined planes that there is an angle below which no foams will flow Lespiat et al. [104]. This non-zero angle has also been observed in simulations of sheared frictionless particles, with the θ_R in different works ranging between $4° - 7°$ [105], $6.28°$ [117], $3.4°$ [118], $5.76° \pm 0.22°$ [103]. In the experimental work of Lespiat et al. [104] this angle was $4.6°$. These values contrasts with $\theta_R = 22°$ found for frictional granular materials [121]. θ_R is equivalent to μ_R and are linked to σ_y in the same manner as Equations (6.1.1) and (6.1.2).

In Chapter 8, we investigate if this macroscopic friction results in a foam with $\theta_R > 0$ using an experimental setup and comparing it to simulations.

Chapter 7

Couette Geometry Rheology

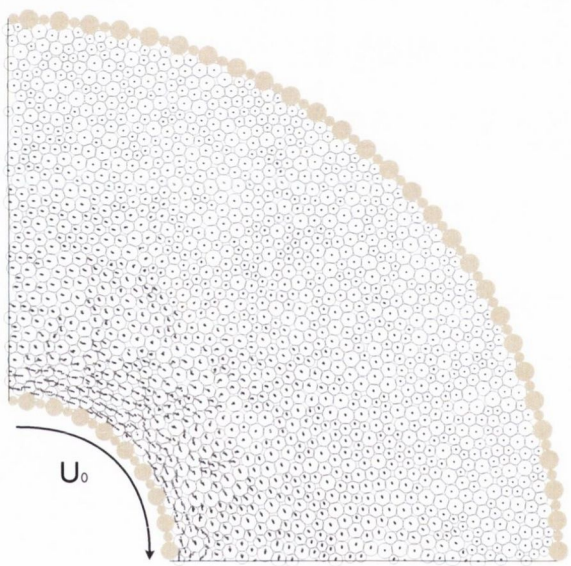

Figure 7.0.1: Image of Simulation Cell. The sample is periodic in the azimuthal direction with discs on the bottom interacting with discs on the left. The gold discs are fixed in the case of the outer wall at a radius R_o =84.99 $\langle R \rangle$, while the inner wall is situated at $R_i = 25\langle R \rangle$ and has an angular velocity of $U_0 = 25\langle R \rangle s^{-1}$. The white discs are free to move in the bulk. The trailing dots represent the disc trajectories.

7.1 Couette Cell Simulations

In this chapter we will examine the constitutive equation for foam in a circular geometry where the shear stress is inhomogenous and investigate whether recent proposed models of foam flow describe the flow of soft discs in this geometry.

7.1.1 Simulation Setup

Using the same simulation code as described in Section 2.2.1, we simulate the flow of wet foams using soft discs in a Couette geometry with periodic boundary conditions; an example is shown in Figure 7.0.1. For this work two densities are studied: $\phi = 0.95$ and $\phi = 0.90$. We generate assemblies of 1417–1500 discs (depending on ϕ) in a periodic cell with two concentric boundaries.

The outer boundary is moved inwards, compressing the soft discs until the desired packing fraction ϕ is reached, then the outer wall is held fixed at a radial distance $R_o = 84.99\langle R\rangle$. The inner boundary is kept at a fixed radial distance $R_i = 25\langle R\rangle$ and when the desired packing fraction ϕ is reached, the inner wall is set moving at velocity U_0, always in a clockwise direction. Other than the compression of the outer wall and then the clockwise shearing of the inner wall no other energy is put into the simulation to anneal the sample. We use polydisperse discs with a uniform distribution and a range of $R = \langle R\rangle(1\pm0.15)$ to prevent crystallisation. The boundaries are composed of discs that are held fixed with a bidisperse radius distribution. While this is a similar geometry to that used by Cheddadi et al. [122] many of the details of these simulations are different.

The sample is typically sheared for $10s - 40s$ depending on the driving velocity, with a time-step of $2.5 \times 10^{-7}s$. After a transient, the shear stresses on the boundaries reach a steady state. The duration of the transient is estimated as $1/\dot{\gamma}(r_y)$, where $\dot{\gamma}(r_y)$ is the strain rate at the radius where the stress

is equal to the yield stress. Once this condition is met we start measuring the velocity profile of the flow. The averaged angular velocity profiles U_θ are plotted in Figure 7.1.1.

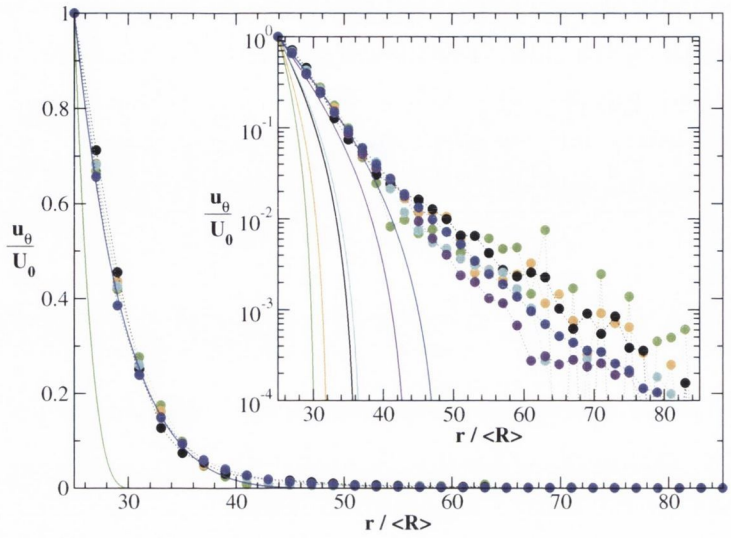

Figure 7.1.1: Normalised angular velocity profiles u_θ of sheared soft disc packings for inner wall driving velocities U_0: (•) 200 $\langle R \rangle s^{-1}$; (•) 100 $\langle R \rangle s^{-1}$; (•) 25 $\langle R \rangle s^{-1}$; (•) 20 $\langle R \rangle s^{-1}$; (•) 5 $\langle R \rangle s^{-1}$; (•) 2 $\langle R \rangle s^{-1}$. Inset are the same profiles but with a logarithmic y-axis. The solid lines are fits from Equation (6.2.5).

7.1.2 Simulation Results

The exponential velocity profiles seen in Figure 7.1.1 are similar to the rapidly decaying velocity profiles found in granular flows and the experimental results conducted in [123] for the flow of 2D foams trapped between two glass plates. Assuming that a continuum description applies and by measuring the shear stress at the inner boundary σ_i, the local stress $\sigma(r)$ can then be found from Equation (6.2.2). Comparing the local stress $\sigma(r)$ for the outer wall calculated from Equation (6.2.2) and measuring the shear stress at the outer boundary confirms that Equation (6.2.2) applies in these simulations. The Herschel–Bulkley model predicts that the velocity should go to zero when $\sigma(r) = \sigma_y$. It is shown in the inset of Figure 7.1.1 that there is clearly flow

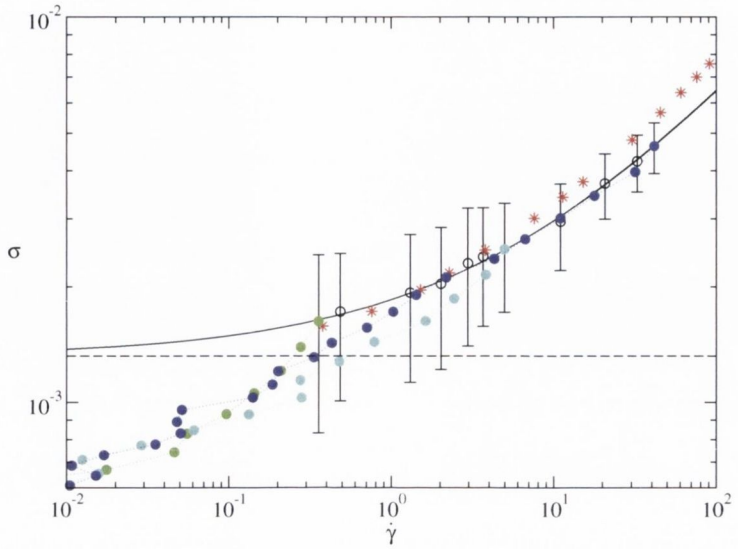

Figure 7.1.2: Stress versus strain rate curve for soft disc simulations. The solid line is the Herschel–Bulkley equation (Equation (6.1.1)) fit to shear stress data measured at and shear strain rate calculated at the inner wall for different driving velocities. Data labeled ($*$) are for a linear geometry with the simulation parameters unchanged [49]. The dashed black line indicates the yield stress. The driving velocities for the Couette cell are labeled the same as in Figure 7.1.1.

throughout the width of the cell and flow below the yield stress σ_y calculated for the bulk, which is found from fitting Equation (6.1.1) to data measured at the inner wall. This flow below the bulk yield stress violates the Herschel–Bulkley model. The angular velocity profiles U_θ are rate independent, which is inconsistent with the Herschel–Bulkley prediction of the velocity profiles as shown in Figure 7.1.1. This reproduces the experimental results of Katgert et al. [111] where rate independence and flow below the yield stress was observed.

Similarly the local strain rate $\dot{\gamma}$, which is a function of radius and angular velocity, can be calculated from the angular velocity profiles using Equation

(6.2.3). The data points plotted in Figure 7.1.2 correspond to the velocity profiles in Figure 7.1.1. The data plotted furthest to the right for the local curves are the points on the inner wall. As the data points move progressively left they correspond to the positions and velocities of the points in Figure 7.1.1 that move towards the outer boundary. Data for stresses below the bulk yield stress σ_y in Figure 7.1.2 correspond to particles that can clearly be shown to be flowing in Figure 7.1.1. The two quantities are compared to the Herschel–Bulkley relation in the linear geometry and plotted in Figure 7.1.2. The simulation results show a similar behaviour to that seen in experiment (see Figure 6.2.2). The local stress-strain rate curves for each driving velocity U_0 do not collapse onto the stress-strain rate data of the linear geometry, as would be expected from the Herschel–Bulkley equation. This confirms the flow in the Couette geometry is different to that in the linear geometry. Also, the local rheology curves do not collapse onto a single curve, suggesting a non-local relation.

The flow below the bulk yield stress is displayed in a series of snapshots of the simulation in Figure 7.1.3. From these images it can be seen that inside the line marking r_y, the radial yield distance under the Herschel–Bulkley interpretation, discs become mixed quickly, indicating flow from their initial positions. Outside r_y various coloured radial bands become ruptured due to the shear induced rearrangements caused by the moving inner wall. Certain locations are marked by a circle highlighting an irreversible rearrangement, clearly showing that there is flow below the bulk yield stress. The irreversible plastic rearrangements shown in Figure 7.1.3 are defined by a sustained switching of neighbours by a particle. Figure 7.1.3 reveals that the further from the moving inner wall, the longer it takes for a rearrangement to occur, confirming the profiles shown in Figure 7.1.1.

7.1.3 Comparison with Herschel–Bulkley

Using Equation (6.2.5) we are able to calculate the velocity profile as predicted by the Herschel–Bulkley theory and compare it to the results of the soft disc simulations. The velocity profile is found by numerically solving Equation (6.2.5) using a shooting method in the MATHEMATICA function NDSOLVE [124]. The comparison is plotted in Figure 7.1.1 and for the majority of driving velocities the Herschel–Bulkley prediction underestimates the velocity profile found in simulation. The velocity profiles calculated from a numerical solution of Equation (6.2.5) do not describe the velocity profiles of the simulations over the range of ω we considered. Fitting Equation (6.1.1) to the shear stresses measured at the inner wall as shown in Figure 7.1.2 gives an exponent of $\beta = 0.49 \pm 0.3$ consistent with experimental values [47] and other soft disc simulations [49].

From Figure 7.1.1 and Figure 7.1.2 we see that the Herschel–Bulkley model describes neither the velocity profiles nor the stress-strain rate relationship in this geometry. However the σ-$\dot{\gamma}$ measurements made at the inner wall are consistent with those found in a linear geometry in both simulation and experiment. The Herschel–Bulkley equation is an empirical formula that has been used to describe flow in visco-elastic materials like foams and emulsions. Though it has been quite successful in describing the flow characteristics in these materials as well as soft disc simulations, there has been no all encompassing microscopic description of why it has been successful. In Section 7.1.4, we will apply another empirical model that accounts for the aspects of flow in foams and soft disc simulations that the Herschel–Bulkley model fails to describe in this geometry.

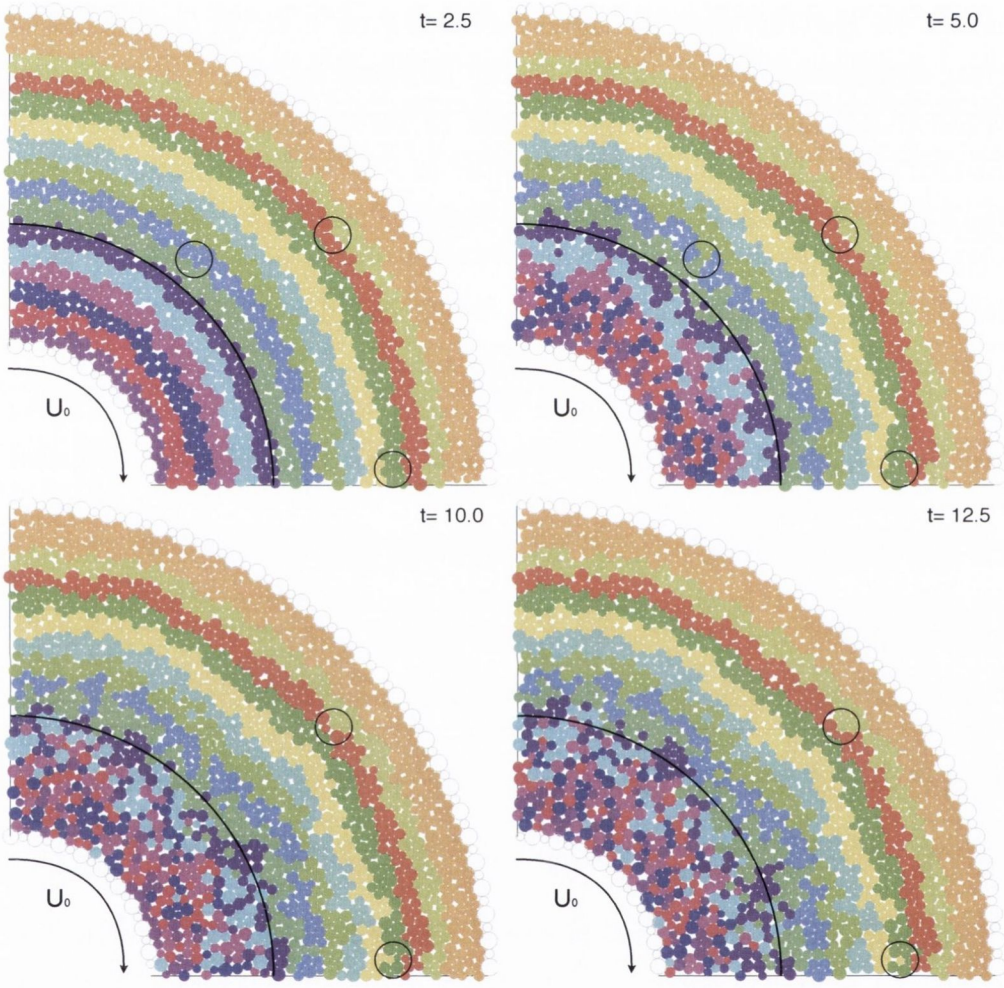

Figure 7.1.3: Plastic rearrangements beyond yield stress. Four snapshots of a simulation of a soft disc packing under shear. The radial sections are coloured differently to show their initial positions and show the movement of the foam. The circles mark positions where plastic rearrangements occur between different coloured discs.

7.1.4 Fluidity Model

To account for the discrepancy found between the Herschel–Bulkley theory and the velocity profiles found in simulation, we implement a fluidity model for non-local flow that has recently been proposed for emulsion flow in confined channels [115, 125]. The fluidity predicted for the system can be found be converting Equation (6.2.8) to polar coordinates

$$f_b(r) - f(r) + \xi^2 \left(\frac{\partial^2 f}{\partial r^2} + \frac{f(r)}{r} \right) = 0. \tag{7.1.1}$$

The boundary conditions for such a system are chosen so that at the inner boundary the fluidity is the same as the bulk fluidity given by Equation (6.2.7) and at the outer boundary, since the outer boundary is held fixed there can be no flow and hence the fluidity must go to zero [126]. An alternative

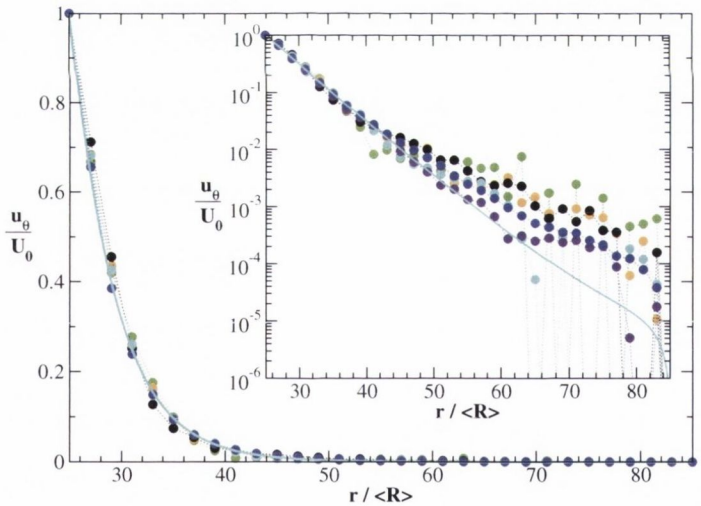

Figure 7.1.4: Comparison of fluidity model velocity profiles with simulation velocity profiles plotted in Figure 7.1.1. Inset are the same profiles with a logarithmic y-axis. The solid line is Equation (7.1.2) fitted to the data $U_0 = 25\langle R \rangle s^{-1}$ with $\xi = 5.9\langle R \rangle$.

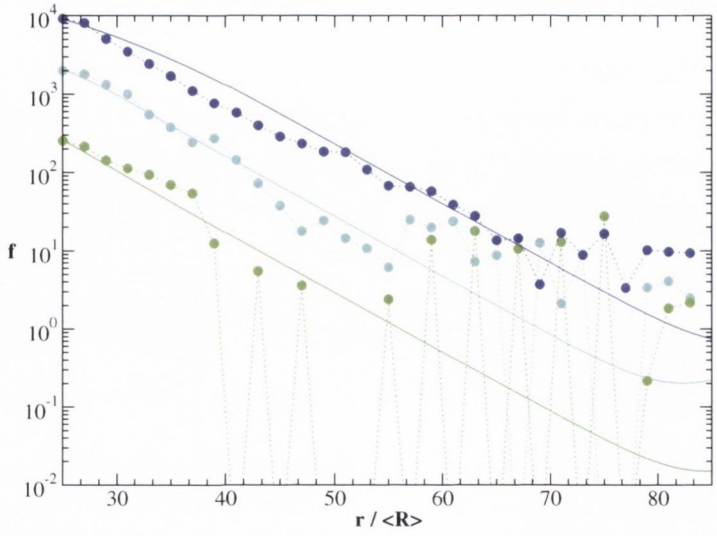

Figure 7.1.5: Fluidity profile from sheared soft disc packings with U_0: (•) 200 $\langle R \rangle s^{-1}$; (•) 25 $\langle R \rangle s^{-1}$; (•) 2 $\langle R \rangle s^{-1}$. The solid lines are the solutions of the fluidity from Equation (7.1.1) with $\xi = 5.9 \langle R \rangle$.

to the condition that the material flows as bulk at the inner wall has been proposed in [113] for 2D confined Poiseuille flow, where the wall fluidity is taken as $1.6 f_b$. However, as seen in Figure 7.1.2, the highest U_0 simulation behaves as bulk flow for some particle diameters into the channel. Equation (7.1.1) is numerically solved using MATHEMATICA routine NDSOLVE [124] to determine f.

A velocity profile from the fluidity model that describes non-local flow can then be found by substituting Equation (6.2.6) into Equation (6.2.1) giving

$$\left(\frac{\partial}{\partial r} + \frac{2}{r}\right)\left(\frac{\dot{\gamma}}{f}\right) = 0,$$

then substituting in from Equation (6.2.3) gives

$$\left(\frac{\mathrm{d}}{\mathrm{d}r}+\frac{2}{r}\right)\left(\frac{u_\theta}{rf}-\frac{\frac{\mathrm{d}u_\theta}{\mathrm{d}r}}{f}\right)=0.$$

Differentiating and simplifying leaves the angular velocity given as

$$\frac{\mathrm{d}^2u_\theta}{\mathrm{d}r^2}=\left(1-\frac{r\dot{f}}{f}\right)\left(\frac{u_\theta}{r^2}-\frac{\frac{\mathrm{d}u_\theta}{\mathrm{d}r}}{r}\right), \tag{7.1.2}$$

which can be solved numerically for a velocity profile. A choice for the parameter ξ is then made by comparison of Equation (7.1.2) with simulation data. This comparison is plotted in Figure 7.1.4 with good agreement between theory and simulation.

The fluidity of the simulation can be compared with the predicted fluidity from Equation (7.1.1). The fluidity is calculated by inserting the calculated values of local strain rate $\dot{\gamma}$ from Equation (6.2.3) and local shear stress σ from Equation (6.2.1) into the definition of fluidity Equation (6.2.6). Making the same choice of non-locality length ξ for all U_0, the comparison between theory and experiment is shown in Figure 7.1.5.

For values of r where the strain γ is significant and the velocity profile is not affected by noise there is good agreement between the predicted fluidity and that found in simulation. At large r the velocity profiles become less well defined, and hence the fluidity profiles becomes noisier. It is expected that by running simulations for a longer period of time the tails of these velocity profiles will become more stable. However for simulations with low rotation rate and therefore low shear rates, the time to reach a steady profile in the tail of the velocity profile is significant. Figure 7.1.5 also shows that for large r, the value of f is low and therefore the propensity for non-local rearrangements (irreversible plastic rearrangements that have been induced by flow in another region of the cell) to occur is slight. The tail of the f simulation data is noisy as few rearrangements occur in this region over the

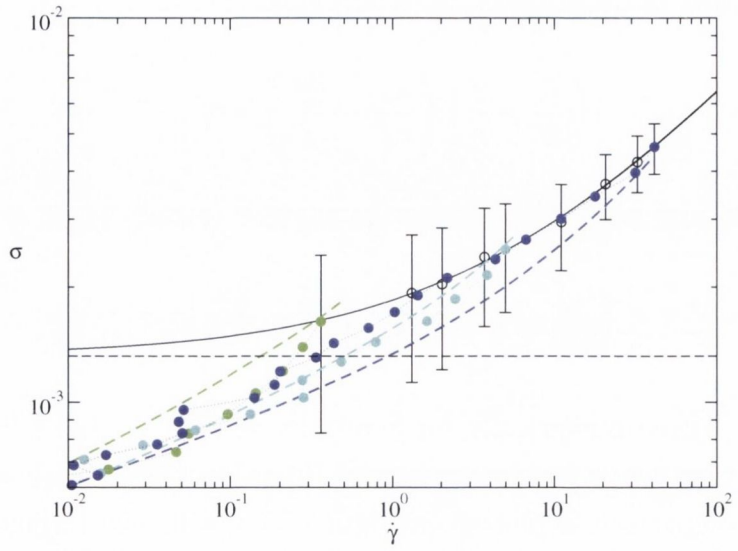

Figure 7.1.6: Comparison of the rheological curves plotted in Figure 7.1.2 with predictions made from the fluidity model (dashed lines). The data is labeled the same as in Figure 7.1.5.

timescale of the simulation. The data shown for low r in Figure 7.1.5 is indicative of agreement with the model.

Given that the velocity profiles are better fit by the fluidity theory than the Herschel–Bulkley theory, f is used to find the rheological model behaviour of the rheology of the soft disc simulations by calculating the stress and strain as predicted by the solution of Equations (7.1.1) and (7.1.2) and plotted in Figure 7.1.6. There is good agreement between theory and the simulation data. The fluidity prediction is particularly robust below the Herschel–Bulkley predicted yield stress of the bulk. The same $\xi = 5.9\langle R \rangle$ was used in all 3 predictions. The results shown in Figure 7.1.6 compare well with the experimental predictions of Katgert et al. [111].

Up to this point all data that has been presented is for $\phi = 0.95$; in Figure 7.1.7(a) and (b) simulation data with $\phi = 0.90$ is compared with the

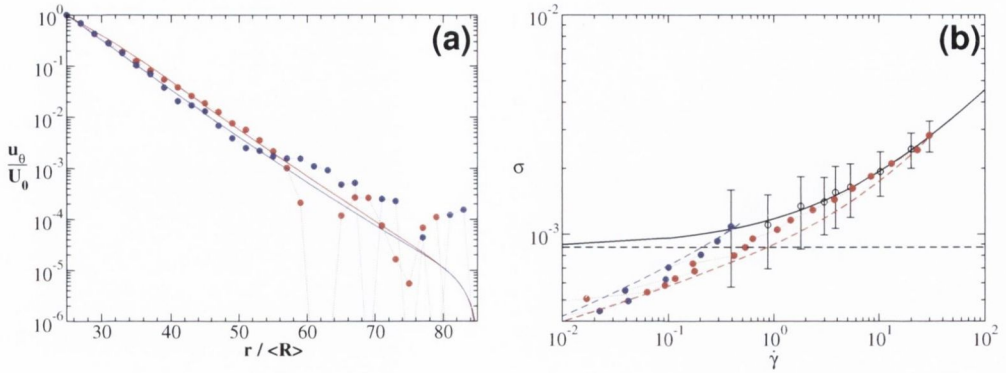

Figure 7.1.7: Flow properties at $\phi = 0.90$. (a) Angular velocity profile for driving velocities U_0: (•) $150\langle R\rangle s^{-1}$; (•) $2\langle R\rangle s^{-1}$. The solid lines are fits to Equation (6.2.8). (b) Stress versus strain rate curve. Data marked as (○) is measured on the inner wall, the solid line is this data fit by Equation (6.1.1). The horizontal dashed line is the yield stress. The coloured dashed lines are predictions of the fluidity model with $\xi = 5.9\langle R\rangle$.

fluidity model. The velocity profile is well described by the fluidity model in Figure 7.1.7(a) and the shear stress versus strain-rate relation in Figure 7.1.7(b) is also in good agreement with the fluidity model. The Herschel–Bulkley equation fitted to the data in Figure 7.1.7(b) shows an increase in the exponent $\beta = 0.54 \pm 0.05$ and decrease in the yield stress relative to $\phi = 0.95$ data. For both comparisons the cooperativity length is kept the same as before with $\xi = 5.9\langle R\rangle$.

The choice of this cooperativity length is justified by Figure 7.1.8, where ξ is largely unaffected by the change in $\phi = 0.95$ to $\phi = 0.90$ with the average of $\xi = 5.9 \pm 0.3\langle R\rangle$. This value of ξ is consistent with other values found in 2D simulations [113] and experiment [111, 115]. Though ξ is approximately constant there is a trend towards lower ξ for increasing driving velocity. The reason we think that ξ drops with ω is because of the timescales involved in inducing a non-local rearrangement. As the material is sheared faster the deformation timescale becomes smaller than the time it takes a rearrange-

ment to trigger another rearrangement further away in another part of the flow and hence ξ decreases. In 3D emulsion experiments [115], it was found that $\xi \to 0$ as the density of the material gets closer to ϕ_c. It is unclear from our results, for the small range of ϕ considered here, whether this trend in ξ is more likely than ξ remaining constant.

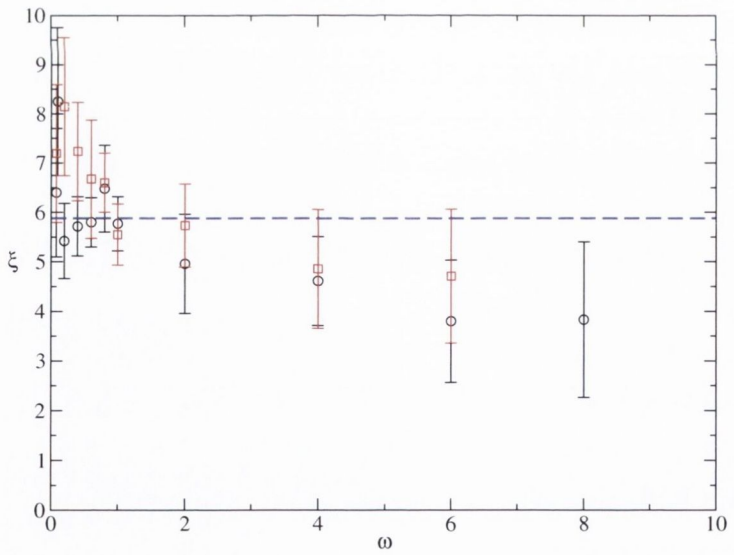

Figure 7.1.8: Variation of cooperativity length ξ with driving velocity and ϕ. Data for two packing fractions are plotted: ($\circ$) $\phi = 0.95$ and ($\square$) $\phi = 0.90$. The dashed blue line is the average of the data, $\xi = 5.9 \pm 0.3\langle R \rangle$.

7.2 Conclusions & Outlook

With soft disc simulations we have reproduced the results of the experiments conducted by Katgert et al. [111] in a Couette geometry. The flow of the soft discs is shown to be independent of driving velocity U_0 and we observe flow below the Herschel–Bulkley predicted yield stress σ_y of the bulk. We find that the rheological curve for this geometry differs from that of a linearly sheared foam. In addition, we have shown in Figure 7.1.2 that the local rheology curves do not collapse onto a single rheology curve, indicating that the rheology is non-local.

We find that the fluidity model proposed by Goyon et al. [115] is in good agreement with the simulation results presented here. The fitting parameter of the cooperativity length ξ is in good agreement with these works and the simulations of Mansard et al. [113]. The influence of packing fraction appears to be slight and the variation of ξ is much greater with driving velocity than with ϕ. The apparent independence of ξ from ϕ is in contrast to the results of 3D emulsions [115, 125], but confirms the results of 2D simulations [113].

The main topic of future work should be to extract ξ independently from the particle trajectories. A outline of the scheme is to study the spatial correlation function of rearrangements and measuring the size of transient swirls that appear in the flow [49, 45].

It would appear that consensus has not been reached on the role of boundary conditions in the investigation of non-local effects. The influence of the boundary is highlighted in [113], which selects a boundary condition for the fluidity that is greater than the bulk fluidity in contrast to other 2D work [111, 126]. There is still much work to be done on the influence of surface roughness and system size on non-local flow. To this end we are in the process of adapting the simulation procedure, so that simulation can be run in the CUDA environment on GPU. The length of time a simulation takes is often the limiting factor in this research. With the current simulation procedure, in order to strain the simulations sufficiently to produce a stable

velocity profile, some of the simulations with a low U_0 can take longer than a month of computation time to complete. A GPU simulation procedure will enhance the speed of simulation allowing a greater examination of the parameters that affect non-locality and allow the investigation of larger system sizes.

It has been shown in experiment that when the gap between the confining walls becomes large, the Herschel–Bulkley description of the rheology becomes appropriate again [127]. It would of interest to steadily increase the size of the system and identify the point at which the fluidity model and Herschel–Bulkley model become indistinguishable from each other.

The apparent different behaviour of ξ as a function of ϕ in 2D and 3D begs further investigation. First of which requires an investigation of non-local effects at much higher and much lower ϕ to better establish its behaviour. It would perhaps be a focus of the enhanced simulation procedure to modify soft disc rheology simulations to that of soft spheres in 3D and investigate the behaviour of ξ. The investigation of 3D foams looks to be a particularly bountiful area of future work with recent developments in experiments with x-ray tomography on foams producing results on the rheology of foams [128].

Chapter 8

Rotating Drum

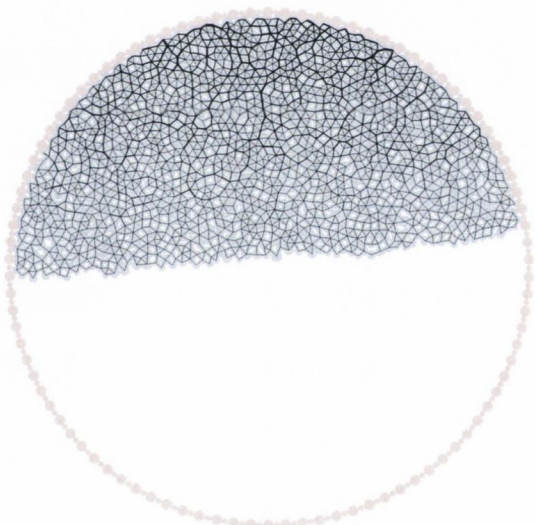

Figure 8.0.1: Image of Simulation Cell. The pink circles are fixed and the blue circles are free to move. There is a buoyancy force acting towards the top of the drum. The blue discs in contact are joined by a line with a width that is proportional to the elastic repulsion between the discs.

8.1 Introduction to Rotating Drum

In contrast to solid grains, bubbles have no static friction. This makes the study of foams in the context of packing and rheology an interesting prospect because it removes an additional variable from the widely studied area of granular media [129]. In this chapter we study some of the phenomena that have previously been investigated for granular materials.

We study macroscopic friction as an emergent property of a collection of frictionless particles and whether it leads to a non-zero static angle of repose. In addition to this, we will investigate shear dilatancy in two dimensional foams and compare the shear dilatancy found in experiment with results from 2D simulations. Finally, we will comment on attempts to measure the angle at which foam starts to flow.

We study these effects through simulation and experiment of a rotating drum setup. The rotating drum experiment, already extensively used in granular media (see [130] and references therein), is adapted for foams (Figure 8.2.1). The experimental portion of this chapter is based upon work conducted by Poulichet et al. [131, 132]. The majority of the experimental work presented in this chapter was conducted by Poulichet in tandem with the simulations which were conducted by me. This work is compared to soft disc simulations of the rotating drum setup. Using simulations and experiments we study a variety of parameters that affect the angle of repose and shear dilatancy of foams.

8.2 Comparison with Experiment

8.2.1 Experimental Setup

To investigate foam properties such as the static angle of repose or dilatancy in the rotating drum setup (Figure 8.2.1), the foam must be brought to a perturbed state and allowed to relax freely to a mechanical equilibrium. It is possible to do so by applying a shear stress by rotating a top plate with angular velocity ω for a certain amount of time and then cease it abruptly. The main features of the apparatus used are:

- The circular drum (radius R=30mm) equipped with a rough edge formed by teeth of about 2mm wide and 1mm deep, as sketched in Figure 8.2.2. This ensures a non-slip boundary condition on the rim of the drum.

- The surfactant solution is prepared with tap water and 1% concentration (by volume) of commercial detergent (Fairy Liquid).

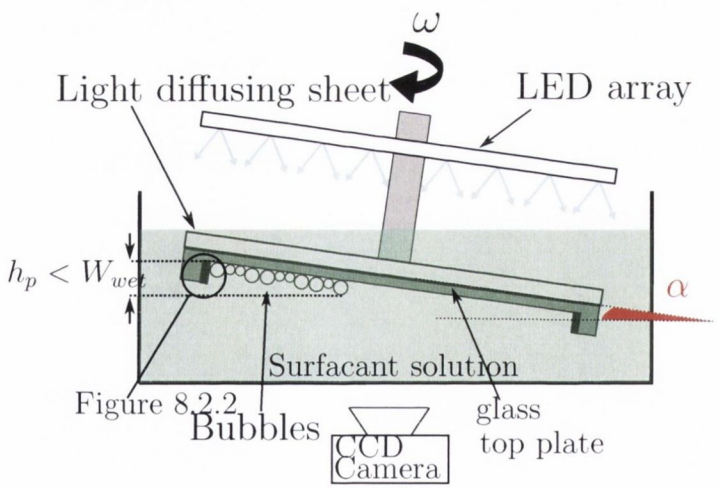

Figure 8.2.1: Side view sketch of the rotating drum apparatus.

- Bubbles are trapped under a top-plate made of glass. The entire setup is levelled by three screwable feet. The level is regularly checked to ensure the consistency of the measurements.

- The drum is filled with bubbles to a filling height of 1/3 of the drum. Customarily in granular experiments the drum is half filled [130] but due to the presence of a driving shaft that interferes with the image analysis (as visible in Figure 8.2.3), we cannot fill the drum to halfway.

- The drum is attached to a shaft that can be rotated on its axis at the angular velocity ω with a stepper motor. Another stepper motor allows us to rotate the axis of the system and tilt the plane of the drum about an angle α with respect to the horizontal. Both α and ω are computer controlled. α must be lower than 7° ($h_p < 2.56mm$ on Figure 8.2.1) to ensure that the foam is in the wet limit W_{wet}. The foam remains wet within a width W_{wet} above the foam/liquid interface where liquid drainage due to gravity is prevented by capillary forces. This wet region is estimated as:

$$W_{wet} = \frac{{l_0}^2}{2\langle R \rangle}, \tag{8.2.1}$$

where $\langle R \rangle$ is the mean radius of the bubbles and l_0 is the capillary length. The capillary length is defined as $l_0 = \sqrt{\frac{\gamma_s}{\rho g}}$ with ρ the density of the fluid, g the gravity constant and γ_s is the surface tension [129].

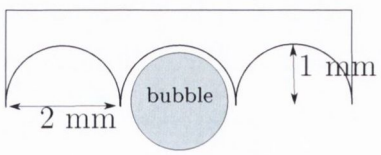

Figure 8.2.2: Drawing of the teeth on the rim of the drum.

- Light-emitting diode (LED) arrays together with a light diffusing sheet ensure that the system's backlight is smooth and uniform. Such a condition is essential for image processing.

- A camera takes snapshots of the drum and is connected to a computer to collect the data. The maximum frame rate of the camera is 25 frame per second, and its resolution is 1280×1024 pixels. The camera is configured so that we get an experimental resolution of about 10 $pixels/mm$.

The different samples created have monodisperse, bidisperse and polydisperse radius distributions. The gas used is air. The maximum duration of an experiment is set to three hours after which the effects of coarsening on the bubbles are no longer negligible.

As mention in Part I of this thesis, foams can crystallise for small values of polydispersity (Figure 8.2.3). In order to avoid crystallisation in bidisperse samples, the introduction of *big* ($r_b = (0.99 \pm 0.03)mm$) and *small* ($r_s = (0.63 \pm 0.03)mm$) bubbles were alternated at least four times during the preparation of one sample. The radii of the bubbles are obtained using the image processing software ImageJ [133]: The area of the bubble is measured (by plotting a circle over it), then the radius is deduced from this area.

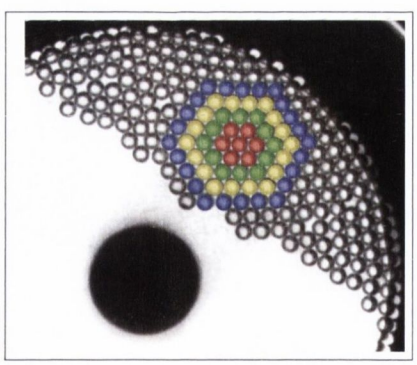

Figure 8.2.3: Example of crystallisation in a monodisperse foam.

8.2.2 Experimental Method

A simple vector diagram (Figure 8.2.4) is useful to visualise the forces applied on the system. The component of the buoyancy parallel to the confining plate ($\vec{F}_B$ in Figure 8.2.4) is the effective force applied on the bubble pile and is written:

$$F_B = \sin(\alpha)\, F_{total}, \tag{8.2.2}$$

where F_{total} is given as,

$$F_{total} = \frac{4\pi}{3}\langle R\rangle^3 \rho_{water} g, \tag{8.2.3}$$

and ρ_{water} is the density of water. From Equation (8.2.2), by changing the angle α the effective buoyancy force applied on the bubble pile is controlled.

Bubbles are introduced into the tilted drum, which is immersed in the surfactant solution to create a monolayer of foam. The system is sheared by rotating the drum for approximately two periods with a rotation rate $\omega = 2.58°s^{-1}$, then the rotation stops and the foam freely relaxes for ten minutes to ensure that the foam has reached mechanical equilibrium (see Figure 8.2.5 and Figure 8.2.6). In this relaxed state the yield stress of the

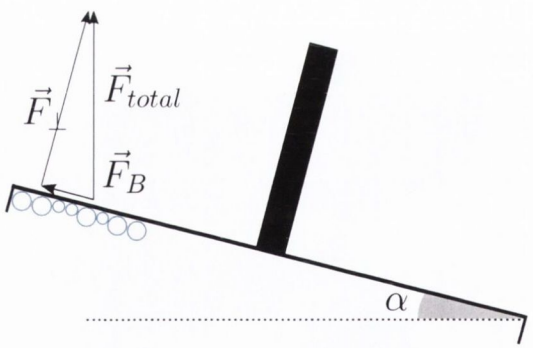

Figure 8.2.4: Simple vector diagram with the buoyancy force ($\vec{F}_{total}$) decomposed in its perpendicular ($\vec{F}_\perp$) and parallel ($\vec{F}_B$) components with respect to the plane of the drum.

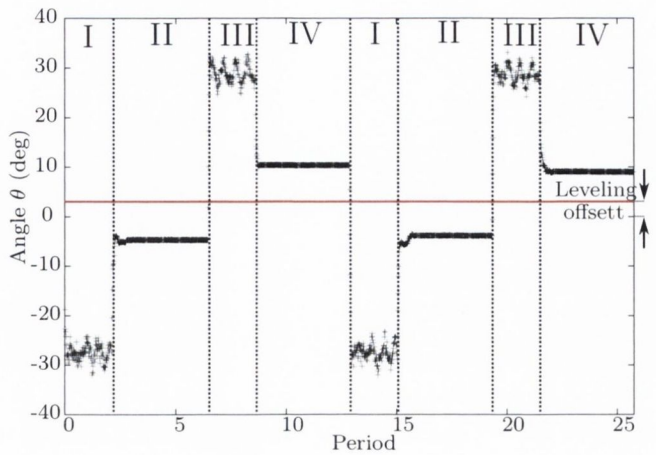

Figure 8.2.5: Change of the angle of the foam/liquid interface during the experiment. The drum completes a rotation in a period. The drum rotates subsequently clockwise and counter clockwise. The tilt angle is $\alpha = (3.5° \pm 1°)$, the rotation rate is $\omega = 2.58° s^{-1}$. The foam is composed of 2/3 *big* bubbles and 1/3 *small* bubbles. Note that the angles are constantly shifted by an angle of approximately two degrees. This offset is due to the imperfection of the levelling. Alternating rotation in both directions allows us to account for this offset see Equation (8.2.4).

foam appears to be homogenous and so the bubble pile forms a straight line across the drum.

The angle of repose should a static property and should not depend on the applied shear rate. This lack of dependence on the shear rate is verified by running experiments with two different shear rates (one low $\omega = 2.58\ °s^{-1}$ and one high $\omega = 6.71\ °s^{-1}$) where we obtain the same static angle of repose within error bars. Therefore, the static angle of repose does not depend on the history. Rotating the drum for five minutes ensures the that foam is well mixed to avoid crystal patches (Figure 8.2.3).

Latin numbers in Figures 8.2.5 and 8.2.6 correspond to stress and relaxation. This operation is carried out subsequently for a clockwise (Figure 8.2.6(a)) and a counter-clockwise (Figure 8.2.6(b)) rotation because of the

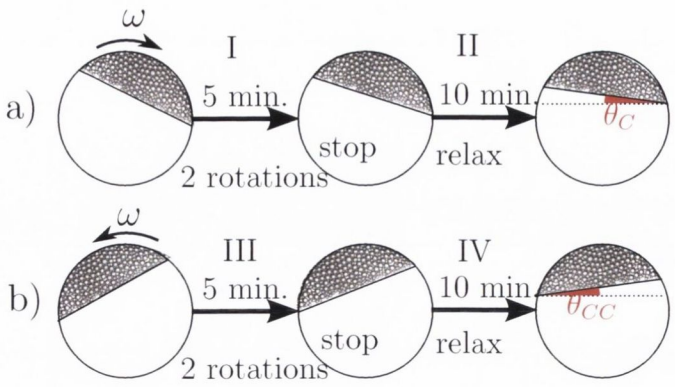

Figure 8.2.6: During the static angle of repose experiment, the procedures (a) and (b) are repeated subsequently.

imperfections of the levelling of the drum. After rotating in the clockwise direction the angle of repose θ_C is recorded. Similarly, after rotating in the counter-clockwise direction the angle of repose θ_{CC} is recorded. The imperfection in levelling the drum leads to an offset in the angle measurements (see Figure 8.2.5), this means that the two measured angles (θ_C and θ_{CC}) are not centred around 0. The angle that the interface of the foam makes with the horizontal is measured when the system is completely relaxed, *i.e.* when no more rearrangement occur within the bubble pile.

The systematic errors in measuring θ_R from the imperfect levelling of the drum can be accounted for when we rotate both clockwise and counter-clockwise. Therefore we can infer θ_R with the absolute values of θ_C and θ_{CC}:

$$\theta_R = \frac{|\theta_C| + |\theta_{CC}|}{2}. \tag{8.2.4}$$

The static angle of repose is measured six times during each experiment. The error is estimated by the standard deviation of these measurements.

Note that the small oscillations in Figure 8.2.5 occurring during rotations *I* and *III* are not intrinsic properties of the foam but is due to a wobble

caused by drum misalignment. This wobble is not problematic for static properties such as θ_R as it only affects the dynamics.

The camera takes an image every two seconds so there are about 6000 images for each run. An IDL (INTERACTIVE DATA LANGUAGE)[134] image processing code is used to measure the angles θ_C and θ_{CC} from the centre of mass of the bubble pile. These angles are measured only at the end of every ten minute rest period.

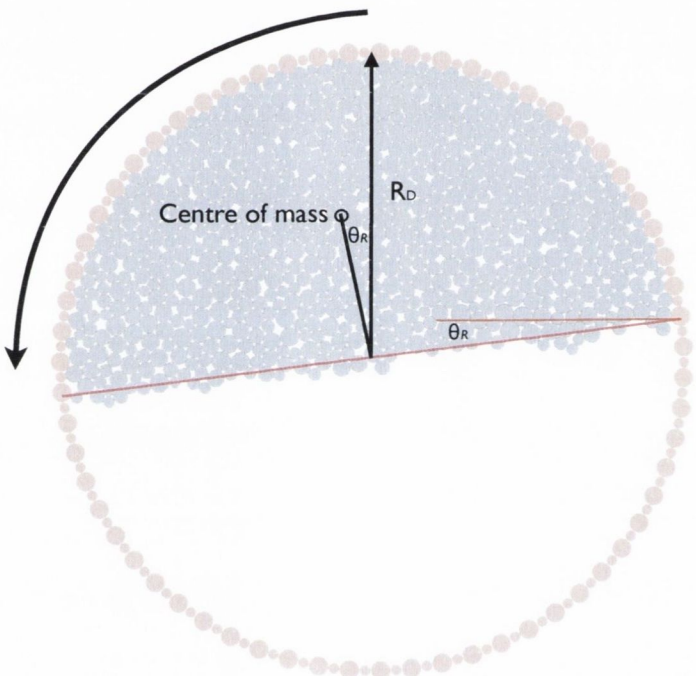

Figure 8.2.7: Diagram of rotating drum simulation geometry. The boundary discs which are coloured pink at the edge have their positions fixed though interact with the blue soft discs as normal. The blue discs are free to move throughout the drum. The boundary discs are rotated counter clockwise at angular velocity w for a period and then stopped.

8.2.3 Simulation Setup and Methods

Simulations of a rotating drum are performed using the soft disc code outlined in Section 2.2.1, where the coefficient of elasticity κ and the dissipation constant c_b are set such that the ratio of the viscous to inertial timescale $t_v/t_i = 0.0419$. While $t_i \gg t_v$ the dynamics are overdamped and the inertial effects are negligible. The geometry shown in Figure 8.2.7 is used for a variety of different drum sizes R_D. The discs on the boundary are held fixed in position and have a bidisperse radius distribution with the larger discs having a radius of $1.24\langle R\rangle$ and the smaller radius $0.76\langle R\rangle$ in order to impose a no slip condition. Inside the drum a number of discs are placed in a disordered lattice with a polydispersity that is either bidisperse (with a 50-50 mix of 1:1.4 radius), uniform or monodisperse. The number of discs placed inside the drum is such that typically half the drum is filled. In addition to the elastic repulsive force and the viscous drag force between discs, a buoyancy force F_B is included in this simulation which drives the discs to the top of the drum. Once the interior discs have settled, the boundary discs are rotated at an angular velocity ω for 8 seconds. The simulation time step is $5 \times 10^{-7}s$. After this period of rotation when the interior discs have been excited and mixed, the imposed shearing is stopped, the boundary discs are held stationary and the pile is allowed to relax. When the angle the centre of mass of the pile makes with the centre of the drum remains unchanged for 8 seconds, the simulation is terminated.

For large system sizes we have adapted the simulation procedure so that it can be executed in parallel on graphics processing units on the CUDA platform. This allows an exploration of very large system size in reasonable computation time.

The angle of repose θ_R is found by calculating the centre of mass of the packing after it has relaxed and measuring the angle that is made with the geometric centre of the drum. This angle is measured for a range of variables such as R_D, F_B, ω, polydispersity and different boundary conditions.

8.2.4 Comparison between Simulation and Experiment

There are a number of differences between simulation and experiment. Principle of which is the difference in the viscous drag. In experiment viscous drag between bubbles scales as $\Delta v^{2/3}$ while in simulation the viscous interaction is linear. Also, the experiment includes a glass top plate to confine the bubbles, adding another viscous interaction. However, in terms of finding θ_R, viscosity is not a factor as while it slows down the dynamics, it should not affect static properties.

In the static case two forces compete, repulsion between bubbles and the compressing force of buoyancy. To compare experiment and simulation, at least qualitatively, we set a dimensionless number (Bu) to represent the competition between the spring repulsion ($\kappa\langle R\rangle$) and the buoyancy on a single bubble (F_B):

$$Bu = \frac{F_B}{\kappa\langle R\rangle}. \tag{8.2.5}$$

The approximation of the spring constant for bubbles in experiment is $4\pi\gamma_s$ in the wet limit [5].

In experiment this buoyancy effect can be tuned by changing α (Equation (8.2.2)) in the experiment. However, it is not possible to set α larger than 7° in the experimental setup because the vertical height of the bubble pile must not exceed W_{wet}, so to avoid the effects of drainage. This would result in a foam with varying liquid fraction. It is difficult to set the angle of the top plate α lower than 2° and keep the bubble pile together during the rotation phase. This sets the limit on the range of values of buoyancy that can be explored in experiment. However, in the simulation, the effect of the buoyancy can be studied over a wider range. The effect that this ratio of buoyancy to repulsion is discussed in Section 8.3.3.

Another effect that is studied in simulation and experiment and then compared in Section 8.3.2 is the effect polydispersity has on the angle of repose. In experiment a bidisperse mixture was primarily used. The polydispersity

is controlled by changing the relative number of big and small bubbles. The average radius of the big bubbles R_b is $(0.99 \pm 0.03)mm$ and the average radius of the small bubbles R_s is $(0.63 \pm 0.03)mm$. By changing the ratio of the number of big bubbles N_b to the number of small bubbles Ns, a range of bidisperse mixtures from a monodisperse foam of big bubbles to a monodisperse foam of small bubbles can be investigated. For consistency, the filling depth of the foam in the drum is kept constant for every mixture. The number of bubbles in each sample can vary from 208 to 344 depending upon the composition of the mixture (See Table 8.1 below). In simulation the effect that polydispersity has on θ_R is investigated by looking at three different types of particle size distribution; bidisperse, uniform and monodisperse.

Another difference between experiment and simulation is the filling height of the drum, which will be reported on in Section 8.3.4. For the experiment the filling height is kept constant at one third filled but the number of bubbles in the drum can change by changing their average size. In simulation we vary the filling height of a drum with 285 bidisperse particles in it by using drum setups of different radii.

We then alter the size of the drum and the number of particles in the drum in simulation to explore the effect of the number of particles and system size has on θ_R. The drum is always half filled in these simulations.

In Section 8.3.5, using Equation (6.1.2) outlined in Chapter 6, we compare a value for the angle of repose that we extract from the Couette geometry simulations in Chapter 7 with the values we have found in the rotating drum simulations and experiments.

In Section 8.4, we investigate how rotation rate in simulation and experiment affects shear dilatancy. We then examine how this dilatancy is affected in simulation by changing parameters such the viscous drag coefficient c_b, the filling height of the drum and the number of particles in the drum.

Finally in Section 8.5, we discuss the angle at which flow begins in the bubble pile.

Exp No.	N	N_b/N	σ_R	Bu	α
E1	208	1.000	0.000	9.74×10^{-3}	$3.5° \pm 1°$
E2	220	0.845	0.140	8.66×10^{-3}	$3.5° \pm 1°$
E3	234	0.709	0.186	7.78×10^{-3}	$3.5° \pm 1°$
E3	234	0.709	0.186	7.78×10^{-3}	$3.5° \pm 1°$
E4A	253	0.549	0.218	6.79×10^{-3}	$3.5° \pm 1°$
E4A	253	0.549	0.218	6.79×10^{-3}	$3.5° \pm 1°$
E4B	253	0.549	0.218	3.88×10^{-3}	$2.0° \pm 1°$
E4C	253	0.549	0.218	10.7×10^{-3}	$5.5° \pm 1°$
E4D	253	0.549	0.218	12.6×10^{-3}	$6.5° \pm 1°$
E5	278	0.374	0.229	5.79×10^{-3}	$3.5° \pm 1°$
E5	278	0.374	0.229	5.79×10^{-3}	$3.5° \pm 1°$
E6	288	0.288	0.224	5.33×10^{-3}	$3.5° \pm 1°$
E6	288	0.288	0.224	5.33×10^{-3}	$3.5° \pm 1°$
E6	288	0.288	0.224	5.33×10^{-3}	$3.5° \pm 1°$
E7	298	0.232	0.214	5.03×10^{-3}	$3.5° \pm 1°$
E7	298	0.232	0.214	5.03×10^{-3}	$3.5° \pm 1°$
E8	317	0.132	0.181	4.54×10^{-3}	$3.5° \pm 1°$
E8	317	0.132	0.181	4.54×10^{-3}	$3.5° \pm 1°$
E9	344	0.000	0.000	3.92×10^{-3}	$3.5° \pm 1°$

Table 8.1: Table of experimental data

8.3 Static Angle of Repose

In this section we compare the results of the simulations and experiments to determine the static angle of repose. In both experiment and simulation we find a non-zero θ_R. We now present our results for how a variety of factors influence the value of θ_R.

8.3.1 Effect of Boundary Roughness

First we check how rough the boundary wall needs to be in order to not affect the value of θ_R. Using a simulation of a drum with $D_R = 26\langle R\rangle$ filled with 285 bidisperse discs that has already been brought to the perturbed state by rotation, the geometry of the boundary is changed. The discs on the boundary are changed so that the boundary becomes composed of monodisperse discs of a given radius. The simulation is then allowed to relax. The smaller the radius, the more discs that are on the boundary. With smaller discs and less size difference between boundary discs there are less gaps for the discs

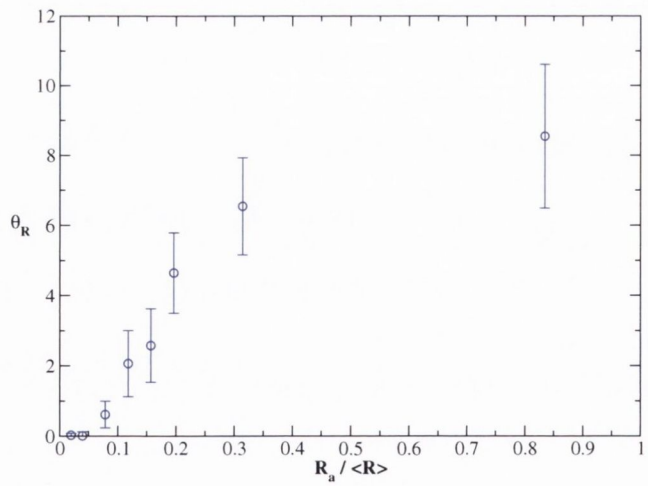

Figure 8.3.1: Angle of repose versus surface roughness of the boundary.

within the drum to form a stable template for a structure to create a non-zero θ_R.

As shown in Figure 8.3.1, θ_R has a dependence on the surface roughness of the boundary. The surface roughness R_a is defined as,

$$R_a = \frac{1}{2\pi R_D} \int_{-\pi}^{\pi} |y(\psi)| R_D \mathrm{d}\psi, \tag{8.3.1}$$

where $y(\psi)$ describes the surface of the boundary [135]. It must be emphasised that this surface roughness dependence is due to the packing relaxing into its lowest energetic state obtainable and not related to the shearing state, which is performed with a bidisperse boundary to allow for slip-free shearing. This simulation only investigates by how much the packing relaxes from its excited state. As the boundary becomes smoother, θ_R decreases and for very small boundary discs, $\theta_R \to 0$. The furthest point on the right of Figure 8.3.1 is the bidisperse boundary used in all other simulations.

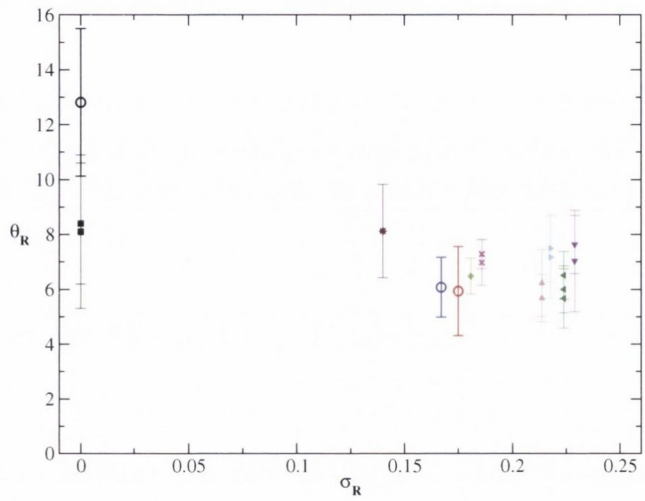

Figure 8.3.2: The static angle of repose with changing polydispersity. The filled symbols represent experimental data. This experimental data has a key that is recorded in Table 8.1. (■) E1,E9; (∗) E2; (♦) E8; (×) E3; (▲) E7; (►) E4A; (◄) E6; (▲) E5. The simulation data is represented as (○) monodisperse; (○) bidisperse; (○) uniform.

8.3.2 Effect of Polydispersity

In Figure 8.3.2 we compare the effect that polydispersity has on θ_R in simulation and experiment. In simulation the bidisperse mixture is a 50-50 mix of soft discs with radius either $1.17\langle R\rangle$ or $0.83\langle R\rangle$ where $\langle R\rangle = 10^{-4}$. The uniform size distribution includes discs that have a radius which range from $0.85\langle R\rangle$ to $1.15\langle R\rangle$. Monodisperse simulations have a single radius of $\langle R\rangle$. The simulated drum with $R_D = 26\langle R\rangle$ is half filled with $N = 285$ discs. Typically the simulation is repeated at least 8 times with a different configuration of initial particle positions for each set of parameters.

In experiment a bidisperse mixture was primarily used. The polydispersity is controlled by changing the relative number of big and small bubbles as shown previously in Table 8.1.

The data plotted in Figure 8.3.2 contain a similar number of particles in

both simulation and experiment. Similarly, Bu is equivalent for all systems shown here. There is no apparent relation between the polydispersity and the static angle of repose with only a slight increase for less polydisperse samples. One may remark that for the case of monodisperse foams the static angle of repose is slightly higher than for polydisperse foams. This is attributed to be the consequence of crystallisation within the bubble pile as depicted in Figure 8.2.3. This effect is more pronounced in simulations of monodisperse packings which form piles with large θ_R. This discrepancy between simulation and experiment may be due to the absence of small vibrations from the environment in simulation which assist the packing in overcome potential barriers and finding a lower energy state or that in experiment bubbles may not be exactly monodisperse. Our interest in this work is disordered packing so simulation results for monodisperse soft discs are omitted from the discussion of other aspects of this research.

8.3.3 Effect of Buoyancy

Another parameter that requires investigation is Bu, which represents the competition between buoyancy force and bubble repulsion. How does θ_R change with the buoyancy force? The change of the static angle of repose with the dimensionless number $Bu = F_B/\kappa\langle r\rangle$ is plotted in Figure 8.3.3.

Figure 8.3.3 suggests that the angle of repose does not change with α significantly in experiment but in simulation over a wider range of values of Bu there is a decrease in the values of θ_R. In general the results of the experiment agree with those of the simulation.

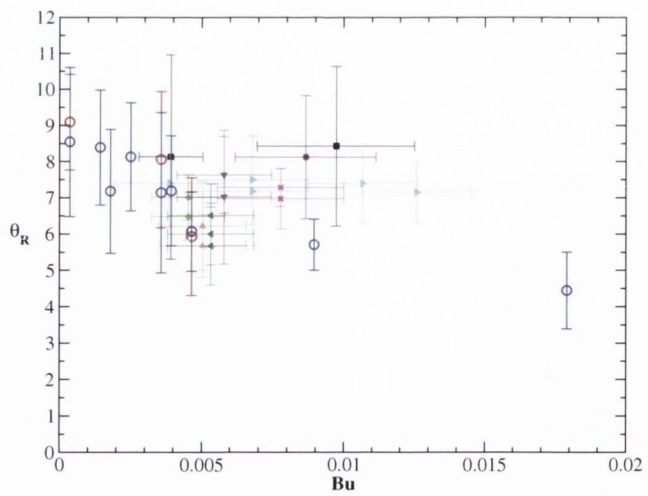

Figure 8.3.3: The effect on the static angle of repose due to buoyancy. Data are labeled the same as in Figure 8.3.2 except that (▶) represents E4A, E4B, E4C and E4D.

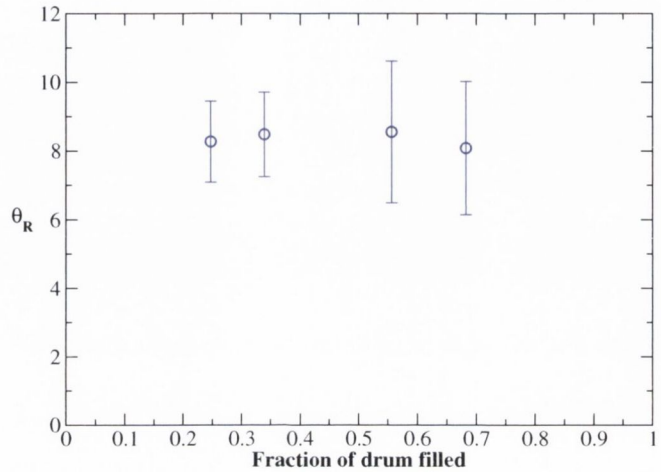

Figure 8.3.4: Plot of simulation results of the static angle of repose versus the fraction of the drum filled for $N = 285$ bidisperse discs with $Bu = 3.55 \times 10^{-4}$.

8.3.4 Effect of System Size

We will now address the question of whether the static angle of repose changes with system sizes. Dependence of the angle of repose on system size has previously been observed in experiments of chute flow of 3D foam where the system size is the height of the foam [104]. The first aspect to be addressed is whether the discrepancy between the amount of the drum filled in experiment, where it is only 1/3 filled versus the simulation procedure where the drum is 1/2 filled. In experiment it is not possible to fill more than a third of the drum due to the driving shaft of the drum (which can be seen in Figure 8.2.3) which interferes with the imaging of the bubbles.

To test whether there is a dependence on filling depth, simulations of bidisperse discs with $N = 285$ were conducted for $R_D = 23\langle R\rangle$, $26\langle R\rangle$, $36\langle R\rangle$, $45\langle R\rangle$. As can be seen in Figure 8.3.4, there is no variation in θ_R with changing filling depth and therefore the variation in the size of the system is

investigated in terms of the number of particles N.

In Figure 8.3.5 the data for simulation results with varying number of particles N. The filling fraction and dimensionless number Bu are kept constant. Simulations show that the angle of repose decreases with increasing system size. The trend for both bidisperse and uniform radius distributions are similar, with θ_R tending to be slightly larger for the uniform distribution. As N gets large, θ_R tends towards a constant. Following the treatment Peyneau and Roux [103] used in studying the effects of finite size on macroscopic friction, we plot in the inset of Figure 8.3.5 the dependence of θ_R as a function of $N^{-1/2}$, which appears to be linear. An empirical equation is fit

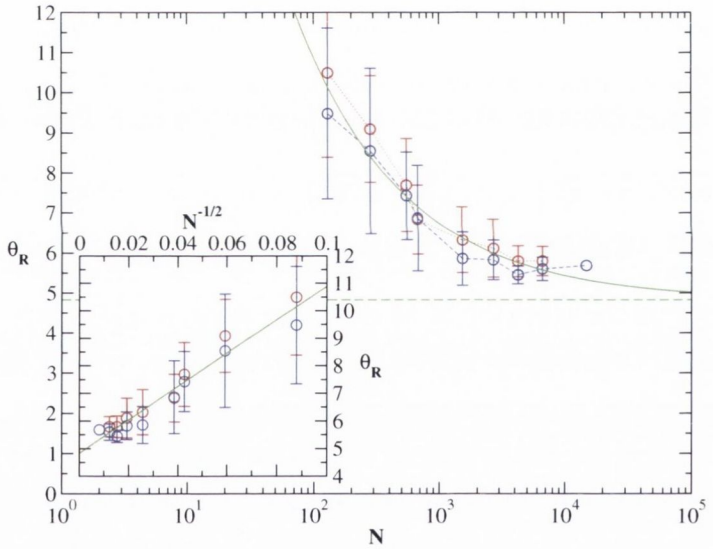

Figure 8.3.5: Plot of the static angle of repose versus the number of particles in the system. Bidisperse data are represented by (○) symbols and simulations with a uniform radius distribution are represented by (○). The solid green line represents Equation (8.3.2) fitted to the data. The dashed green line is the value of θ_R^{∞} as found from Equation (8.3.2). Inset: Plot of θ_R as a function of $N^{-1/2}$. The solid green line represents Equation (8.3.2) fitted to the data.

Polydispersity	N	No. of Simulations	R_D	Bu
Bidisperse	130	10	$18\langle R\rangle$	3.55×10^{-4}
Uniform	130	9	$18\langle R\rangle$	3.55×10^{-4}
Bidisperse	285	24	$26\langle R\rangle$	3.55×10^{-4}
Uniform	285	24	$26\langle R\rangle$	3.55×10^{-4}
Bidisperse	550	17	$36\langle R\rangle$	3.55×10^{-4}
Uniform	550	17	$36\langle R\rangle$	3.55×10^{-4}
Bidisperse	675	18	$40\langle R\rangle$	3.55×10^{-4}
Uniform	675	20	$40\langle R\rangle$	3.55×10^{-4}
Bidisperse	1520	17	$60\langle R\rangle$	3.55×10^{-4}
Uniform	1520	18	$60\langle R\rangle$	3.55×10^{-4}
Bidisperse	2700	18	$80\langle R\rangle$	3.55×10^{-4}
Uniform	2700	18	$80\langle R\rangle$	3.55×10^{-4}
Bidisperse	4225	10	$100\langle R\rangle$	3.55×10^{-4}
Uniform	4225	10	$100\langle R\rangle$	3.55×10^{-4}
Bidisperse	6580	8	$120\langle R\rangle$	3.55×10^{-4}
Uniform	6580	7	$120\langle R\rangle$	3.55×10^{-4}
Bidisperse	14800	1	$190\langle R\rangle$	3.55×10^{-4}

Table 8.2: Table of simulation data for variation with number of discs N.

to the data of form,

$$\theta_R = \theta_R^{\infty} + \frac{A}{\sqrt{N}} \tag{8.3.2}$$

where θ_R^{∞} is the value of the θ_R as $N \to \infty$ and A is a fitting constant. Fitting Equation (8.3.2) to the data yields that $\theta_R^{\infty} = (4.82 \pm 0.15)^{\circ}$ and $A = (60.6 \pm 3.6)^{\circ}$. This value of the θ_R^{∞} is consistent with that of other simulations and experiments of foam [103, 104, 105, 117].

In experiment it was not possible to opt for a drum of a different size because of the limitations of the experimental apparatus. Instead the size of the bubbles were altered and microbubble samples were created with $\langle R\rangle$ from $400\mu m$ to $600\mu m$. Various system sizes are investigated experimentally, from 234 bubbles to 1108 bubbles. It was not possible to prepare larger systems because if the bubbles are too small, they can assemble in double

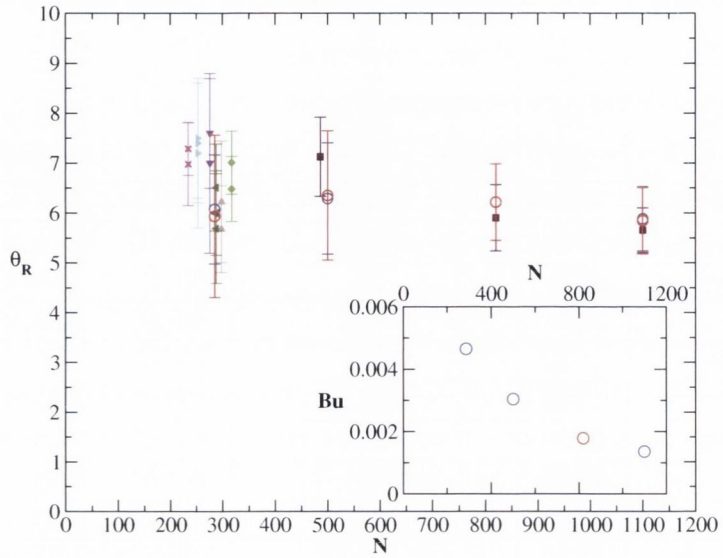

Figure 8.3.6: The effect on the static angle of repose with increasing system size when buoyancy is matched between simulation and experiment. Experimental polydisperse data is represented as (■), all other data is as before. Inset: Variation of simulation Bu with system size.

layers. However, changing the size of $\langle R \rangle$ also affects Bu through Equation (8.2.5). This means for increasing N in experiment that Bu is decreasing. In order to match simulation with experiment, the buoyancy force in the simulation needs to be altered for each system size. The Bu matched data between simulation and experiment for increasing system is plotted in Figure 8.3.6. The experimental data exhibits a similar trend to that shown in Figure 8.3.5, where larger systems have a smaller θ_R. The simulation results are in good agreement with the experimental data for all system sizes.

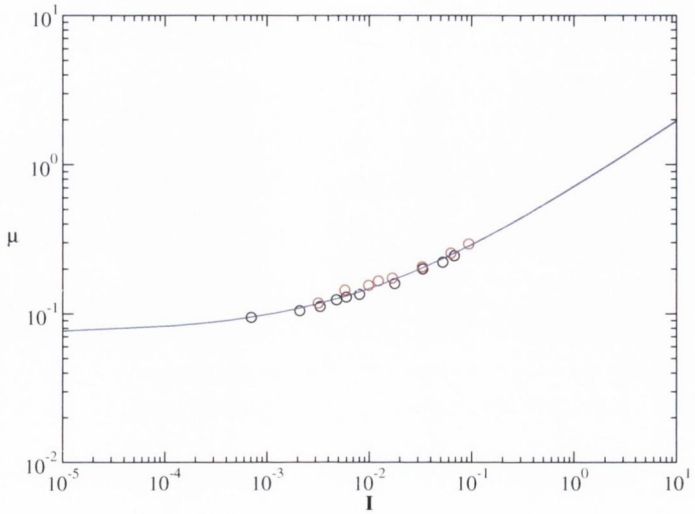

Figure 8.3.7: Macroscopic friction versus viscous number measured on the inner wall of Couette simulations for two packing fractions: $\phi = 0.95$ (○); $\phi = 0.90$ (○). The solid line is Equation (8.3.3) fit to the data.

8.3.5 Comparison with Couette Simulations

Returning briefly to Equation (6.1.2) outlined in Chapter 6. If we use the data measured on the inner wall of the Couette simulations in Chapter 7 for a variety of driving velocities at two different ϕ and then rescale this data by dividing σ by the normal stress on the walls of the simulation P and then plot this against a dimensionless shear rate given by $I = c_b\dot{\gamma}/P$, we see that this data collapses in Figure 8.3.7. Then substituting a form of $y(I)$ proposed by Peyneau and Roux [103] into Equation (6.1.2) we get

$$\mu = \mu_R + AI^b. \tag{8.3.3}$$

When Equation (8.3.3) is fit to the data plotted in Figure 8.3.7, a value of the exponent $b = 0.47 \pm 0.07$ is found. The value of macroscopic friction μ_R indicates $\theta_R = (4.2 \pm 0.6)^\circ$, in agreement with the rotating drum simulations.

8.3.6 Discussion of Angle of Repose

Let us discuss how a static angle of repose can exist if the bubbles do not exhibit any solid friction. The bubbles are trapped in the teeth on the edge of the drum and in turn frustrate bubbles above and so on. The boundary here creates a no slip boundary condition and creates a template for the bubbles located at the edge of the drum. Small systems have a larger proportion of bubbles on the boundary than large systems. Therefore small systems have less possibility to rearrange to a lower energy configuration than larger ones, leading to the static angle of repose being larger for smaller systems. This phenomenon is discussed for granular systems in Pouliquen and Renaut [136]. The authors employ the term effective friction. This effective friction is composed of a solid friction and a friction due to geometrical frustration. In the case of wet foam, this effective friction only depends on the geometry because there is no static friction. This frustration of a bubble being unable to flow past other bubbles due to their geometric arrangement can be thought of as a microscopic yield stress and hence the origin of the angle of repose.

If we imagine an experiment with an infinite number of bubbles, the finite size effect in this situation vanishes. We observed in Figure 8.3.5 that the simulation data strongly suggests that the static angle of repose tends to a constant (~ 4.8) as we increase the system size. This implies an angle of repose exists whatever the size of the system.

Measurements in a three-dimensional chute flow foam experiment by Lespiat et al. [104] have shown an angle at which the flow starts of 4.6°. This angle also increases for smaller systems, which corroborates our findings. It is interesting to note that the values of θ_R found in 2D simulations and experiments match those of 3D simulations [103] and 3D experiments [104].

8.4 Shear Dilatancy

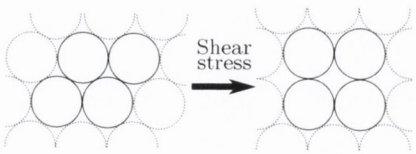

Figure 8.4.1: Typical stick-slip scenario in monodisperse foam. The change in configuration induced by shearing leads to an increase of free volume.

8.4.1 Concept of Dilatancy

Dilatancy is the tendency of a material to expand when it is sheared. This term was introduced by Reynolds [137] in the nineteenth century in the context of granular media. In this two-dimensional setup, the packing fraction is defined as the ratio of the area occupied by the bubbles and the total area occupied by the foam. When the system is sheared the foam expands and consequently the packing fraction becomes lower.

This property can be explained phenomenologically. The particles are trapped in the bulk of the material. When the system is subjected to a shear stress, the particles are rearranged within the pile and may have to slip or roll over each other (Figure 8.4.1). This leads to an increase of the area of the foam. Dilatancy of 2D foams was first described in theory and simulation by Weaire and Hutzler [138] and later a further theoretical model of dilatancy in foams was expanded upon by Rioual et al. [139]. Observations of dilatancy in experiments of 3D foams have been reported [104, 140]. Shear dilatancy has been previously reported for two-dimensional soft discs [43].

In this section we investigate dilatancy in the same rotating setup as before in simulation and experiment and compare the results.

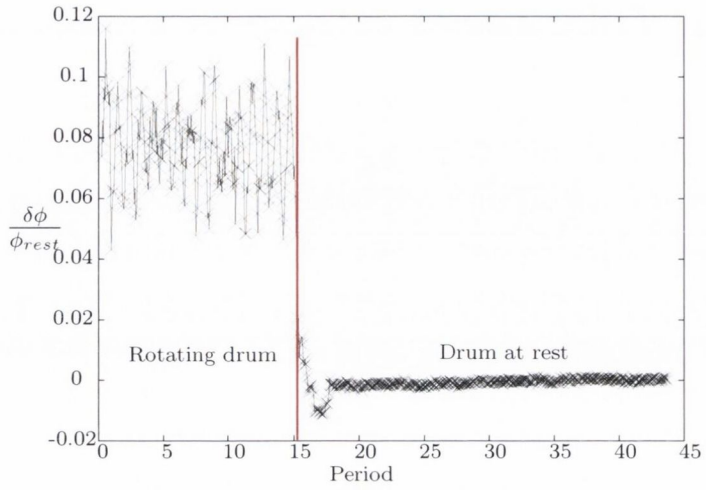

Figure 8.4.2: Example of a dilatancy experiment on a bidisperse sample of 285 bubbles. The rotation rate is $(11.77 \pm 0.05)^{\circ}s^{-1}$. The vertical (red) line marks the moment at which the drum stops rotating.

8.4.2 Methods

Dilatancy is a dynamic property, as opposed to the static property the angle of repose. In the case of 2D wet foams and granular material this may be investigated by measuring how much the area of a packing expands as the system is sheared. $\delta\phi$ is the change in packing fraction due to shear and is defined as

$$\delta\phi = \phi_{rest} - \phi_{shear}$$

where ϕ_{rest} is the packing fraction at rest and ϕ_{shear} is the packing fraction during shear. $\delta\phi > 0$ implies that ϕ is decreasing when shear stress is applied and that the foam is undergoing shear dilation.

Simulations were performed in the same manner as in Section 8.2. To perform the experiment, the drum is filled with approximately 250 bubbles in the same way as for the static angle of repose experiment. Shear stress was applied by rotating the drum at a rotation rate ω. Using image analysis (IDL) the centre of mass of the bubble pile was calculated from which the

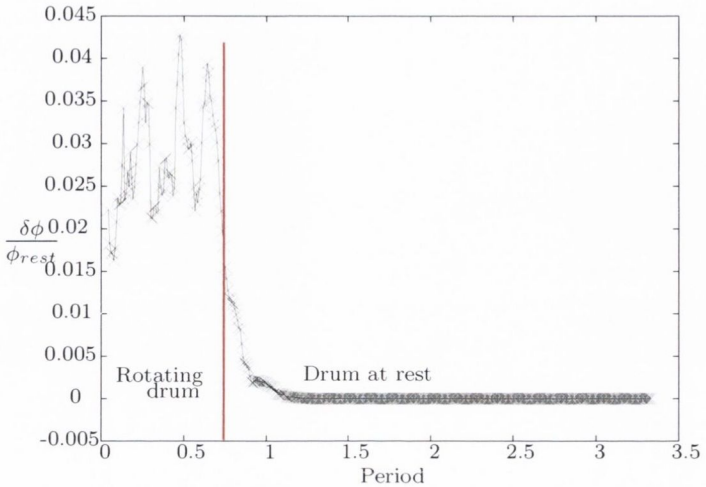

Figure 8.4.3: Example of a dilatancy simulation on a bidisperse sample of 285 bubbles. As in Figure 8.4.2, the vertical (red) line marks the moment at which the drum stops rotating. Rotation rate $\omega = 30\ ^{\circ}s^{-1}$.

packing fraction was found by the following method.

The radial distance of the centre of mass from the edge of the drum h_{COM} is measured. Then assuming the distribution of particles is homogeneous, the angle that the edge of the pile makes at the drum edge with the geometric centre of the drum, β can be found by,

$$R_D - h_{COM} = \frac{4R_D \sin^3\left(\frac{\beta}{2}\right)}{3(\beta - \sin(\beta))}. \tag{8.4.1}$$

Using β, the comparable homogenous area A_{occ} of the pile is calculated,

$$A_{occ} = \frac{R_D^2}{2}(\beta - \sin(\beta)). \tag{8.4.2}$$

The area of the particles in drum is known,

$$A_B = \sum_{i=1}^{N} \pi r_i^2 + \frac{\beta}{4\pi} \sum_{i=1}^{N_{boundary}} \pi r_i^2, \tag{8.4.3}$$

where r_i is the radius of a particle i. The packing fraction ϕ is then found from

$$\phi = \frac{A_B}{A_{occ}}. \tag{8.4.4}$$

The packing fraction of the system at rest in experiment is found to be $\phi = 0.9$ which is larger than the random close packing (recall $\phi_c \approx 0.84$ in 2D). This may be caused by partial crystallisation or boundary effects. In the simulated system with $N = 285$, ϕ is much lower at 0.837 ± 0.004. This difference from ϕ_c is attributed to the confinement of the system.

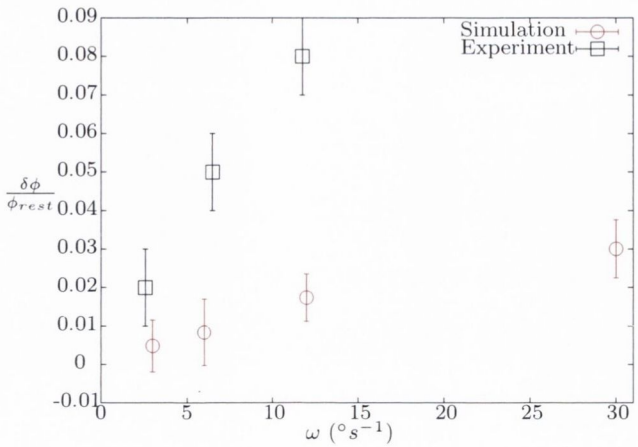

Figure 8.4.4: Dilatancy effect for different shear rate for both simulation and experiment. A bidisperse foam (composed of 2/3 of *big* bubbles (radius $(0.99 \pm 0.03)mm$) and 1/3 of *small* bubbles (radius $(0.63 \pm 0.03)mm$)) and a tilt angle $\alpha=(3.5\pm1)^\circ$ is used to perform the experiment. A bidisperse foam of 285 bubbles with a similar dimensionless number Bu is used for the experiment.

8.4.3 Results

Figure 8.4.2 and Figure 8.4.3 display the change in packing fraction when the system is sheared in experiment and simulation. Note that the wobble in the top plate of the experimental setup creates an oscillation around the average value of ϕ_{shear} during rotation and therefore induces a small error. In both cases, the system clearly exhibits shear dilatancy: the bubble pile expands when a shear stress is applied.

Dilatancy is greater for larger shear rates in both simulation and experiment as displayed in Figure 8.4.4. This is consistent with the results of Bagnold [141] who noted that dilatancy of granular materials altered with shear rate. However, we observe a linear trend for both simulation and experiment, while Bagnold noted a quadratic dependence on the shear rate. In a similar but confined simulated system Langlois et al. [43] found a power law

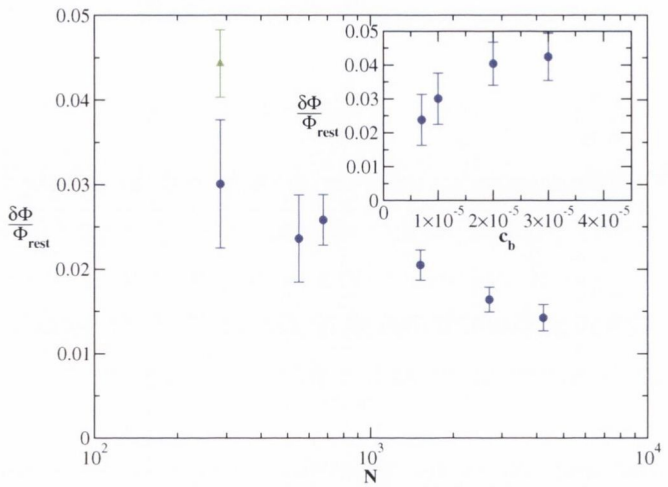

Figure 8.4.5: Dilatancy effect for different system size in simulation. A bidisperse foam of 285 bubbles with $Bu = 3.55 \times 10^{-4}$ is used for the simulation. (•) are for simulations when the drum is half filled and (▲) for 1/3 filled drum. Inset: Dilatancy effect for different coefficient of viscosity c_b.

dependence on the shear rate with an exponent of 0.4. Despite this common trend we observe a discrepancy between the value of the change of packing fraction for both the experimental case and the simulation. We also note a decrease of dilatancy with system size in Figure 8.4.5.

There are a number of factors that may affect the difference between the simulation and experimental results for shear dilation. First of all is the filling height: it is found in simulation that if the drum is filled to a lower fraction, the value of $\delta\phi/\phi_{rest}$, in contrast to θ_R, increases (Figure 8.4.5). Also, altering the coefficient of friction c_b can help bridge the disparity between simulation and experimental results (inset of Figure 8.4.5). The combination of all these effects have not been simulated to ascertain if the experimental result can be reproduced. It may be the case that a correct rescaling of the shear rate results in a collapse of results in Figure 8.4.4 onto the same trend.

8.4.4 Discussion of Dilatancy

We have shown that the dilatancy effect is more important when the system is sheared at a higher shear rate. This is similar to the dilatancy in 3D foams continuous shear observed by Marze et al. [140]. Increasing the shear rate leaves less time for bubbles to rearrange, requiring for bubbles to flow past each other by moving around each other and consequently the area increases. We get a constantly higher dilatancy effect in experiment than in simulation (see Figure 8.4.4). This may be the result of an additive viscous drag created by the top plate or due to difference in the viscous interactions in simulation and experiment. The presence of the confining top plate during shear means that a drag is imposed on the entire bubble pile rather than just at the boundary, as in the simulation. This drag applied to the entire foam may add to the frustration of the flow of the bubbles, again leading to a greater increases in the area of the bubble pile.

There is a competition between the rotation rate and the time scale of bubble relaxation. The time of relaxation depends on viscosity therefore it takes longer for bubbles to relax when a viscous drag is added and consequently decreases the packing fraction ϕ.

8.5 Angle When Flow Begins

Onset of granular flows have been studied by Pouliquen [142] and Pouliquen and Forterre [143]. Hysteresis between the angle at which the pile starts flowing and at which it stops flowing has been observed in the flow of granular materials down inclined planes. Using the rotating drum setup we investigate when the angle at which flow starts θ_{start} and whether this is the same as θ_R. Starting with a relaxed pile with non-zero θ_R, we rotate the drum in the opposite direction. Ideally, the foam would rotate as a solid body rotation before starting to flow. When the rotation would be equal to θ_{start}, one would expect a flowing behaviour different from solid body rotation. As seen in Figure 8.5.1, the transition between the solid body rotation and the flowing behaviour is too smooth to accurately determine the onset of flow.

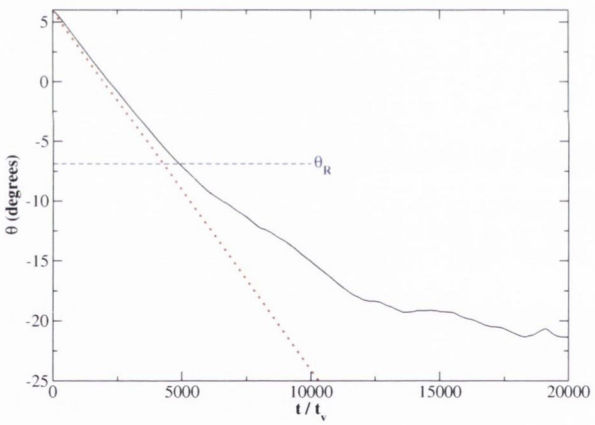

Figure 8.5.1: Angle at which the flow starts in simulation. The solid line is the angle the centre of mass makes relative to the centre of the drum. The dotted line is the angle the centre of mass would take should the pile rotate as a solid body and the dashed line marks the average angle of repose for this system. Data is for a bidisperse packing of 675 discs with $R_D = 40\langle R \rangle$.

8.6 Conclusions & Outlook

By means of experiment and simulation of two-dimensional wet foam in a rotating drum configuration, we have demonstrated the existence of a static angle of repose. The results obtained are robust and reproducible within error bars. Limited polydispersity in samples that do not crystallise does not have a significant effect on the value of θ_R. Except in the case of monodisperse size distributions, the values of θ_R in simulation and experiment are in agreement. This agreement is particularly good when Bu in simulations is tuned to that of the experiment. Small changes of buoyancy do not affect θ_R, but the size of the system has a pronounced effect. The smaller the system, the higher the static angle of repose. Small N means that there are less degrees of freedom to relax to a lower θ_R. When the system's size N is increased, the angle is found to tend to a constant.

The simulation gives remarkably accurate results for the angle of repose θ_R considering the simplicity of the model used. The behaviour of the simulation results match those measured in experiment very well. Studying bubbles is a good way to isolate the geometrical frustration effect occurring in granular materials. The puzzling question that remains to be answered is: What sets this angle? So far no convincing theoretical argument has been given for the size of this angle.

The observation of shear dilatancy also requires further study to explain the discrepancy between the results in experiment and in simulation. This may require a modification to the bubble model to describe this effect or it could require finding a correct rescaling of the viscous interactions from the imposed driving velocities in simulation and experiment. For a comprehensive comparison of the shear dilatancy, an experimental setup that does not have an artefact affecting its rotation of the foam is required, or altering the simulation to include this artefact.

Appendix A

Statistical cutoff

For all equations fitted and figures plotted of averaged quantities, any binned data with less than 100 particles are omitted from Part I of this thesis. This cutoff was decided upon after inspection of the data. We found by applying an arbitrary cutoff for all averaged quantities of 100 particles was sufficient to filter out noise while preserving the trends in the data.

In Figure A.0.1 we have shown the relationship between the average number of contacts a particle of size a has for all the polydispersities. We have shown both after (in Figure A.0.1 (a)) and before (Figure A.0.1 (b)) the cutoff has been applied. The trend in the data is unaffected by the inclusion of more data points in Figure A.0.1. This example is typical of the other plots where we apply this cutoff.

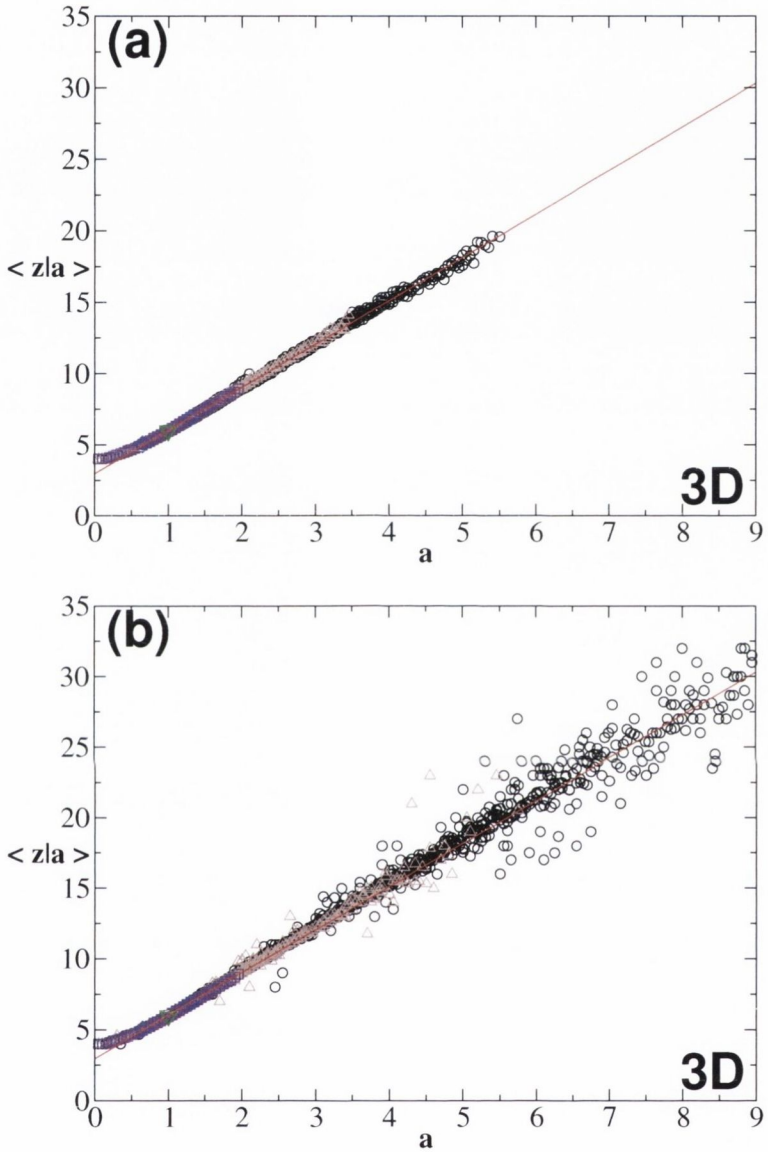

Figure A.0.1: The average contact number for particles of a given area a at ϕ_c in 3D for all ($\triangledown$) monodisperse, ($\Diamond$) bidisperse, ($\square$) uniform, ($\triangle$) Gaussian and ($\circ$) lognormal size distributions at all the widths σ_R we have considered (see Figure 2.3.2). The solid red line is a fit to Equation (3.2.3). In (a) only data binned with more than 100 particles have been plotted, while in (b) all data has been plotted.

Appendix B

Ordering in 3D Monodisperse Packings for Increasing Packing Fraction

To investigate whether packings become more ordered with increasing packing fraction for the packing algorithm outlined in Section 2.2.2, three monodisperse packings at three different ϕ are analysed for local order. The three packings are at $\phi = \phi_c$, $\phi = 0.75$ and $\phi = 1.00$. For each of these packings the Bond Orientational Order Parameter (BOOP) is calculated for each particle and plotted in Figure B.0.1.

The BOOP or Steinhardt order parameter is a measure of the rotational order within a sample [144] and has proved useful in identifying crystalline structures. The bond orientation parameter is based upon the association of a spherical harmonic $Q_{ml} = Y_l^m(\phi_{ij}, \theta_{ij})$ with each bond in the system, which in this case is defined as a contact. A contact in the context of the BOOP is defined as a vector $\mathbf{r}_{ij}$ joining the centre positions of neighbouring particles i and j. ϕ_{ij} and θ_{ij} are the polar and azimuthal angles of this bond with respect to a spherical coordinate system. In order to guarantee directional invariance of the BOOP only even spherical harmonics are considered. For

symmetric packings the first non-zero results are obtained for $l = 4$ and $l = 6$. The averaged 4^{th} and 6^{th} spherical harmonic are defined as,

$$Q_4 = \left(\frac{4\pi}{9} \sum_{m=-4}^{4} \frac{1}{n_i} \left| \sum_{j=1}^{n_i} Y_4^m(\phi_{ij}, \theta_{ij}) \right|^2 \right)^{1/2} \tag{B.0.1}$$

$$Q_6 = \left(\frac{4\pi}{13} \sum_{m=-6}^{6} \frac{1}{n_i} \left| \sum_{j=1}^{n_i} Y_6^m(\phi_{ij}, \theta_{ij}) \right|^2 \right)^{1/2} \tag{B.0.2}$$

where Y_l^m is the l^{th} spherical harmonic, n_i is the number of contacts of the particle being considered and N is the total number of particles with the system [144, 145]. Each crystal structure has a unique set of Q_4 and Q_6 with which it may be identified and the values of some common crystal structure are shown in Table B.1.

In Figure B.0.1 the Q_4 and Q_6 values for fcc, hcp and bcc crystals are plotted. It has been shown in experiment that packings of monodisperse

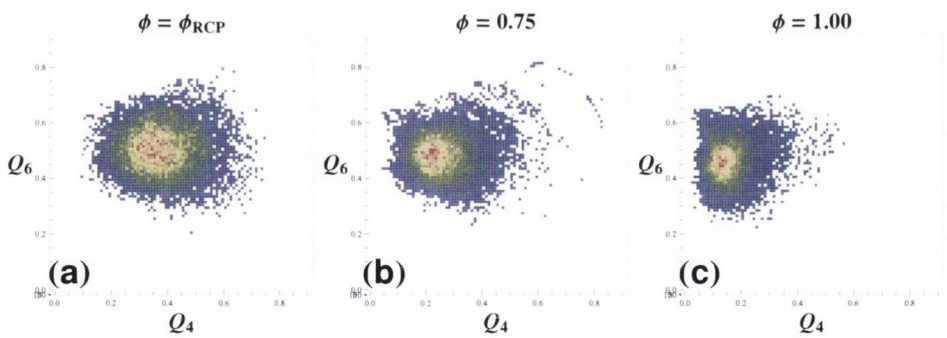

Figure B.0.1: Bond Orientation Order Parameter for a packing of monodisperse particles for increasing ϕ labelled from left to right, $\phi = \phi_c$, $\phi = 0.75$, $\phi = 1.00$. The plots are coloured with a spectrum representing the frequency of occurrence of a given pair of Q_4 and Q_6, where blue indicates low occurrence through to red, which indicates high occurrence. The values that are associated with crystalline ordering (see Table B.1) are shown as (•).

Structure	Q_4	Q_6
FCC	0.19094	0.57252
HCP	0.09722	0.48476
BCC	0.50918	0.62854

Table B.1: Table of Bond Order Orientation Parameters of some common crystalline structures [146].

foams tend to form crystal structures that are predominately fcc and hcp. In the first image at ϕ_c a wide range of Q_4 and Q_6 values are found for a packing. This is reminiscent of a liquid system [145] and is unsurprising as the random closed packed monodisperse spheres were first studied as a model for liquids [15]. When the BOOP is studied at $\phi = 0.75$ which is slightly above the packing fraction associated with fcc crystals of $\phi = 0.7405$, in Figure B.0.1 (b) there is a higher cluster of values of the BOOP but this is not at any characteristic value of crystal ordering. This indicates that the sample is becoming more ordered. This is again shown in B.0.1 (c) where there are some particles that have the Q_4 and Q_6 values of an hcp crystal but the majority of particles do not. This implies that the packing is more ordered but not a fully crystalline state. The inability to get to an expected crystalline state is due to the simulation procedure. There is no annealing step in the CG minimisation method that allows a packing to overcome a local energetic minimum and therefore cannot find the global energy minimum which in this case would be an fcc or hcp crystal. Another possibility is the templating effect of a confining container is required for packings to order fully.

Appendix C

Stress and Strain Rate in Polar Coordinates

C.1 Shear Stress

Here we present a derivation from Timoshenko and Goodier [147] for the shear stress in polar coordinates.

Consider the equilibrium of a small element 1234, cut out from the plate by the radial sections 04, 02 normal to the plate and by two cylindrical surfaces 3, 1, normal to the plate. The normal stress component in the radial direction is denoted by σ_{rr}, the normal component in the circumferential direction by $\sigma_{\theta\theta}$, and the shear stress component by $\sigma_{r\theta}$, each symbol representing stress at the mid-point of the element P with coordinates $(r+{}^{dr}/_{2}, \theta+{}^{d\theta}/_{2})$. On account of the variation of the stress, the values at the mid-points of the sides 1,2,3,4 are not quite the same as the values σ_{rr},$\sigma_{\theta\theta}$,$\sigma_{r\theta}$, and are denoted by $\sigma_{rr,1}$, etc. in Figure C.1.1.

By balancing the forces in the tangential direction, we can find the Cauchy equilibrium condition. We have the normal forces on side 4, $\sigma_{rr,4}dr$ and on the opposing side 2, $-\sigma_{rr,2}dr$. The shear stress on side 4 also have a component in the azimuthal direction, given by, $\sigma_{r\theta,4}dr\sin(d\theta/2)$, which can

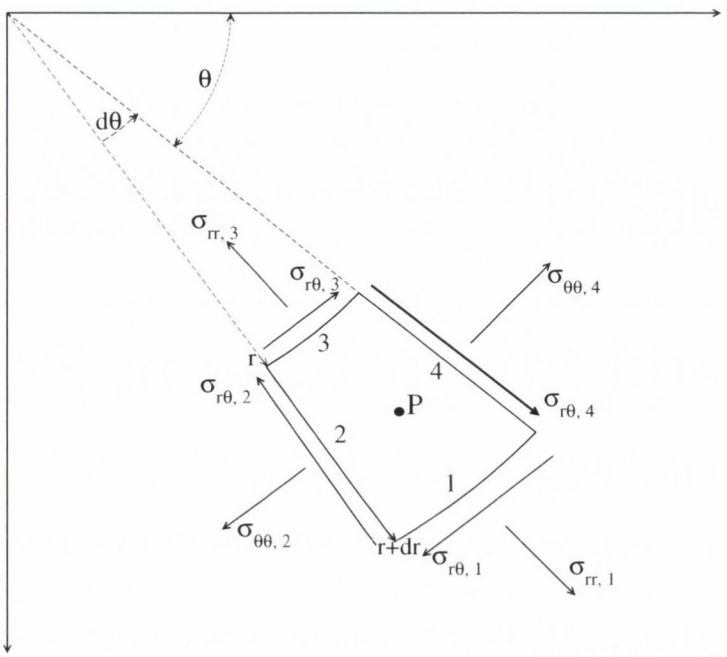

Figure C.1.1: Infinitesimal element in polar coordinates.

be approximated to $\sigma_{r\theta,4} dr d\theta/2$. The same approach can be taken for side 2 where the shear stress component gives $\sigma_{r\theta,2} dr d\theta/2$. The shear stress on sides 1 and 3 are given by $\sigma_{r\theta,1}(r+dr/2)d\theta$ and $\sigma_{r\theta,3}(r-dr/2)d\theta$ respectively.

Summing up all the forces in the tangential direction, we obtain the equation of equilibrium

$$(\sigma_{\theta\theta,4} - \sigma_{\theta\theta,2})dr + \frac{1}{2}(\sigma_{r\theta,4} + \sigma_{r\theta,2})dr d\theta + (\sigma_{r\theta,1}(r + \frac{dr}{2}) - \sigma_{r\theta,3}(r - \frac{dr}{2}))d\theta = 0. \tag{C.1.1}$$

Dividing by $dr d\theta$ this becomes

$$\frac{\sigma_{\theta\theta,2} - \sigma_{\theta\theta,4}}{d\theta} + \frac{1}{2}(\sigma_{r\theta,4} + \sigma_{r\theta,2}) + \frac{\sigma_{r\theta,1}(r + \frac{dr}{2}) - \sigma_{r\theta,3}(r - \frac{dr}{2})}{dr} = 0. \tag{C.1.2}$$

If the dimensions of the element are now taken smaller and smaller, to

the limit zero, the first term of this equation is in this limit $\partial\sigma_{\theta\theta}/\partial\theta$. The second becomes $\sigma_{r\theta}$, and the third $\partial(r\sigma_{r\theta})/\partial r$. Differentiating the third term results in

$$\frac{\partial\sigma_{\theta\theta}}{\partial\theta} + \sigma_{r\theta} + \sigma_{r\theta} + r\frac{\partial\sigma_{r\theta}}{\partial r} = 0. \tag{C.1.3}$$

Then dividing by r gives,

$$\frac{1}{r}\frac{\partial\sigma_{\theta\theta}}{\partial\theta} + \frac{2\sigma_{r\theta}}{r} + \frac{\partial\sigma_{r\theta}}{\partial r} = 0. \tag{C.1.4}$$

If we assume that the solution has circular symmetry, as is the case in the Taylor–Couette geometry, then $\sigma_{\theta\theta}$ becomes zero. If we change the notation so that $\sigma_{r\theta} = \sigma$, then Equation C.1.4 becomes

$$\frac{\partial\sigma}{\partial r} + \frac{2\sigma}{r} = 0, \tag{C.1.5}$$

the same expression as Equation (6.2.1).

C.2 Strain Rate

Here we reproduce the derivation found in Acheson [148].

The infinitesimal strain rate tensor in generalised coordinates is defined as

$$\dot{\gamma}_{ij} = \frac{\partial u_i}{\partial e_j} + \frac{\partial u_j}{\partial e_i}, \tag{C.2.1}$$

where $\boldsymbol{u}$ is the flow velocity vector and $\boldsymbol{e}$ is the position vector. Writing this generally in terms of the vector components gives

$$\dot{\gamma}_{ij} = (\boldsymbol{e}_i \cdot \nabla)(\boldsymbol{u} \cdot \boldsymbol{e}_j) + (\boldsymbol{e}_j \cdot \nabla)(\boldsymbol{u} \cdot \boldsymbol{e}_i), \tag{C.2.2}$$

which can be written more generally again as

$$\dot{\gamma}_{ij} = [(\boldsymbol{e}_i \cdot \nabla)\boldsymbol{u}] \cdot \boldsymbol{e}_j) + [(\boldsymbol{e}_j \cdot \nabla)\boldsymbol{u}] \cdot \boldsymbol{e}_i. \tag{C.2.3}$$

Looking for the shear strain rate in polar coordinates, gives $\nabla = (\frac{\partial}{\partial r}, \frac{\partial}{r\partial\theta})$, then the shear strain rate is

$$\dot{\gamma}_{r\theta} = \left[\frac{\partial}{\partial r}(u_r e_r + u_\theta e_\theta)\right] \cdot \boldsymbol{e}_\theta + \left[\frac{\partial}{r\partial\theta}(u_r e_r + u_\theta e_\theta)\right] \cdot \boldsymbol{e}_r. \tag{C.2.4}$$

In polar coordinates the unit position vectors have the identities

$$\frac{\partial e_r}{\partial \theta} = e_\theta, \tag{C.2.5}$$

$$\frac{\partial e_\theta}{\partial \theta} = -e_r. \tag{C.2.6}$$

Therefore Equation (C.2.4) simplifies to

$$\dot{\gamma}_{r\theta} = \frac{\partial u_\theta}{\partial r} + \left[\frac{1}{r}\left(\frac{\partial u_r}{\partial \theta} e_r + u_r e_\theta + \frac{\partial u_\theta}{\partial \theta} - u_\theta e_r\right)\right] \cdot e_r. \tag{C.2.7}$$

When the dot product is applied then the only non zero terms are

$$\dot{\gamma}_{r\theta} = \frac{\partial u_\theta}{\partial r} + \frac{1}{r}\left(\frac{\partial u_r}{\partial \theta} - u_\theta\right). \tag{C.2.8}$$

Assuming that there is no flow in the radial direction and choosing the convention of θ so that the flow is always positive, with a change of notation so that $\dot{\gamma}_{r\theta} = \dot{\gamma}$ then we recover,

$$\dot{\gamma} = \left|\frac{\partial u_\theta}{\partial r} - \frac{u_\theta}{r}\right|, \tag{C.2.9}$$

the same expression as Equation (6.2.3).

Bibliography

[1] D. Weaire and S. Hutzler. Foams as a complex system. *J. Phys.:Condens. Matter*, 21(474227), 2009.

[2] D. Weaire and S. Hutzler. *The Physics of Foams*. Clarendon Press, Oxford, 1999.

[3] F. Bolton and D. Weaire. Rigidity loss transition in a disordered 2d froth. *Phys. Rev. Lett.*, 65(3449), 1990.

[4] J. A. F. Plateau. *Statique Expérimentale et Théorique des Liquides soumis aux Seules Forces Moléculaires*. Paris: Gauthier-Villars, 1873.

[5] M-D. Lacasse, G. S. Grest, D. Levine, T. G. Mason, and D. A. Weitz. Model for the elasticity of compressed emulsions. *Phys. Rev. Lett.*, 76(3448), 1996.

[6] R. Höhler and S. Cohen-Addad. Rheology of liquid foam. *J. Phys.:Condens. Matter*, 17(R1041), 2005.

[7] A. J. Liu and S. R. Nagel. Nonlinear dynamics: Jamming is not just cool any more. *Nature*, 396(21), 1998.

[8] A. J. Meagher, M. Mukherjee, D. Weaire, S. Hutzler, J. Banhart, and F. Garcia-Moreno. Analysis of the internal structure of monodisperse liquid foams by x-ray tomography. *Soft Matter*, 7(9881), 2011.

[9] L. E. Silbert, A. J. Liu, and S. R. Nagel. Structural signatures of the unjamming transition at zero temperature. *Phys. Rev. E*, 73(041304), 2006.

[10] D. Weaire and S. Hutzler. *An Introduction To Rheology.* Elsevier, Amsterdam, 1989.

[11] T. Aste and D. Weaire. *The Pursuit of Perfect Packing.* Bristol and Philadelphia: IOP Publishing Ltd, 2000.

[12] T. C. Hales. Historical overview of the kepler conjecture. *Discr. Comput. Geom.*, 36(5), 2006.

[13] T. C. Hales. A proof of the kepler conjecture. *Ann. Math.*, 162(1065), 2005.

[14] J. D. Bernal. A geometrical approach to the strucure of liquids. *Nature*, 183 (141), 1959.

[15] J. D. Bernal and J. Mason. Packing of spheres: Co-ordination of randomly packed spheres. *Nature*, 188(910), 1960.

[16] J. G. Berryman. Random close packing of hard spheres and discs. *Phys. Rev. A*, 27(1053), 1983.

[17] A. Donev, I. Cisse, D. Sachs, E. A. Variano, F. H. Stillinger, R. Connelly, S. Torquato, and P. M. Chaikin. Improving the density of jammed disordered packings using ellipsoids. *Science*, 303(990), 2004.

[18] M. van Hecke. Jamming of soft particles: Geometry, mechanics, scaling and isostaticity. *J. Phys.:Condens. Matter*, 22(033101), 2010.

[19] S. Torquato, T.M. Truskett, and P.G. Debenedetti. Is random close packing of sphere well defined? *Phys. Rev. Lett.*, 84(2064), 2000.

[20] G. W. Delaney, J. E. Hilton, and P. W. Cleary. Defining random loose packing for nonspherical grains. *Phy. Rev. E*, 83(051305), 2011.

[21] P. W. Anderson. Through the glass lightly. *Science*, 267(1615), 1995.

[22] M. Wyart. On the rigidity of amorphous solids. *Ann. Phys. Fr.*, 30(1), 2005.

[23] E. I. Corwin. Getting into a proper jam. *Physics*, 5(97), 2012.

[24] C. S. O'Hern, L. E. Silbert, S. R. Nagel, and A. J. Liu. Jamming at zero temperature and zero applied stress: The epitome of disorder. *Phys. Rev. E*, 68(011306), 2003.

[25] P. Charbonneau, E. I. Corwin, G. Parisi, and F. Zamponi. Universal microstructures and mechanical stability of jammed packings. *Phys. Rev. Lett.*, 109(205501), 2012.

[26] P. Chaudhuri, L. Berthier, and S. Sastry. Jamming transitions in amorphous packings of frictionless spheres occur over a continuous range of volume fractions. *Phys. Rev. Lett.*, 104(165701), 2010.

[27] S. Alexander. Amorphous solids: Their structure, lattic dynamics and elasticity. *Phys. Rep.*, 296(65), 1998.

[28] C. F. Moukarzel. Isostatic phase transition and instability in stiff granular materials. *Phys. Rev. Lett.*, 81(1634), 1998.

[29] C. P. Goodrich, A. J. Liu, and S. R. Nagel. Finite-size scaling at the jamming transition. *Phys. Rev. Lett.*, 109(095704), 2012.

[30] S. Dagois-Bohy, B. P. Tighe, J. Simon, S. Henkes, and M. van Hecke. Soft-sphere packings at finite pressure but unstable to shear. *Phys. Rev. Lett.*, 109(9), 2012.

[31] R. J. Speedy. Glass transition in hard disc mixtures. *J. Chem. Phys.*, 110 (4559), 1999.

[32] M. R. Sadr-Lahijany, P. Ray, and H. E. Stanley. Dispersity-driven melting transition in two-dimensional solids. *Phys. Rev. Lett.*, 79(3206), 1997.

[33] S. Yerazunis, S. W. Cornell, and B. Winter. Dense random packing of binary mixtures of spheres. *Nature*, 207(835), 1965.

[34] A. R. Kansal, S. Torquato, and F. H. Stillinger. Computer generation of dense polydisperse sphere packings. *Journal of Chemical Physics*, 117(8212), 2002.

[35] A. S. Clarke and J. D. Wiley. Numerical simulation of the dense random packing of a binary mixture of hard spheres: Amorphous metals. *Phys. Rev. B*, 35(7350), 1987.

[36] N. Xu, J. Blawzdziewicz, and C. S. O'Hern. Random close packing revisited: Ways to pack frictionless disks. *Phys. Rev. E*, 71(061306), 2005.

[37] W. Schaertl and H. Sillescu. Brownian dynamics of polydisperse collodial hard spheres: Equilibrium structures and random close packings. *J. Stat. Phys.*, 77(1994), 1994.

[38] D. He, N. N. Ekere, and L. Cai. Computer simulation of random packing of unequal particles. *Phys. Rev. E*, 60(7098), 1999.

[39] R. S. Farr and R. D. Groot. Close packing density of polydisperse hard spheres. *J. Chem. Phys.*, 131(244104), 2009.

[40] S. Phan, W. B. Russel, J. Zhu, and P. M. Chaikin. Effects of polydispersity on hard sphere crystals. *J. Chem. Phys.*, 108(9789), 1998.

[41] K. Lochmann, L. Oger, and D. Stoyan. Statistical analysis of random sphere packings with variable radius distribution. *Solid State Sciences*, 8(1397), 2006.

[42] D. J. Durian. Foam mechanics at the bubble scale. *Phys. Rev. Lett.*, 75 (4780), 1995.

[43] V. J. Langlois, S. Hutzler, and D. Weaire. Rheological properties of the soft-disk model of two-dimensional foams. *Phys. Rev. E*, 78(021401), 2008.

[44] E. I. Corwin, M. Clusel, A. O. N. Siemens, and J. Brujic. Model of random packing of polydisperse frictionless spheres. *Soft Matter*, 6(2949), 2010.

[45] G. Katgert, M. E. Möbius, and M. van Hecke. Rate dependence and role of disorder in linearly sheared two-dimensional foams. *Phys. Rev. Lett.*, 101 (058301), 2008.

[46] N. D. Denkov, S. Tcholakova, K. Golemanov, V. Subramanian, and A. Lips. Foam-wall friction: Effect of air volume fraction for tangentially immobile bubbles surface. *Coll. Surf. A*, 282-283(329), 2006.

[47] N. D. Denkov, S. Tcholakova, K. Golemanov, K. P. Ananthpadmanabhan, and A. Lips. The role of surfactant type and bubble surface mobility in foam rheology. *Soft Matter*, 5(3389), 2009.

[48] F. P. Bretherton. The motion of long bubbles in tubes. *J. Fluid Mech.*, 10 (166), 1961.

[49] M. B. Sexton, M. E. Möbius, and S. Hutzler. Bubble dynamics and rheology in sheared two-dimensional foams. *Soft Matter*, 7(11252), 2011.

[50] M. Clusel, E. I. Corwin, A. O. N. Siemens, and J. Brujic. A 'granocentric' model for random packing of jammed emulsions. *Nature*, 460(611), 2009.

[51] W. H Press, B. P. Flannery, S. A Teukolsky, and W. T. Vetterling. *Numerical Recipes in C*. Cambridge University Press, Cambridge, 1995.

[52] I. Biazzo, F. Caltagirone, G. Parisi, and F. Zamponi. Theory of amorphous packings of binary mixtures of hard spheres. *Phys. Rev. Lett.*, 102(195701), 2009.

[53] J. Brujic, S. Edwards, I. Hopkinson, and H. A. Makse. Measuring the distribution of interdroplet forces in a compressed emulsion system. *Physica A*, 327(201), 2003.

[54] G. Katgert and M. van Hecke. Jamming and geometry of two-dimensional foams. *Europhys. Lett.*, 92(34002), 2010.

[55] K. A. Newhall, I. Jorjadze, E. Vanden-Eijnden, and J. Brujic. A statistical mechanics framework captures the packing of monodisperse particles. *Soft Matter*, 7(11518), 2011.

[56] M. Durand, J. Käfer, C. Quilliet, S. Cox, S. A. Talebi, and F. Graner. Statistical mechanics of two-dimensional shuffled foams: Prediction of the

correlation between geometry and topology. *Phys. Rev. Lett.*, 107(168304), 2011.

[57] C. Quilliet, S. A. Talebi, D. Rabaud, J. Käfer, S. J. Cox, and F. Graner. Topological and geometrical disorders correlate robustly in two dimensional foams. *Phil. Mag. Lett.*, 88(651), 2008.

[58] M. P. Miklius and S. Hilgenfeldt. Analytical results for size-topology correlations in 2d disc and cellular packings. *Phys. Rev. Lett.*, 108(015502), 2012.

[59] K. A. Newhall, L. L. Pontani, I. Jorjadze, S. Hilgenfeldt, and J. Brujic. Size-topology relations in packings of grains, emulsions, foams and biological cells. *Phys. Rev. Lett.*, 108(268001), 2012.

[60] T. S. Majmudar and R. P. Behringer. Contact force measurements and stress-induced anisotropy in granular materials. *Nature*, 435(1079), 2005.

[61] S. Ostojic, E. Somfai, and B. Nienhuis. Scale invariance and univarsality of force networks in static granular matter. *Nature*, 439(828), 2006.

[62] H. A. Makse, D. L. Johnson, and L. M. Schwartz. Packing of compressible granular materials. *Phys. Rev. Lett.*, 84(4160), 2000.

[63] J. A. Dodds. The porosity and contact points in multicomponent random sphere packings calculated by a simple statistical geometric model. *J. Colloid Interface Sci.*, 77(317), 1980.

[64] C. B. O'Donovan and M. E. Möbius. Spatial correlations in polydisperse, frictionless, two-dimensional packings. *Phys. Rev. E*, 84(020302), 2011.

[65] J. Leech. The problem of the thirteen spheres. *The Mathematical Gazette*, 40(22), 1956.

[66] M. Clusel. Granocentric model prediction for lognormal size distribution of width $\sigma = 0.30$. Private communications, 2012.

[67] B. P. Tighe, J. H. Snoeijer, T. J. H. Vlugt, and M. van Hecke. The force network ensemble for granular packings. *Soft Matter*, 6(2908), 2010.

[68] D. Weaire. Some remarks on the arrangement of grains in a polycrystal. *Metallography*, 7(157), 1974.

[69] F. T. Lewis. The correlation between cell division and the shapes and sizes of prismatic cells in the epidermis of cucumis. *Anat. Rec.*, 38(341), 1928.

[70] C. M. Grinstead and J. L. Snell. *Introduction to probability*. American Mathematical Society, Providence, R.I., U.S.A., 2nd rev. ed. edition, 1997.

[71] C. S. O'Hern, S. A. Langer, A. J. Liu, and S. R. Nagel. Force distributions near jamming and glass transitions. *Phys. Rev. Lett.*, 86(111), 2001.

[72] J. Zhou, S. Long, Q. Wang, and A. D. Dinsmore. Measurement of forces inside a three-dimensional pile of frictionless droplets. *Science*, 312(1631), 2006.

[73] F. Radjai, M. Jean, J. J. Moreau, and S. Roux. Force distributions in dense two-dimensional granular systems. *Phys. Rev. Lett.*, 77(274), 1996.

[74] A. R. T. van Eerd, W. G. Ellenbroek, M. van Hecke, J. H. Snoeijer, and T. J. H. Vlugt. Tail of the contact force distribution in static granular materials. *Phys. Rev. E*, 75(060302), 2007.

[75] J. H. Snoeijer, T. J. H. Vlugt, M. van Hecke, and W. van Saarloos. Force network ensemble: A new approach to static granular matter. *Phys. Rev. Lett.*, 92(054302), 2004.

[76] L. Kondic, A. Goullet, C. S. O'Hern, M. Kramar, K. Mishaikow, and R. P. Behringer. Topology of force networks in compressed granular media. *Europhys. Lett.*, 97(54001), 2012.

[77] C. Voivret, F. Radjai, J.-Y. Delenne, and M. S. El Youssoufi. Multiscale force networks in highly polydisperse granular media. *Phys. Rev. Lett.*, 102 (178001), 2009.

[78] C. Song, P. Wang, and H. A. Makse. A phase diagram for jammed matter. *Nature*, 453(629), 2008.

[79] B. P. Tighe, A. R. T. van Eerd, and T. J. H. Vlugt. Entropy maximization in the force network ensemble for granular solids. *Phys. Rev. Lett.*, 100 (238001), 2008.

[80] N. Rivier and A. Lissowski. On the correlation between sizes and shapes of cells in epithelial mosaics. *J. Phys. A: Math. Gen.*, 15(L143), 1982.

[81] D. A. Aboav. The arrangement of grains in a polycrystal. *Metallography*, 3 (383), 1970.

[82] D. Weaire and N. Rivier. Soap, cells and statistics - random patterns in two dimensions. *Contemp. Phys.*, 25(59), 1984.

[83] K. A. Brakke. 200,000,000 random voronoi polygons. Technical report, Department of Mathematical Sciences, Susquehanna University, Selinsgrove PA 17870, USA, 1985.

[84] C. Godrèche, I. Kostov, and I. Yekutieli. Topological correlations in cellular structures and planar graph theory. *Phys. Rev. Lett.*, 19(2674), 1992.

[85] G. Schliecker. Structure and dynamics of cellular systems. *Adv. Phys.*, 51 (1319), 2002.

[86] R. Y. Yang, R. P. Zou, and A. B. Yu. Voronoï tessellation of the packing of fine uniform spheres. *Phys. Rev. E*, 65(041302), 2001.

[87] M. A. Fortes. Applicability of the lewis and aboav-weaire laws to 2d and 3d cellular structure based on poisson partitions. *J. Phys. A: Math. Gen.*, 28 (1055), 1995.

[88] R. Delannay and G. Le Cäer. Topological characteristics of 2d cellular structures generated by fragmentation. *Phys. Rev. Lett.*, 73(1553), 1994.

[89] C. Sire and M. Seul. Maximum entropy analysis of disordered droplet patterns. *J. Phys. I*, 5(97), 1995.

[90] M. Seul, N. Y. Morgan, and C. Sire. Domain coarsening in a two-dimensional binary mixture: Growth dynamics and spatial correlations. *Phys. Rev. Lett.*, 73(17), 1994.

[91] T. S. Majmudar, M. Sperl, S. Luding, and R. P. Behringer. Jamming transition in granular systems. *Phys. Rev. Lett.*, 98(058001), 2007.

[92] C. Zhao, K. Tian, and N. Xu. New jamming scenario: From marginal jamming to deep jamming. *Phys. Rev. Lett.*, 106(125503), 2011.

[93] A. E. Roth, B. G. Chen, and D. J. Durian. Structure and coarsening at the surface of a dry three-dimensional aqueous foam. *Phy. Rev. E*, 88(062302), 2013.

[94] A. E. Roth, C. D. Jones, and D. J. Durian. Bubble statistics and coarsening dynamics for quasi-two-dimensional foams with increasing liquid content. *Phys. Rev. E*, 87(042304), 2013.

[95] H. Flyvbjerg. Model for coarsening froths and foams. *Phy. Rev. E*, 47(4037), 1993.

[96] K. Y. Szeto and W. Y. Tam. Lewis' law versus feltham's law in soap froth. *Physica A*, 221(256), 1995.

[97] C. H. Desch. The solidification of metals from the liquid state. *J. Inst. Met.*, 22(241), 1919.

[98] P. Feltham. Grain growth in metals. *Acta Metall.*, 5(97), 1957.

[99] T. G. Mason, J. Bibette, and D. A. Weitz. Yielding and flow of monodisperse emulsions. *J. Colloid Interface Sci.*, 179(439), 1996.

[100] W. H. Herschel and R. Bulkley. Konsistenzmessungen von gummi-benzollösungen. *Colloid. Polym. Sci.*, 39(291), 1926.

[101] V. Mansard and A. Colin. Local and non local rheology of concentrated particles. *Soft Matter*, 8(4025), 2012.

[102] P. Jop, Y. Forterre, and O. Pouliquen. A constitutive law for dense granular flows. *Nature*, 441(727), 2006.

[103] P. E. Peyneau and J-N. Roux. Frictionless bead packs have macroscopic friction, but no dilatancy. *Phys. Rev. E*, 78(011307), 2008.

[104] R. Lespiat, S. Cohen-Addad, and R. Höhler. Jamming and flow of random-close-packed spherical bubbles: An analogy with granular materials. *Phys. Rev. Lett.*, 106(148302), 2011.

[105] A. Taboada, N. Estrada, and F. Radjai. Additive decomposition of shear strength in cohesive granular media from grain-scale interactions. *Phys. Rev. Lett.*, 97(098302), 2006.

[106] J. Lauridsen, M. Twardos, and M. Dennin. Shear-induced stress relaxation in a two-dimensional wet foam. *Phys. Rev. Lett.*, 89(098303), 2002.

[107] H. M. Princen. Rheology of foam and highy concentrated emulsions. 1. elastic properties and yield stress of z cylindrical model system. *J. Colloid Interface Sci.*, 91(160), 1983.

[108] L. W. Schwartz and H. M. Princen. A theory of extensional viscosity for flowing foams and concentrated emulsions. *J. Colloid Interface Sci.*, 118 (201), 1987.

[109] N. D. Denkov, V. Subramanian, D. Gurovich, and A. Lips. Wall slip and viscous dissipation in sheared foams: Effect of surface mobility. *Colloids Surf. A*, 263(129), 2005.

[110] B. P. Tighe, E. Woldhuis, J. J. C. Remmers, W. van Saarloos, and M. van Hecke. Model for the scaling of stresses and fluctuations in flows near jamming. *Phys. Rev. Lett.*, 105(088303), 2010.

[111] G. Katgert, B. P. Tighe, M. E. Möbius, and M. van Hecke. Couette flow of two-dimensional foams. *Europhys. Lett.*, 90(54002), 2010.

[112] H. M. Princen and A. D. Kiss. Rheology of foams and highly concentrated emulsion: 4. an experimental study of the shear viscosity and yield stress of concentrated emulsions. *J. Colloid Interface Sci.*, 128(176), 1989.

[113] V. Mansard, A. Colin, P. Chaudhuri, and L. Bocquet. A molecular dynamics study of non-local effects in the flow of soft jammed particles. *Soft Matter*, 9(7489), 2013.

[114] R. J. Clancy, E. Janiaud, D. Weaire, and S. Hutzler. The response of 2d foams to continuous applied shear in a couette rheometer. *Eur. Phys. J. E*, 21(123), 2006.

[115] J. Goyon, A. Colin, G. Ovarlez, A. Ajdari, and L. Bocquet. Spatial cooperativity in soft glassy flows. *Nature*, 454(84), 2008.

[116] L. Bocquet, A. Colin, and A. Ajdari. Kinetic theory of plastic flow in soft glassy materials. *Phys. Rev. Lett.*, 103(036001), 2009.

[117] F. da Cruz, S. Emam, M. Prochnow, J-N. Roux, and F. Chevoir. Rheophysics of dense granular materials: Discrete simulation of plane shear flows. *Phys. Rev. E*, 72(021309), 2005.

[118] T. Hatano. Power-law friction in closely packed granular materials. *Phys. Rev. E*, 75(060301), 2007.

[119] C.-A. Coulomb. *Mém. Acad. Sci. Savants Etrangers*. Inst. Imperial France, 1772.

[120] P. J. Blau. The significance and use of the friction coefficient. *Tribol. Int.*, 34(585), 2001.

[121] C. Cassar, M. Nicolas, and O. Pouliquen. Submarine granular fllows down inclined planes. *Phys. Fluids*, 17(103301), 2005.

[122] I. Cheddadi, P. Saramito, C. Raufaste, P. Marmottant, and F. Graner. Numerical modelling of foam couette flows. *Eur. Phys. J. E*, 27(123), 2008.

[123] G. Debrégeas, H. Tabuteau, and J.-M di Meglio. Deformation and flow of a two-dimensional foam under continuous shear. *Phys. Rev. Lett.*, 87(178305), 2001.

[124] Inc. Wolfram Research. *Mathematica Edition: Version 7.0.* Wolfram Research, Inc., Champaign, Illinois, 2008.

[125] J. Goyon, A. Colin, and L. Bocquet. How does a soft glassy material flow: finite size effects, non local rheology, and flow cooperativity. *Soft Matter*, 6 (2668), 2010.

[126] J. D. Barry, D. Weaire, and S. Hutzler. Nonlocal effects in the contnuum theory of shear localisation in 2d foams. *Phil. Mag. Lett.*, 91(432), 2011.

[127] G. Ovarlez, S. Rodts, A. Ragouilliaux, P. Coussot, J. Goyon, and A. Colin. Wide gap couette flows of dense emulsions: local concentration measurements, and comparison between macroscopic and local constitutive law measurements through mri. *Phy. Rev. E*, 78(036307), 2008.

[128] I. T. Davies, S. J. Cox, and J. Lambert. Reconstruction of tomographic images of dry foams. *Coll. Surf. A*, 2013.

[129] D. Weaire, V. J. Langlois, M. Saadatfar, and S. Hutzler. Foam as granular matter. In T. Di Matteo, T. Aste, and A. Tordesillas, editors, *Granular and Complex Materials*, volume 8 of *World Scientific Lecture Notes in Complex Systems*. World Scientific, New Jersey, 2007.

[130] GDR Midi. On dense granular flows. *Eur. Phys. J. E*, 14(341), 2003.

[131] V. Poulichet. Rheological properties of wet foam. Master's thesis, School of Physics, Trinity College Dublin, School of Physics, Trinity College Dublin, Dublin 2, Ireland, 2012.

[132] V. Poulichet, C. B. O'Donovan, G. Ryan, and M. E. Möbius. Static angle of repose in two dimensional foam. in preparation, 2013.

[133] C. A. Schneider, W. S. Rasband, and K. W. Eliceiri. Nih image to imagej: 25 years of image analysis. *Nature Methods*, 9(671), 2012.

[134] W. B. Landsman. Astronomical data analysis software and systems ii. In R. J. Hanisch, R. J. V. Brissenden, and J. Barnes, editors, *A.S.P. Conference Series*, volume 52, page 246, 1993.

[135] S. Kalpakjian and S. R. Schmid. *Manufacturing Processes for Engineering Materials*. Prentice Hall, 2010.

[136] O. Pouliquen and N. Renaut. Onset of granular flows on an inclined rough surface: Dilatancy effects. *J. Phys. II*, 6(923), 1996.

[137] O. Reynolds. On the dilatancy of media composed of rigid particles in contact, with experimental illustrations. *Phil. Mag.*, 20(469), 1885.

[138] D. Weaire and S. Hutzler. Dilatancy in liquid foams. *Phil. Mag.*, 83(2747), 2003.

[139] F. Rioual, S. Hutzler, and D. Weaire. Elastic dilatancy in wet foams: A simple model. *Coll. Surf. A*, 263(117), 2005.

[140] P. L. Marze, A. Saint-Jalmes, and D. Langevin. Protein and surfactant foams: Linear rheology and dilatancy effect. *Coll. Surf. A*, 263(121), 2005.

[141] R. A. Bagnold. *The Physics of Blown Sand and Desert Dunes*. Methuen, London, 1941.

[142] O. Pouliquen. Scaling laws in granular flows down rough inclined planes. *Phys. Fluids*, 11(542), 1999.

[143] O. Pouliquen and Y. Forterre. Friction law for dnese granular flows: applications to the motion of a mass down a rough inclined plane. *J. Fluid Mech.*, 453(133), 2002.

[144] P. J. Steinhardt, D. R. Nelson, and M. Ronchetti. Bond-orientational order in liquids and glasses. *Phys. Rev. B*, 28(784), 1983.

[145] W. Lechner and C. Dellago. Accurate determination of crystal structures based on averaged local bond order parameters. *J. Chem. Phys.*, 129 (114707), 2008.

[146] A. J. Meagher. *The structure of monodisperse foam.* PhD thesis, School of Physics, Trinity College Dublin, 2012.

[147] S. Timoshenko and J. N. Goodier. *Theory of Elasticity.* McGraw-Hill Book Company, 1951.

[148] D. J. Acheson. *Elementary Fluid Dynamics.* Clarendon Press, Oxford, 1990.